Neural Targets of Cervical Transcutaneous Spinal Cord Stimulation: Experimental and Computational Approaches for Therapeutic Applications

Roberto Martins de Freitas

September 2022

Neural Targets of Cervical Transcutaneous Spinal Cord Stimulation: Experimental and Computational Approaches for Therapeutic Applications

A dissertation submitted to

THE GRADUATE SCHOOL OF ENGINEERING SCIENCE

OSAKA UNIVERSITY

in partial fulfillment of the requirements for the degree of

DOCTOR OF PHILOSOPHY IN ENGINEERING

By

Roberto Martins de Freitas

September 2022

Abstract

Cervical transcutaneous spinal cord stimulation (tSCS) is a non-invasive electrical stimulation technique that can used to activate the nerve fibers at multiple spinal segments of the cervical level. These nerve fibers branch from (via sensory fibers) and to (via motor fibers) the upper-limb muscles. The tSCS stimulation technique has recently attracted considerable interest in motor rehabilitation of upper-limb function in spinal cord injured (SCI) individuals. The efficacy of cervical tSCS in upper-limb motor recovery was suggested to depend on the spatiotemporal activation of sensory fibers rather than motor fibers. To better understand the neural targets of cervical tSCS, I investigated the mechanisms of sensory and motor fiber activation using both experimental and computational simulations. In my first study, I developed a computational model to analyze activations of different groups of motor and sensory fibers during cervical tSCS. First, I developed a 3D geometrical model of the cervical spinal cord and stimulation electrodes, and used it to estimate the electric potential distributions along the trajectory of the sensory (proprioceptive and cutaneous) and motor fibers at the C7 spinal segment. The cathode electrode was placed at the C7 vertebral level, while the anode was on the anterior neck. Dedicated motor and sensory fiber compartment models were used to simulate the activation of motor, proprioceptive sensory and cutaneous sensory fibers. The minimum stimulation intensity necessary to activate the nerve fibers were estimated and compared across the different groups of fibers. My results showed that groups of proprioceptive and cutaneous sensory fibers were co-activated at lower stimulation intensities compared with motor fibers. These findings suggested a sizable contribution of sensory proprioceptive and cutaneous fibers underlying the rehabilitation mechanisms of upper-limb motor recovery after SCI. In my second study, I examined the excitability and selectivity of cervical spinal segments using different cervical tSCS cathode and anode electrode configurations in an experimental

investigation including ten able-bodied individuals. Excitability and selectivity were examined by comparing the evoked responses recorded from electromyography (EMG) signals of six proximal arm and distal hand muscles while the cathode was placed at three positions (C6, C7, and T1) and the anode was fixed on the anterior neck. Additionally, EMG evoked responses were also compared across four anode configurations (neck, shoulders, iliac crests, and back). My results showed that distal hand muscles were preferentially activated when the cathode was placed over the C7 and T1 vertebral levels compared with the C6 cathode position. For all cathode positions, proximal arm muscles were activated at lower stimulation intensities compared with distal hand muscles. Moreover, all muscles were more effectively activated when the anode was placed over the anterior neck compared with the other anode configurations (shoulders, iliac crests, and back). Therefore, these results suggested that placing the cathode at C7 and T1 vertebral levels while the anode is fixed on the anterior neck can increase the activation of sensory fibers, thus improving rehabilitation outcomes. In my third study, I used computational simulations to examine the excitability of caudal spinal segments (C7 and C8 level) using cervical tSCS electrode configurations consistent with my experimental study. First, I updated the 3D geometrical model to include the C8 spinal segment, and used it to estimate the electric potential distribution along the trajectories of sensory proprioceptive and motor fibers at both C7 and C8 spinal segments. The cathode electrode was simulated at three positions: C6, C7, and T1 vertebral levels; and in three sizes: 5.0 x 5.0 (L), 3.5 x 3.5 (M); and 2.5 x 2.5 (S) cm^2, while the anode was fixed on the anterior neck. Dedicated motor and sensory compartment models were used to simulate motor and sensory proprioceptive fibers, respectively. The minimum stimulation intensity necessary to activate the fibers were compared between motor and sensory fibers and across the different cathode configurations. My results showed that sensory fibers at C7 and C8 spinal segments were activated at lower stimulation intensities when the cathode was placed at C7 or T1 vertebral

level compared with the C6 cathode position. Moreover, proprioceptive sensory fibers were activated at lower stimulation intensities when smaller cathode sizes were used. Importantly, for all cathode configurations, motor fibers were consistently recruited at higher stimulation intensities compared with sensory fibers. These results corroborate the experimental results obtained in my experimental study, further suggesting that using small electrodes may optimize the activation of hand muscle sensory fibers during cervical tSCS. From the results I obtained in these three studies, it can be concluded that the activation of proprioceptive and cutaneous sensory fibers may underly the cervical tSCS rehabilitation mechanisms. Moreover, sensory fibers may be more effectively activated by placing the cathode electrode at C7 or T1 vertebral levels, while the anode is fixed on the anterior neck. Overall, these outcomes contribute for better understanding the neural targets activated during non-invasive cervical tSCS, which can be applied to achieve more effective rehabilitation protocols.

Table of contents

Abbreviations

3D	three-dimensional
ANOVA	analysis of variance
APB	abductor pollicis brevis
BB	biceps brachii
ECR	extensor carpi radialis
EMG	electromyography
FCR	flexor carpi radialis
FEM	finite element method
FDI	first dorsal interosseous
HCN	hyperpolarization activated cyclic-nucleotide
NRS	numeric rating scale
SCI	spinal cord injury
SD	standard deviation
TB	triceps brachii
tSCS	transcutaneous spinal cord stimulation

List of Figures

CHAPTER I

General introduction

1.1 Cervical transcutaneous spinal cord stimulation (tSCS)

1.1.1. Basic principles

Transcutaneous spinal cord stimulation (tSCS) is a non-invasive electrical stimulation technique which has recently been attracting interest in motor rehabilitation of upper and lower limbs after spinal cord injury (Gerasimenko et al., 2015b; Benavides et al., 2020; Inanici et al., 2021; Taylor et al., 2021; Barss et al., 2022). Specifically, cervical tSCS is applied with electrodes placed around the cervical level of the spinal cord, such as exemplified in Figure 1.1 (Freyvert et al., 2018; Milosevic et al., 2019b; Inanici et al., 2021; de Freitas et al., 2021; Sasaki et al., 2021). The electrical stimulation is commonly delivered with monophasic or biphasic electric current pulses (Gad et al., 2018; Milosevic et al., 2019b; Islam et al., 2020; Inanici et al., 2021), which can simultaneously activate nerve fibers branching from (i.e. dorsal root sensory fibers) and to (i.e. ventral root motor fibers) multiple upper-limb muscles.

1.1.2. Electrode configurations

A considerable variety of electrode configurations have been used in previous experimental studies to deliver cervical tSCS (Massey et al., 2018; Inanici et al., 2018; Gad et al., 2018; Freyvert et al., 2018; Villar Ortega et al., 2019; Milosevic et al., 2019b; Wu et al., 2020; Benavides et al., 2020; Islam et al., 2020; de Freitas et al., 2021; Sasaki et al., 2021). For instance, cathode electrodes have been commonly configured medially over the C3-T4 vertebra (Inanici et al., 2018; Gad et al., 2018; Milosevic et al., 2019b; Wu et al., 2020; de Freitas et al.,

2021; Sasaki et al., 2021). Moreover, anode electrodes have been configured over the anterior neck (Milosevic et al., 2019b; Wu et al., 2020; de Freitas et al., 2021; Sasaki et al., 2021), clavicles (Murray & Knikou, 2017; Islam et al., 2020), iliac crests (Inanici et al., 2018; Gad et al., 2018; Freyvert et al., 2018; Benavides et al., 2020), or the back (Massey et al., 2018; Villar Ortega et al., 2019). A common electrode configuration used in previous experimental studies is illustrated in Figure 1.1, in which the anode is placed over the anterior neck while the cathode is placed aligned with the vertebral column (Milosevic et al., 2019b; de Freitas et al., 2021; Sasaki et al., 2021).

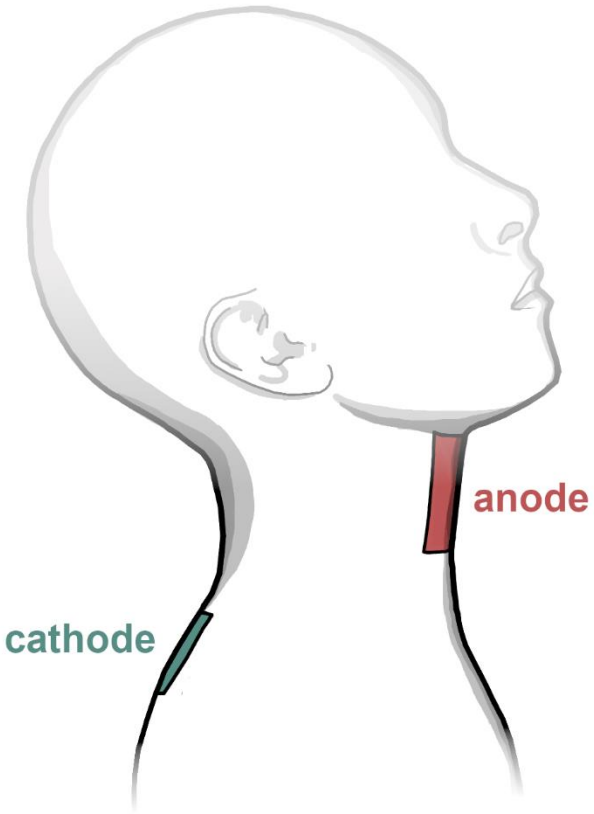

Figure 1.1 – Cervical tSCS electrode configuration: Illustration of a common electrode configuration used to deliver cervical transcutaneous spinal cord stimulation (Milosevic et al., 2019b; Wu et al., 2020; de Freitas et al., 2021; Sasaki et al., 2021). The cathode electrode (negative polarity) is placed over the C7 spinal process and aligned with the midline of the vertebral column, while the anode electrode (positive polarity) is placed over the anterior neck.

1.1.3. Rehabilitation of spinal cord injured individuals

Previous studies have suggested that the recruitment of dorsal root sensory fibers during tSCS enables modulation of specific spinal circuits, which can promote cortical (Manson et al., 2022) and spinal (Rejc et al., 2020; Kumru et al., 2021) changes associated with motor recovery processes after spinal cord injury. Notably, it has also been suggested that the spatiotemporal association between descending commands and the activation of sensory fibers evoked during tSCS is critical for strengthening neural connections across the spinal lesioned regions (Gerasimenko et al., 2015a; Moraud et al., 2016; Wenger et al., 2016; Minassian et al., 2016; Taccola et al., 2018; Capogrosso et al., 2018; Formento et al., 2018; Seáñez & Capogrosso, 2021; Barss et al., 2022). In fact, the activation of sensory fibers should be optimized at different spinal segments to compensate for the scarce sensory feedback below the spinal injury (Gerasimenko et al., 2015a; Wenger et al., 2016; Capogrosso et al., 2018; Formento et al., 2018). These mechanisms enable modifications to corticospinal neural circuits, i.e., neuroplasticity, which result in motor recovery (Gerasimenko et al., 2015a; Moraud et al., 2016; Wenger et al., 2016; Minassian et al., 2016; Taccola et al., 2018; Capogrosso et al., 2018; Formento et al., 2018; Rejc et al., 2020; Greiner et al., 2021; Seáñez & Capogrosso, 2021; Barss et al., 2022; Manson et al., 2022). Therefore, the effectiveness of rehabilitation protocols using cervical tSCS should be increased by maximizing the activation of sensory fibers at specific spinal segments during volitional movements, thus compensating for sensorial feedback below the spinal injury.

CHAPTER I

1.2. Post-activation depression

1.2.1. Basic principles

Post-activation depression is a physiological mechanism used experimentally to analyze the activation of muscle-spindle proprioceptive sensory fibers (Aα-sensory fibers) during electrical stimulation (Hultborn et al., 1996). Notably, this mechanism has been observed using lumbar (Minassian et al., 2007) and cervical (Milosevic et al., 2019b) tSCS. Specifically, post-activation depression can be measured by comparing motor potentials evoked in the electromyography (EMG) signals recorded from the lower or upper-limb muscles while a couple of tSCS pulses are delivered (Minassian et al., 2007; Milosevic et al., 2019b). First, a single stimulation pulse is delivered, thus resulting in a single motor evoked potential. After a few milliseconds (e.g., 50 ms), a second stimulation pulse is delivered, thus resulting in a second motor evoked potential with a smaller amplitude compared with the first response (Figure 1.2). The suppression of the second evoked response amplitude in relation to the first was suggested to correspond to a synaptic depression between the proprioceptive sensory and motor neurons induced after the first stimulus. Notably, a similar mechanism is unlikely to be elicited when other groups of sensory (e.g., cutaneous Aβ-sensory) and motor (e.g., α-motor) fibers are activated (Pierrot-Deseilligny & Burke, 2005). Therefore, post-activation depression specifically indicates the activation of muscle-spindle proprioceptive sensory fibers during tSCS.

1.2.2. Cervical tSCS

Milosevic and colleagues showed post-activation depression mechanisms using cervical tSCS, suggesting preferential activation of proprioceptive fibers (Milosevic et al., 2019b). Specifically, they compared EMG motor evoked potentials recorded from eight upper-limb

muscles, while a couple of monophasic current pulses were delivered (inter-stimulus interval of 50 ms). An anode electrode (7.5 x 10 cm) was placed over the anterior neck, while a cathode electrode (5 x 5 cm) was placed between the C7 and T1 spinal processes (Figure 1.1). Their results showed post-activation depression in all upper-limb muscles, suggesting preferential activation of proprioceptive fibers at multiple cervical spinal segments. Notably, the second evoked responses were not fully suppressed, which also indicated simultaneous activation of other groups of nerve fibers. Taking together, proprioceptive sensory fibers were preferentially activated during cervical tSCS, although the activation of other groups of sensory and motor fibers could not be ruled out.

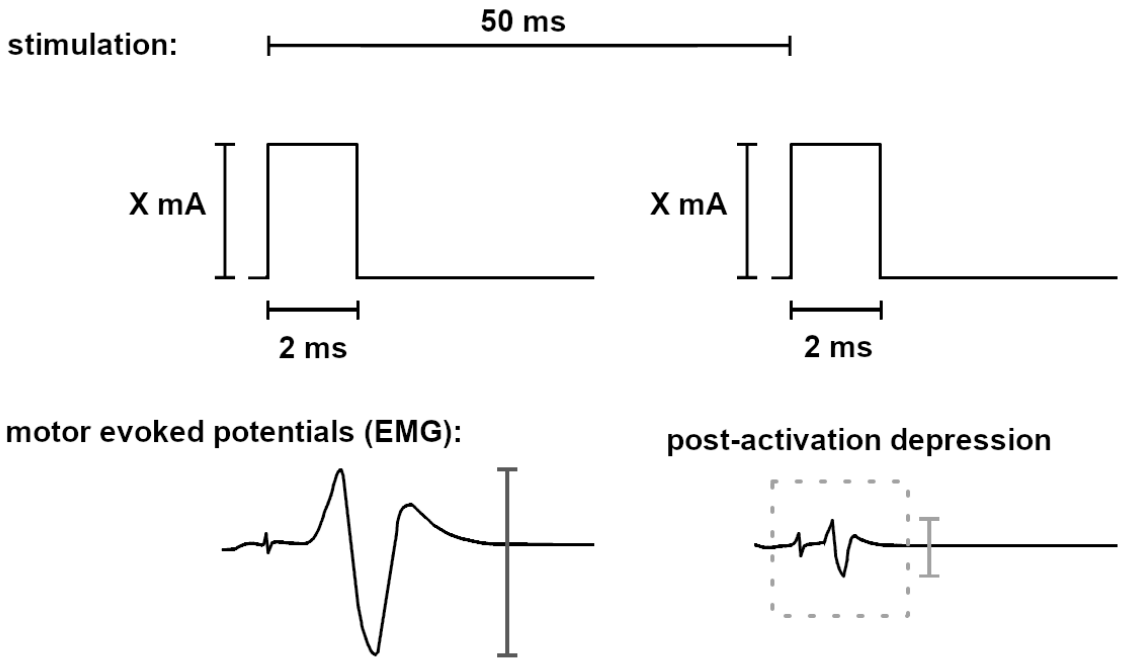

Figure 1.2 – Post-activation depression: Post-activation depression mechanism is illustrated. The first and second tSCS pulses are identical, i.e., same amplitude, X in mA, and duration, 2 ms. The inter-stimuli interval is 50 ms between the first and second pulses. The amplitude of the motor response evoked after the second pulse is smaller compared with the first evoked potential, indicating post-activation depression of the synaptic connection between proprioceptive sensory and motor neurons after the first pulse. In this example, the second motor evoked response recorded in the electromyography (EMG) signal is not completely supressed after the second pulse, suggesting activation of other groups of motor and sensory fibers besides proprioceptive sensory fibers.

CHAPTER I

1.3. Computational models of spinal cord stimulation

1.3.1. Estimation of electric potential distribution using finite element method

Finite Element Method (FEM) is a numerical method used for solving differential equations governing physical systems. This method can be used to estimate the distribution of electric potential across anatomical structures (e.g., gray matter, white matter, dorsal and ventral roots) while spinal cord stimulation is delivered (Ladenbauer et al., 2010; Danner et al., 2011; Khadka et al., 2020; Greiner et al., 2021). Specifically, electromagnetic differential equations are computed for discretized parts (i.e. meshes) of the 3D anatomical geometry, whereas the resulting electric potential is given by interpolating the solutions. For a static physical system, the governing equation is the Laplace equation:

$$\nabla \cdot \big(\sigma(\boldsymbol{x})\nabla V(\boldsymbol{x})\big) = 0 \qquad (1.1)$$

In equation 1.1., $V(\boldsymbol{x})$ is the electric potential at any point $\boldsymbol{x}$ of the geometrical domain. Moreover, the solution of the Laplace equation should also respect the boundary conditions imposed by the geometrical model. Two types of boundary conditions are commonly applied to the geometry interfaces: the Neumann and the Dirichlet. The Dirichlet boundary condition defines values to the solution, such as $V(\boldsymbol{x}) = 0$. The Neumann boundary condition defines values to the derivative of the solution, such as $\nabla V(\boldsymbol{x}) = 0$, where ∇ is the gradient operator.

1.3.2. Nerve fiber models

Since the nerve fiber model developed by Hodgkin and Huxley (Hodgkin & Huxley, 1952) in 1952, succeeding studies have improved the realism in simulations of the membrane dynamics of human nerve cells (Richardson, McIntyre & Grill, 2000; Gaines et al., 2018). Notably, a model developed by McIntyre and colleagues realistically represents the myelin

structure found in mammalian nerve fibers (Richardson, McIntyre & Grill, 2000). This model, referred as MRG model, is composed of multi-compartments of nodes and internodes segments (Richardson, McIntyre & Grill, 2000). Specifically, each node of Ranvier is represented by a single segment (NODE), whereas each internode is represented by three types of segments: paranodal myelin attachment segment (MYSA), paranodal main segment (FLUT), and internodal segment (STIN).

Notably, the MRG model does not implement differences between the excitability of motor and sensory fibers (Dawson, 1956; Kiernan, Mogyoros & Burke, 1996; Forst et al., 2015). In a recent work, Gaines and colleagues (Gaines et al., 2018) have implemented specific channel gating parameters to the MRG which accounts for physiological differences between motor and sensory fibers (Dawson, 1956; Kiernan, Mogyoros & Burke, 1996; Forst et al., 2015). The circuit diagram of the Gaines model is illustrated in Figure 1.3. Importantly, the Gaines models include fast K^+ channels in the node segments, and fast K^+, slow K^+, leak and hyperpolarization activated cyclic-nucleotide gated (HCN) channels in the internodal segments, which are not included in the MRG model (Gaines et al., 2018). The gating parameters of these ion channels are configured differently for sensory and motor nerve fibers, considering the physiological properties of their membrane excitability (Gaines et al., 2018). It is noteworthy that the Gaines models have been used in previous computational studies of spinal cord stimulation (Graham et al., 2019), and have also been validated for peripheral nerve fiber stimulation (Gaines et al., 2018).

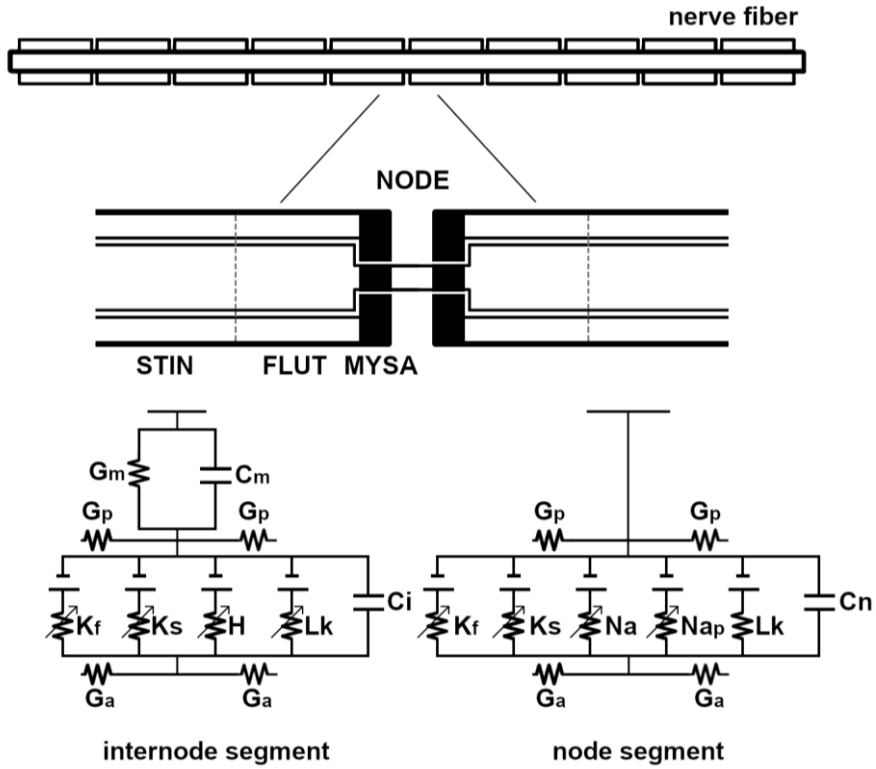

Figure 1.3 – Gaines model: Circuit diagram of the myelinated motor and sensory fiber models developed by Gaines and colleagues (Gaines et al., 2018). The node of Ranvier is represented by one segment (NODE), whereas internodes are represented by three types of segments (MYSA, FLUT and STIN). The model includes: fast K^+ (K_f), slow K^+ (K_s), fast Na^+ (Na), persistent Na^+ (Na_p), leak current (L_k) and HCN (H) channels. Legend – C_n: nodal capacitance, C_i: internodal capacitance, C_m: myelin capacitance, G_a: axoplasmic conductance, G_p: periaxonal conductance, and G_m: myelin conductance. Figure adapted from (McIntyre, Richardson & Grill, 2002).

1.3.3. Computational simulations

An approach for estimating nerve fiber activation during spinal cord stimulation is using the combination of finite element method and compartment nerve fiber model simulations (Rattay et al., 2014). This methodological approach have been used by previous computational studies for lumbar tSCS (Ladenbauer et al., 2010; Danner et al., 2011) and spinal stimulation using electrodes placed epidurally (Graham et al., 2019; Greiner et al., 2021). First, the electric potential distribution along the trajectories of sensory and motor fibers is estimated using finite element method. The distribution of electric potential is then discretized, such as exemplified in Figure 1.4, and applied as extraneural potential to all node and internode segments of a nerve

fiber compartment model (see Appendix A.3 for more details of the equations). Finally, nerve fiber activation is simulated through a system of differential equations which describe the dynamics of membrane potential along time (Appendix A.3).

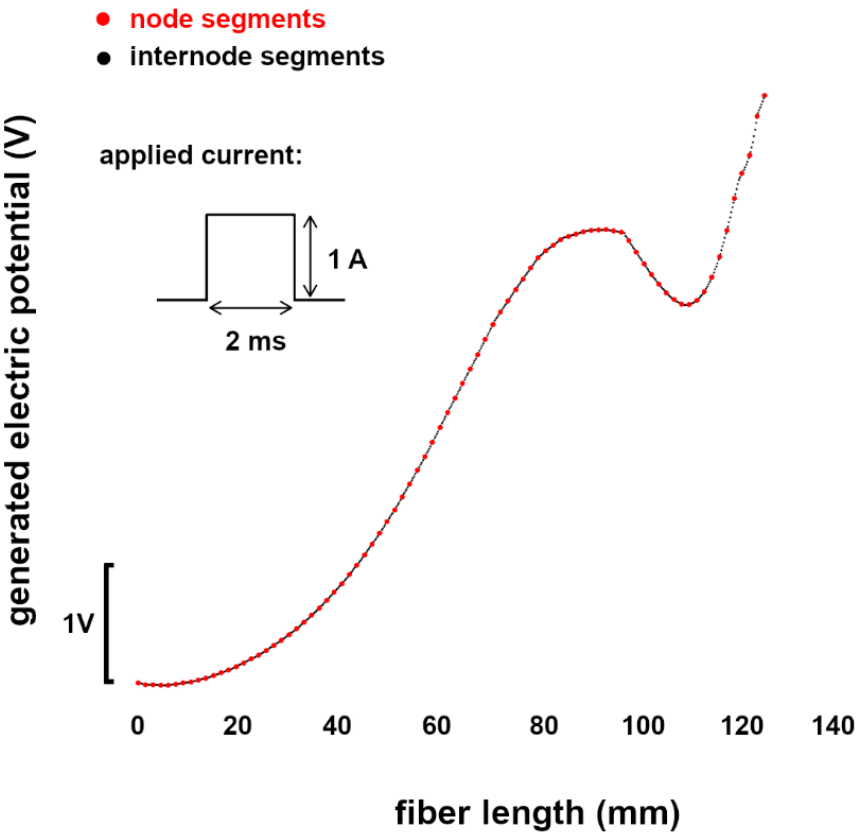

Figure 1.4 – Extraneural potential applied to node and internode segments: Distribution of electric potential at node (red) and internode (black) segments of a sensory fiber measured with Finite Element Method simulations. A stimulation pulse with 1 A amplitude and 2 ms width was simulated. In this example, the Gaines model (Gaines et al., 2018) was used, such that 2 node segments are separated by 10 internode segments.

Importantly, a quasi-static approximation for estimating the electric potential using FEM simulations is often assumed (Ladenbauer et al., 2010; Danner et al., 2011; Khadka et al., 2020; Greiner et al., 2021). This assumption enables solving the governing electromagnetic equations of the system by neglecting capacitive and inductive effects of the tissues, as well as wave propagation effects during stimulation (Plonsey & Heppner, 1967; Bossetti, Birdno & Grill, 2008). It is noteworthy that this assumption is reasonable for common stimulation pulse widths

used experimentally and conductivity values adopted in previous simulation studies (Plonsey & Heppner, 1967; Bossetti, Birdno & Grill, 2008; Ladenbauer et al., 2010; Danner et al., 2011).

1.4. Objectives and hypotheses

1.4.1. Objective and hypothesis 1

To analyze the groups of fibers targeted during cervical tSCS, I analyzed the recruitment of α-motor, proprioceptive Aα-sensory and cutaneous Aβ-sensory fibers using computational simulations (Chapter II). Specifically, a computational approach using FEM and nerve fiber multi-compartment models were developed and applied to enable realistic predictions of nerve fiber activation during cervical tSCS. Considering the experimental results obtained in Milosevic et al. (Milosevic et al., 2019b), I hypothesized that Aα-sensory fibers would be recruited at lower stimulation intensities compared with α-motor fibers. Moreover, since the Aβ-sensory fibers are smaller compared with Aα-sensory fibers, I hypothesized that proprioceptive fibers would be recruited at lower stimulation intensities compared with cutaneous fibers.

.

1.4.2. Objective and hypothesis 2

To examine the selectivity and excitability of different spinal segments using cervical tSCS, I compared EMG evoked potentials recorded from upper-limb muscles using different cathode and anode configurations (Chapter III). Specifically, cervical tSCS evoked potentials were measured and compared across different cathode (C6, C7, and T1 cathode positions) and anode (neck, shoulders, iliac crests and back) electrode configurations used in previous experimental studies, as well as across different hand and arm muscles. Considering the anatomical organization of motor pools in the cervical spinal cord (Kendall et al., 2005), I

hypothesized that more caudal cathode position would be more efficient for activating distal hand muscles, whereas more rostral cathode position would be more efficient for activating proximal arm muscles. Moreover, because of more proximity between the cathode electrode and the anode electrode at the anterior neck, I hypothesized that more muscle activation would be expected using the anterior neck anode position compared with the other anode configurations (shoulders, iliac crests and back).

1.4.3. Objective and hypothesis 3

To confirm my previous experimental findings (de Freitas et al., 2021) and further analyze the excitability of cervical spinal segments during cervical tSCS, I quantified the activation of α-motor and Aα-sensory fibers at C7 and C8 spinal segments using different cathode configurations (Chapter IV). Specifically, the cervical tSCS computational model used in my first study (Chapter II) was incremented to enable simulations of motor and sensory fibers in two spinal segments (C7 and C8 spinal segments) and nine different cathode configurations (three sizes x three cathode positions). The cathode positions were simulated consistently with those used experimentally in Chapter III, i.e. C6, C7, and T1 cathode positions. Considering the proximity between the cathode electrode positions (C6, C7, and T1) and the spinal segments (C7 and C8), I hypothesized that C6 cathode position would be optimal to recruit Aα-sensory fibers at C7 spinal segment, whereas T1 cathode position would be optimal to recruit Aα-sensory fibers at C8 spinal segment. Moreover, considering the post-activation depression mechanisms observed in my previous studies (de Freitas et al., 2021, 2022a), I also hypothesized that Aα-sensory fibers would be activated at lower stimulation intensities compared with α-motor fibers for all the cathode configurations testes. I also hypothesized that the cathode size would affect the activation of Aα-motor and Aα-sensory fibers.

CHAPTER II

Preferential activation of proprioceptive and cutaneous sensory fibers compared to motor fibers during cervical transcutaneous spinal cord stimulation: A computational study

The material presented in this chapter has been published in the article:

de Freitas RM, Capogrosso M, Nomura T, Milosevic M. 2022. Preferential activation of proprioceptive and cutaneous sensory fibers compared to motor fibers during cervical transcutaneous spinal cord stimulation: a computational study. Journal of Neural Engineering 19:1-13. DOI: 10.1088/1741-2552/ac6a7c.

***NOTE**: The content of this chapter is identical to the material presented in the publication.*

CHAPTER II

Abstract

Cervical transcutaneous spinal cord stimulation (tSCS) is a promising technology that can support motor function recovery of upper-limbs after spinal cord injury. Its efficacy may depend on the ability to recruit sensory afferents, conveying excitatory inputs onto motoneurons. Therefore, understanding its physiological mechanisms is critical to accelerate its development towards clinical applications. In this study, we used an anatomically realistic cervical tSCS computational model to compare α-motor, Aα-sensory, and Aβ-sensory fiber activation thresholds and activation sites. We developed a 3D geometry of the cervical body and tSCS electrodes with a cathode centred at the C7 spinous process and an anode placed over the anterior neck. The geometrical model was used to estimate the electric potential distributions along motor and sensory fiber trajectories at the C7 spinal level using a finite element method. We implemented dedicated motor and sensory fiber models to simulate the α-motor and Aα-sensory fibers using 12, 16, and 20 μm diameter fibers, and Aβ-sensory fibers using 6, 9, and 12 μm diameter fibers. We estimated nerve fiber activation thresholds and sites for a 2 ms monophasic stimulating pulse and compared them across the fiber groups. Our results showed lower activation thresholds of Aα- and Aβ-sensory fibers compared with α-motor fibers, suggesting preferential sensory fiber activation. We also found no differences between activation thresholds of Aα-sensory and large Aβ-sensory fibers, implying their co-activation. The activation sites were located at the dorsal and ventral root levels. Using a realistic computational model, we demonstrated preferential activation of dorsal root Aα- and Aβ-sensory fibers compared with ventral root α-motor fibers during cervical tSCS. These findings suggest high proprioceptive and cutaneous contributions to neural activations during cervical tSCS, which inform the underlying mechanisms of upper-limb functional motor recovery.

Keywords: cervical; transcutaneous spinal cord stimulation; upper-limb; computational simulation; finite element method.

CHAPTER II

2.1. Introduction

Cervical transcutaneous spinal cord stimulation (tSCS) has recently emerged as a non-invasive rehabilitation technology for recovery of upper-limb motor function after spinal cord injury (Gad et al., 2018; Benavides et al., 2020; Inanici et al., 2021; Barss et al., 2022). Neuromodulation of cervical spinal neural circuitries may occur when cervical tSCS is combined with supraspinal descending drive, promoting neuroplasticity across the damaged spinal regions (Inanici et al., 2018; Gad et al., 2018; Kumru et al., 2021; Rowald et al., 2022). Specifically, it has previously been suggested that these rehabilitation effects may depend on the activation of sensory fibers during tSCS (Courtine et al., 2016; Formento et al., 2018; Courtine & Sofroniew, 2019; Seáñez & Capogrosso, 2021). On the other hand, direct activation of motor fibers may be adverse to the rehabilitation efficacy as it could lead to multiple-muscle contractions (Wenger et al., 2016; Capogrosso et al., 2018; Greiner et al., 2021). However, little is known about which specific groups of fibers are activated during cervical tSCS. Better understanding of the neural activation targets could therefore provide implications for rehabilitation and inform therapeutic functional parameter selection for cervical tSCS.

The lack of knowledge on what groups of motor and sensory fibers are co-activated during cervical tSCS also limits our interpretation and analysis of the spinally motor evoked potentials in electromyography (EMG) (Milosevic et al., 2019b; Wu et al., 2020; de Freitas et al., 2021; Sasaki et al., 2021). For instance, in previous cervical tSCS experimental studies, the activation of Ia-sensory fibers was inferred by post-activation depression of the motor evoked potentials during application of paired stimuli (Pierrot-Deseilligny & Burke, 2005; Milosevic et al., 2019b; de Freitas et al., 2021; Sasaki et al., 2021). Specifically, post-activation depression was conditioned by two stimulating pulses with equal amplitudes that were sequentially delivered with short (e.g., 50 ms) interstimulus intervals (Milosevic et al., 2019b; Wu et al., 2020; de Freitas et al., 2021; Sasaki et al., 2021). A decrease in the amplitude of the

second motor evoked potential in relation to the first has been suggested to be primarily caused by a suppression of monosynaptic connectivity between Ia-sensory fibers and α-motoneurons after the first stimulus (Milosevic et al., 2019b; Wu et al., 2020; de Freitas et al., 2021; Sasaki et al., 2021). Additionally, when the second motor evoked motor potentials were not fully suppressed, this suggested possible activations of fibers groups other than the Ia-sensory fibers (Milosevic et al., 2019b; de Freitas et al., 2021). These other fiber groups could include large diameter fibers, such as α-motor and Ib-sensory fibers, as previously suggested in experimental studies (Roy, Gibson & Stein, 2012; Gerasimenko et al., 2015a; Milosevic et al., 2019b; de Freitas et al., 2021). Moreover, using experimental recordings and computational simulations, it was also suggested that cutaneous Aβ-sensory fibers could be co-activated in non-human primates during epidural cervical spinal cord stimulation (Greiner et al., 2021). Taking into consideration the practical feasibility of invasively recording neural activities in humans, the activation of sensory and motor fibers during cervical tSCS at a neural level has not been confirmed.

Computational simulations can play an important role in better understanding the physiological mechanisms underlying motor and sensory fiber activations during spinal cord stimulation at a neural level (Ladenbauer et al., 2010; Danner et al., 2011; Capogrosso et al., 2013; Khadka et al., 2020; Greiner et al., 2021). Previous studies have coupled simulations with nerve fiber models to reproduce realistic membrane dynamics in response to extraneural electrical fields, thereby accurately predicting activations of motor and sensory fibers (Ladenbauer et al., 2010; Danner et al., 2011; Khadka et al., 2020; Capogrosso & Lempka, 2020; Greiner et al., 2021). For instance, accurate representations of the proprieties of membrane fibers (e.g., membrane resistance and capacitance) according to the fiber diameters may help reproduce preferential activation of large diameter nerve fibers over the smaller ones during electrical stimulation, i.e., inverse recruitment order (Blair & Erlanger, 1933;

Capogrosso et al., 2013; Greiner et al., 2021). In previous computational studies examining lumbar tSCS, activations of ventral root motor fibers and dorsal root sensory fibers were analyzed during monophasic stimulation pulse (Ladenbauer et al., 2010; Danner et al., 2011). Cervical tSCS computational models, on the other hand, have not yet been developed, primarily owning to the later development of this technology in the rehabilitation of upper-limbs.

The spinal cord anatomy at the cervical body and the lower trunk considerably different (Christ et al., 2010; Calabrese et al., 2018; Mendez et al., 2021), implying that nerve fiber activation mechanisms during lumbar and cervical tSCS are also different. For instance, the ventral and dorsal rootlets are shorter and more obtuse at the cervical body compared with the lower trunk (Calabrese et al., 2018; Mendez et al., 2021). Moreover, the curvature of the spinal cord, as well as the shape of the vertebral bones also differ between the two anatomical regions (Cramer & Darby, 2014). These geometrical differences influence not only in the curvature of the trajectories of motor and sensory nerve fibers, but also the current flow across the spinal canal where the nerve fibers cross (Ladenbauer et al., 2010; Fiocchi et al., 2016). Indeed, the substantial anatomical differences between lumbar and cervical body may critically affect outcomes of cervical tSCS compared to lumbosacral stimulation (Rattay et al., 2014). Therefore, the results obtained with simulations of lumbar tSCS may not be directly translatable to cervical tSCS, and specific computational models are required to better understand the neural activation mechanisms underlying cervical stimulation.

In this study, a cervical tSCS model was developed to simulate activations of α-motor and Aα-sensory fibers using 12, 16, and 20 µm diameters (Danner et al., 2011; Kandel et al., 2013; Gaines et al., 2018), as well as Aβ-sensory fibers using 6, 9, and 12 µm diameters (Kandel et al., 2013; Greiner et al., 2021). Specifically, the cathode electrode was configured at the C7 spinal process while the anode electrode was configured on the anterior neck, following electrode configurations of cervical tSCS experimental studies (Milosevic et al.,

2019b; Wu et al., 2020; de Freitas et al., 2021; Sasaki et al., 2021). The minimum current intensities injected in the anode electrode that are necessary to activate the nerve fibers (activation thresholds) and the location where the action potentials were initiated (activation sites) were compared across different diameter size motor and sensory fibers. We hypothesized that Aα-sensory fibers would be preferentially activated compared with α-motor fibers. In other words, we expect that the Aα-sensory fibers would have lower activation thresholds compared with the α-motor fibers due to their different physiological properties (Dawson, 1956; Kiernan, Mogyoros & Burke, 1996; Forst et al., 2015; Gaines et al., 2018). We also hypothesized that the Aβ-sensory fibers would be least excitable due their smaller range of diameters (Rattay, 1999; Kandel et al., 2013; Rattay et al., 2014). In other words, we expected that Aβ-sensory fibers would have the highest activation thresholds compared with α-motor and Aα-sensory fibers (Rattay, 1999; Kandel et al., 2013; Rattay et al., 2014).

2.2. Methods

We first developed a 3D geometry of the cervical body and stimulation electrodes based on MRI reconstructed volume of the human body and anatomical values from the literature (see section 2.2.1). Using this geometry, we then estimated the electric potential distribution along the trajectories of motor and sensory fibers of the C7 spinal level using the FEM (see section 2.2.2). Dedicated axon fiber models were used to simulate the activation of α-motor, Aα-sensory, and Aβ-sensory fibers when extraneural electric potentials were applied (see section 2.2.3). Finally, we computed the minimum stimulation intensities necessary to activate the nerve fibers, as well as the locations where the action potentials were initiated, to compare the motor and sensory fibers of different diameters (see section 2.2.4).

CHAPTER II

2.2.1. Development of an anatomically realistic cervical tSCS geometrical model

We developed a 3D model representing anatomical structures of the cervical body and stimulation electrodes using Autodesk Inventor Professional 2021 (Autodesk Inc., USA), as illustrated in Figure 2.1. The geometry of the cervical body was designed based on the MRI reconstructed volume of the "virtual family" from a 34 year old male model "Duke" (Christ et al., 2010), and anatomical values from the literature (Lee & Hwang, 2002; West et al., 2012; Torriani et al., 2014; Sass et al., 2017, 2020; Calabrese et al., 2018; Milosevic et al., 2019b; Wade et al., 2020; Mendez et al., 2021; de Freitas et al., 2021). Specifically, the geometry model included 27 components: white matter and gray matter (Calabrese et al., 2018); dorsal and ventral rootlets, and the respective roots, from the right and left sides at C7 spinal level (Sass et al., 2017; Mendez et al., 2021); dorsal root ganglions (West et al., 2012); left and right C7 spinal nerves designed until the clavicle level (Wade et al., 2020); cerebrospinal fluid (Sass et al., 2020); C5, C6, C7, and T1 spinal bones with C5-C6, C6-C7, and C7-T1 inter-vertebral spinal disks (Christ et al., 2010); epidural fat (Christ et al., 2010); general cervical body (Christ et al., 2010); back muscles (Christ et al., 2010); fat (Torriani et al., 2014); skin (Lee & Hwang, 2002); a cathode electrode (5x5 cm) placed over C7 spinal process (Milosevic et al., 2019b; de Freitas et al., 2021; Sasaki et al., 2021); and an anode electrode (7.5x10 cm) placed on the anterior side of the neck (Milosevic et al., 2019b; Wu et al., 2020; de Freitas et al., 2021; Sasaki et al., 2021).

2.2.2. Electric potential distribution estimation

The 3D model was meshed in COMSOL Multiphysics (v.5.6, COMSOL Inc., USA) with approximately 8.5 million tetrahedral elements. We assigned each component of the geometry an electrical conductivity σ as indicated in Table 2.1, consistent with previous studies

(Ladenbauer et al., 2010; Danner et al., 2011; Khadka et al., 2020). Anisotropic electrical conductivities (longitudinal x transversal) of the white matter and back muscles were implemented using the Curvilinear Coordinates toolbox in COMSOL (Greiner et al., 2021). Specifically, the diffusion method was used, while their bottom and top surfaces were defined with the inlet and outlet conditions, respectively (Greiner et al., 2021). All components were considered as purely resistive, and a quasi-static assumption was adopted to calculate the distribution of electric potentials $V(\boldsymbol{x})$ at any point $\boldsymbol{x}$ of the domain during stimulation (Plonsey & Heppner, 1967; Bossetti, Birdno & Grill, 2008; Ladenbauer et al., 2010; Danner et al., 2011). Insulating boundary condition was applied to all external surfaces of the geometry (Khadka et al., 2020). Dirichlet boundary condition was applied to cathode electrode with $V(\boldsymbol{x}) = 0$. Neuman boundary condition was applied to the anode electrode such that a 1 A electric current was injected (Khadka et al., 2020; Greiner et al., 2021). The Laplace equation $\nabla \cdot \big(\sigma(\boldsymbol{x})\nabla V(\boldsymbol{x})\big) = 0$, with the anisotropic electrical conductivity $\sigma(\boldsymbol{x})$ for the white matter and back muscles, was solved with the FEM in COMSOL to obtain the electric potential distributions across the 3D geometry.

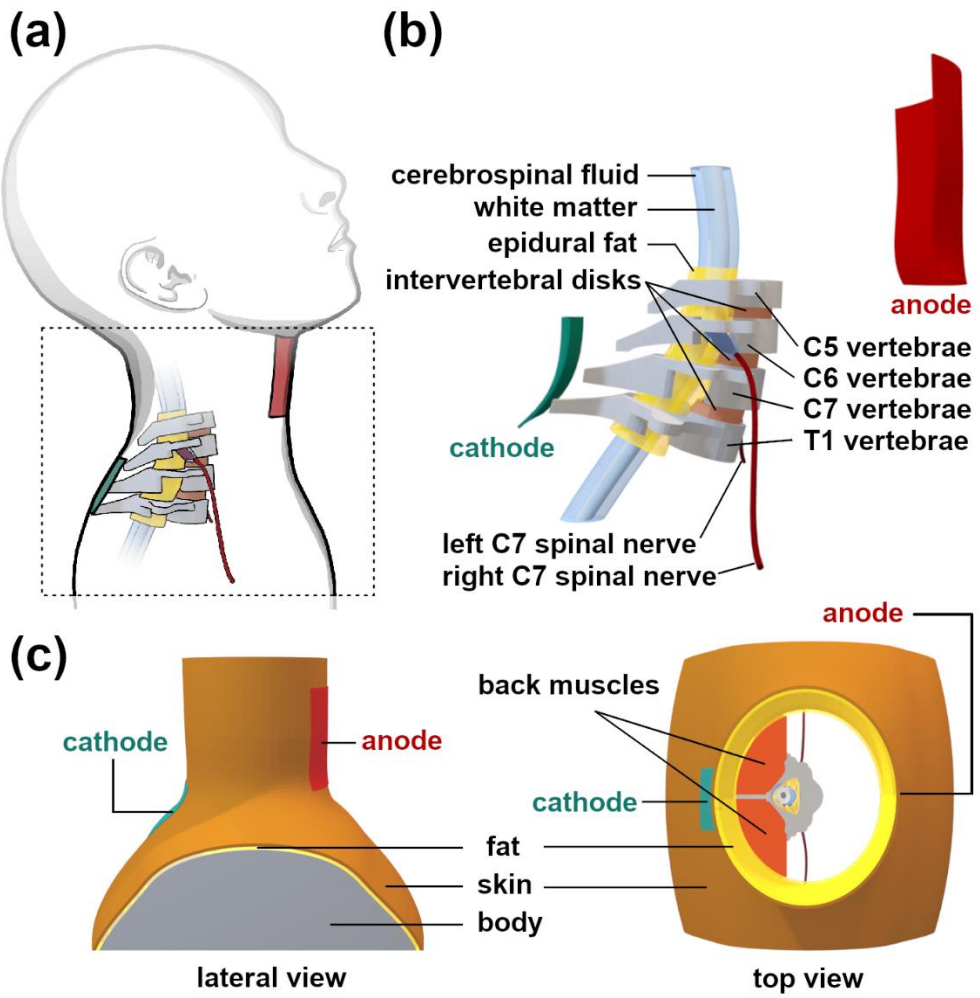

Figure 2.1 – 3D model of the cervical spinal cord including C7 spinal nerve: (a) Illustration of the cervical body configuration during cervical transcutaneous spinal cord stimulation (tSCS) considered for the development of the 3D model. A cathode (green) and an anode (red) electrodes are arranged in a configuration used by previous cervical tSCS experimental studies (Milosevic et al., 2019b; de Freitas et al., 2021; Sasaki et al., 2021). Specifically, the cathode electrode is configured over the C7 spinal process and the anode electrode over the anterior neck. The dashed square illustrates the anatomical boundaries considered in the 3D model. (b and c) 3D model of the cervical body developed based on realistic anatomical proportions. (b) most of the model components surrounding the spinal canal are shown. The gray matter and dorsal and ventral roots are not visible. (c) In the lateral view, the fat, body and skin structures are indicated. In the top view, the back muscles enclosed between the fat and vertebra structures are also shown, while the body structure is not visible.

2.2.3. Axon models

A sensory and a motor axon fiber models developed by Gaines and colleagues (Gaines et al., 2018) were used to simulate the dynamics of the membrane potentials during cervical tSCS (Graham et al., 2019; Khadka et al., 2020). The Gaines models (Gaines et al., 2018) are derived from the model developed by McIntyre, Richardson, and Grill (MRG) (McIntyre,

Richardson & Grill, 2002), and implements adjustments to the specific channel gating parameters to account for motor and sensory fibers physiological differences (Dawson, 1956; Kiernan, Mogyoros & Burke, 1996; Forst et al., 2015). For both motor and sensory fiber models, the nerve fiber consists of nodal and internodal segments, as illustrated in Figure 2.2A. Each node of Ranvier is represented by a single segment (NODE), and each internode by ten segments: two paranodal myelin attachment segments (MYSA); two paranodal main segments (FLUT); and six internodal segments (STIN) (McIntyre, Richardson & Grill, 2002; Gaines et al., 2018). The Gaines models (Gaines et al., 2018) include fast K^+ channels in the node segments, and fast K^+, slow K^+, leak and hyperpolarization activated cyclic-nucleotide gated (HCN) channels in the internodal segments, which accounts for a more realistic representation of ion channels of motor and sensory fibers (Howells et al., 2012). The membrane and myelin sheath conductance and capacitance values are defined according to the diameter and length dimensions of the nodal and internodal segments (NODE, MYSA, FLUT, and STIN). In turn, the NODE diameter, STIN diameter, STIN length, length between two NODE, number of myelin lamellae and STIN length, were linearly extrapolated from (McIntyre, Richardson & Grill, 2002) for each axon fiber diameter size that was simulated (i.e., for 6, 9, 12, 16, and 20 μm), consistent to pervious studies (Danner et al., 2011). The Gaines motor and sensory axon fiber models and the MGR model were implemented in Python 3.9 using NEURON 8.0 (Hines & Carnevale, 1997).

Table 2.1: Conductivity values, in siemens per meter (S/m), of the materials assigned to the components of the geometrical model of the cervical body (gray matter, white matter, ventral/dorsal roots and rootlets, dorsal root ganglia, C7 spinal nerves, cerebrospinal fluid, epidural fat, C5-C6, C6-C7 and C7-T1 intervertebral disks, C5, C6, C7 and T1 vertebra, back muscles, general cervical body, skin and fat) and the electrodes (i.e., anode and cathode electrodes). For white matter and muscles, anisotropic conductivities were assigned to longitudinal (L) and transversal (T) components.

Material	Conductivity σ (S/m)
Gray matter	0.276
White matter	L: 0.6; T: 0.083
Spinal nerve, root, dorsal root ganglion and rootlet	0.1432
Cerebrospinal fluid	1.7
Epidural fat	0.04
Intervertebral disk	0.6
Spinal bone	0.02
Muscle	L: 0.5; T: 0.08
Body	0.25
Skin	0.0025
Fat	0.04
Electrode	0.01

Legend: L – longitudinal; T – transversal

2.2.4. Simulation conditions

Gaines model simulations

The distribution of electric potentials was estimated along the α-motor, Aα-sensory, and Aβ-sensory fiber trajectories, which are shown in Figure 2.2. Specifically, different fiber trajectories were defined along the left and right C7 spinal nerves from the clavicles level until inside the spinal cord. At each dorsal (sensory fibers) and ventral (motor fibers) root, three different trajectories were defined spanning across the middle portion of the rootlet structures. At the interface between the ventral rootlets and the white matter, each motor fiber was further defined in three other pathways leading towards the center of the gray matter. Moreover, at the interface between the dorsal rootlets and the white matter, each Aα-sensory fiber trajectory was defined in three other pathways towards the center of the gray matter, while each Aβ-sensory fiber trajectory was defined in three ascending pathways towards rostral levels of the dorsal

column (Burke & Glenn, 1996), consistent with a previous study (Greiner et al., 2021). In total, 18 trajectories were defined for each of the α-motor, Aα-sensory, and Aβ-sensory fibers, including the right and left sides (i.e., 3 segments at the roots level x 3 segments entering the white matter x 2 sides = 18 trajectories).

To estimate the activation thresholds, which are the minimum stimulation intensity required to activate the fibers, we scaled the distributions of electric potentials along the motor and sensory fiber trajectories and applied them as extraneural potentials to the axon fiber models (Grill, 1999; Richardson, McIntyre & Grill, 2000). Specifically, for each fiber, the extraneural potential distribution was computed as the minimum level required for fiber activation using a bisection algorithm (Danner et al., 2011; Khadka et al., 2020). The extraneural potential distributions were applied by simulating a rectangular monophasic stimulation pulse with 2 ms duration, consistent with previous cervical tSCS experimental studies (Milosevic et al., 2019b; de Freitas et al., 2021; Sasaki et al., 2021). It is noteworthy that the stimulation current applied at the anode electrode and the electric potential in the domain, $V(\boldsymbol{x})$, are linearly related. Therefore, the scaling factor estimated to elicit fiber activation corresponds to a fraction of the 1 A initially simulated at the anode electrode with FEM simulations. Furthermore, we also estimated the locations along the trajectories where the action potentials were initiated at the activation threshold intensity, i.e., activation sites.

The α-motor, Aα-sensory, and Aβ-sensory fibers were simulated using the motor and sensory fiber models proposed by Gaines et al. (Gaines et al., 2018). The α-motor and Aα-sensory fibers with trajectories entering the gray matter were simulated using 12, 16, and 20 μm diameters (Kandel et al., 2013), which were used in previous simulation studies (Danner et al., 2011; Gaines et al., 2018). Specifically, this range of fiber diameters covers the sizes of Ia- and Ib-sensory fibers, as well as large diameter α-motor fibers (Kandel et al., 2013). The Aβ-sensory fibers ascending the dorsal column were simulated using 6, 9, and 12 μm diameters,

consistent with previous simulation studies (Greiner et al., 2021). These diameter sizes are within the range corresponding to the group of Aβ-sensory fibers and also ascending branches of Ia-sensory fibers, which were considered to be two-thirds of the diameters of the dorsal root segments (Burke & Glenn, 1996). The 18 trajectories that were simulated for each fiber type caused the electric potential distribution along each fiber to be slightly different, thereby introducing microanatomical variations for the estimation of activation thresholds, allowing for statistical analysis (Gaines et al., 2018; Greiner et al., 2021).

MRG model stimulation

To examine the methodological considerations used by Danner and colleagues (Danner et al., 2011), we also used the MRG model (McIntyre, Richardson & Grill, 2002) to estimate the activation thresholds of the motor and sensory fibers, which were differentiated only by their diameter sizes. In agreement with their methodology, only motor and sensory fibers entering the gray matter were simulated (i.e. the same 18 trajectories defined for α-motor and Aα-sensory fibers), while the trajectories ascending towards the dorsal column from the dorsal roots were omitted (Danner et al., 2011). Specifically, the sensory fibers were simulated with the 16 µm diameters and motor fibers with the 14 µm diameters (Danner et al., 2011). Additionally, the Gaines models were also used to simulate motor fibers with 14 µm diameters and sensory fibers with 16 µm diameters to enable a direct comparison between the activation thresholds obtained with both models.

2.2.5. Statistics

Since normality of the data could not confirmed for all analysis groups using the Shapiro-Wilk test, nonparametric tests were used. First, the Kruskal-Wallis test was used to

compare activation thresholds of α-motor, Aα-sensory and Aβ-sensory fibers that were pooled across their respective fiber diameters (*fiber type*: α-motor, Aα-sensory, and Aβ-sensory). Moreover, the Kruskal-Wallis test was also used to compare the activation thresholds across groups of motor and sensory fibers with different diameters to examine possible co-activations (*fiber groups*: $\alpha\text{-motor}_{12}$, $\alpha\text{-motor}_{16}$, $\alpha\text{-motor}_{20}$, $A\alpha\text{-sensory}_{12}$, $A\alpha\text{-sensory}_{16}$, $A\alpha\text{-sensory}_{20}$, $A\beta\text{-sensory}_{6}$, $A\beta\text{-sensory}_{9}$, and $A\beta\text{-sensory}_{12}$). When significant results were found for the Kruskal-Wallis test, multiple-pairwise comparisons were performed with Bonferroni corrections. The Mann-Whitney test was used to compare the activation thresholds of motor and sensory fibers estimated using the MRG model (*MRG fibers*: $MRG_{sensory16}$ and $MRG_{motor14}$ and). Additionally, the Mann-Whitney test was also used to compare the activation thresholds of motor and sensory fibers estimated using the Gaines models (*Gaines fibers*: $Gaines_{motor14}$ and $Gaines_{sensory16}$). Statistical tests were performed using SPSS (IBM, Armonk, NY) and the significance level was set to $\alpha=0.05$.

2.3. Results

2.3.1. Gaines model motor and sensory fibers activation thresholds and sites

We used the motor and sensory fiber models developed by Gaines and colleagues (Gaines et al., 2018) to simulate the α-motor, Aα-sensory, and Aβ-sensory fibers. The α-motor and Aα-sensory were simulated using 12, 16, and 20 μm diameters, whereas Aβ-sensory fibers were simulated using 6, 9, and 12 μm diameters. For each fiber group, the activation thresholds and sites were estimated using 18 trajectories (see sections 2.2.4 and 2.3.2), shown in Figure 2.3. We identified the activation sites at the activation threshold intensity level for each simulated fiber (Figure 2.3). The Kruskal-Wallis test was used to compare between α-motor, Aα-sensory, and Aβ-sensory fibers (*fiber type*: α-motor, Aα-sensory, and Aβ-sensory).

Moreover, the Kruskal-Wallis test was used to compare the activation thresholds of motor and sensory fibers with different diameter sizes (*fiber groups*: α-motor$_{12}$, α-motor$_{16}$, α-motor$_{20}$, Aα-sensory$_{12}$, Aα-sensory$_{16}$, Aα-sensory$_{20}$, Aβ-sensory$_{6}$, Aβ-sensory$_{9}$, and Aβ-sensory$_{12}$).

Activation sites

A representative simulated response of the membrane potentials in all node segments during cervical tSCS is presented in Figure 2.2B. In this illustrative example, we show the activation of a Aα-sensory fiber. Specifically, the 16 µm diameter Aα-sensory fiber that was simulated using the Gaines model for a 2 ms stimulation pulse with amplitude activation threshold intensity (see section 2.4.1.). An action potential was initiated approximately at the middle portion of the dorsal root, corresponding to a valley point in the extraneural electric potential distribution applied along the fiber length, as illustrated on the right side of Figure 2.2C. Analogous to Aα-sensory fibers, the activation sites of α-motor fibers were located in the middle portion of the ventral root, as exemplified on the left side of Figure 2.2C. Contrary to the α-motor and Aα-sensory fibers, the activation sites of Aβ-sensory fibers were located closer to the interface between the dorsal roots and white matter, as illustrated on the left side of Figure 2.2C. Consistent with these representative outcomes, the activation sites of all simulated motor (α-motor) and sensory (Aα- and Aβ-sensory) fibers in our study are shown in Figure 2.3. Indeed, the activation sites for α-motor and Aα-sensory always corresponded to locations at the level of the roots for both the left and right sides. In contrast, the activation sites for Aβ-sensory fibers were consistently located around the interface between rootlets and white matter, where these fibers curved towards the dorsal column.

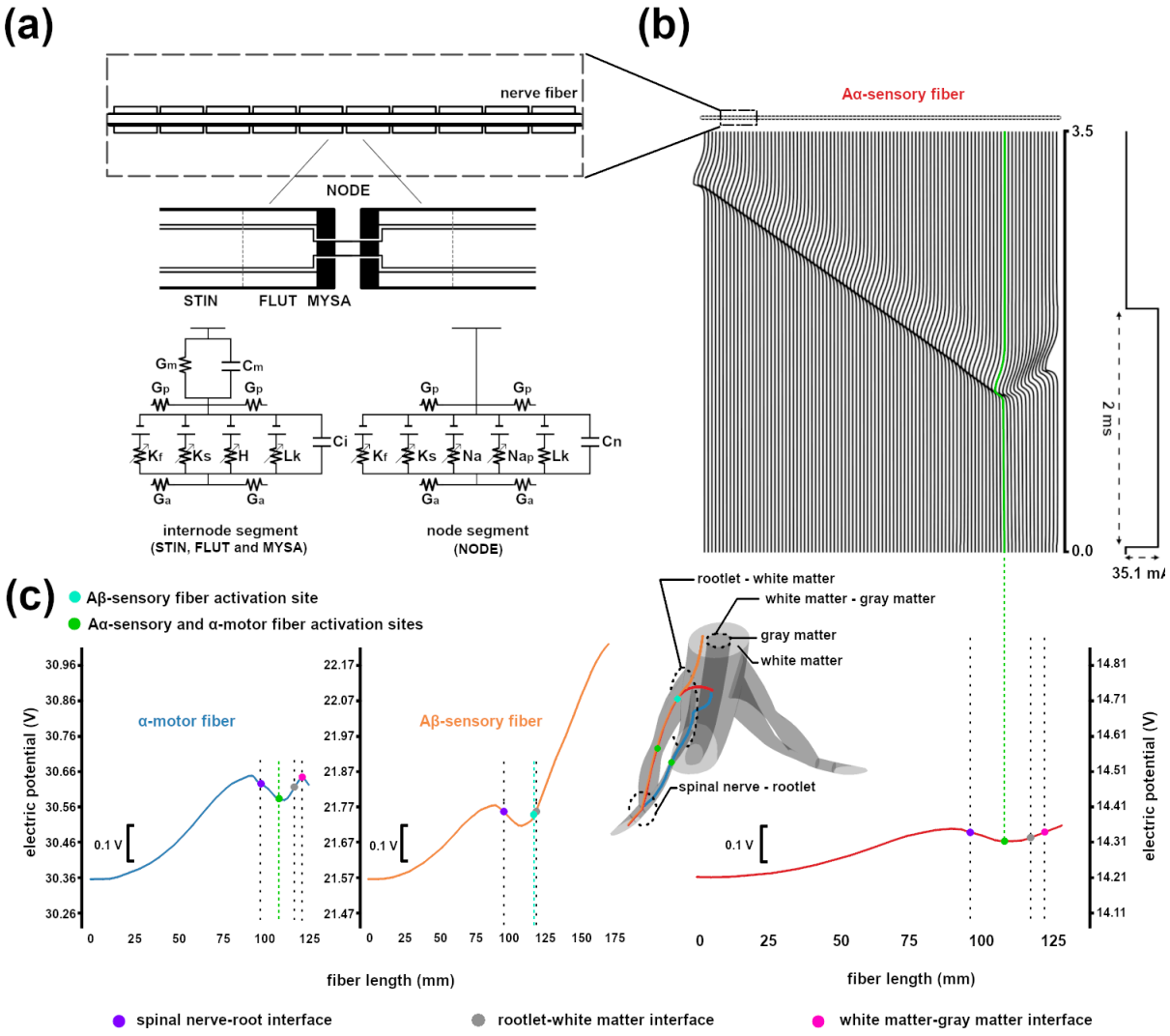

Figure 2.2 – Activation threshold and activation site estimation: (a) Compartment model of myelinated nerve fiber membrane proposed by Gaines et al. (Gaines et al., 2018) to simulate motor and sensory fibers. Each node (NODE) is represented by one segment, and each internode by ten segments: two MYSA, two FLUT and six STIN. The node and internode segments are composed of fast K^+ (K_f), slow K^+ (K_s), fast Na^+ (Na), persistent Na^+ (Na_p), leak current (L_k) and HCN (H) channels. Nodal (C_n), internodal (C_i) and myelin (C_m) capacitances, as well as axoplasmic (G_a), periaxonal (G_p) and myelin (G_m) conductances are also represented in this model. Adapted with permission from (McIntyre, Richardson & Grill, 2002) © 2002 The American Physiological Society. (b) At the top, a representative response of the membrane potentials in all node segments simulated with Gaines model. The representative response is from a 16 µm diameter Aα-sensory fiber with the trajectory entering the gray matter. The minimum stimulation intensity necessary to activate the fiber was 35.1 mA for a 2 ms pulse width. The location where the action potential was initiated, referred to as activation site, was located at the middle portion of the dorsal root, indicated by the green trace. (c) On the right side, the electric potential distribution along the Aα-sensory fiber is shown with its activation site indicated by a green circle. On the left side, representative electric potential distributions along a 16 µm diameter α-motor fiber (blue) and a 9 µm diameter Aβ-sensory fiber (orange) are shown with its corresponding activation sites indicated by green and cyan circles, respectively. The 0 mm fiber length value is located at the clavicles for all fibers. The maximum fiber length values are located at the middle of the gray matter structure for α-motor and α-sensory fibers, and at C5 level of the dorsal column for Aβ-sensory fibers. The stimulation amplitude defined as minimum stimulation intensity necessary to activate the α-motor and Aβ-sensory fibers were 75.0 mA and 53.3 mA, respectively, for a 2 ms pulse width. The location at interface between the spinal nerve and the rootlets, at the interface between the rootlets and the white matter, and at the interface between the white and gray matters are indicated by purple, gray and pink circles, respectively.

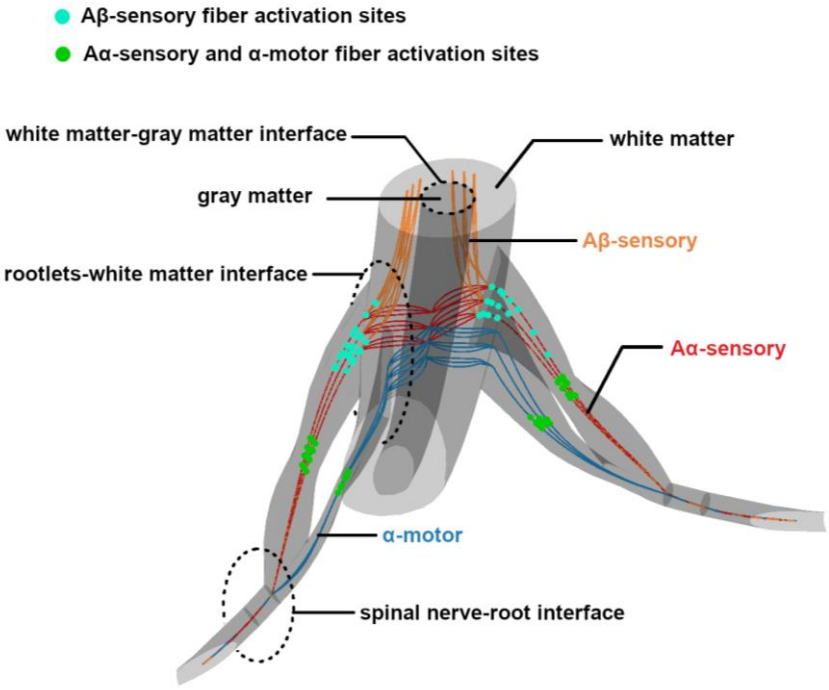

Figure 2.3 – Activation sites of motor and sensory fibers: Activation sites of all the Aα-sensory (red traces) and α-motor fibers (blue traces) are indicated by green circles at the middle portion of the ventral and dorsal roots. The trajectories of these fibers are defined to cross through the white matter and enter the gray matter. The activation sites of the Aβ-sensory fibers (orange traces) are indicated by cyan circles around the interface between the dorsal rootlets and the white matter. The trajectories of the Aβ-sensory fibers are defined to ascend the dorsal column when they enter the white matter. In total, 18 α-motor, 18 Aα-sensory, and 18 Aβ-sensory fibers were simulated with the myelinated nerve fiber model developed by Gaines et al. (Gaines et al., 2018).

Activation thresholds

Comparison results of the activation thresholds across different fiber diameters sizes (*fiber type*: α-motor, Aα-sensory, and Aβ-sensory) are summarized in Figure 2.4A. Our results showed significant main effects between the *fiber type* factors ($\chi^2(2,162)=70.90$, $p<.001$; α-motor: 86.11±22.41 mA, Aα-sensory: 39.72±12.58 mA, and Aβ-sensory: 72.91±45.23 mA; mean ± standard deviation). Multiple pairwise comparisons with Bonferroni corrections showed that the activation thresholds of Aα-sensory fibers were significantly lower compared to α-motor ($p<.001$) and Aβ-sensory fibers ($p<.001$), as well as that activation thresholds of Aβ-sensory fibers were significantly lower compared to α-motor fibers ($p=.001$) (Figure 2.4A).

CHAPTER II

Comparison of co-activation of fibers with different diameter sizes across groups of motor and sensory fibers (*fiber groups:* α-motor$_{12}$, α-motor$_{16}$, α-motor$_{20}$, Aα-sensory$_{12}$, Aα-sensory$_{16}$, Aα-sensory$_{20}$, Aβ-sensory$_{6}$, Aβ-sensory$_{9}$, and Aβ-sensory$_{12}$) are summarized in Figure 2.4B. Our results showed significant main effects between *fiber groups* factor ($\chi^2(8,162)=150.76$, $p<.001$; α-motor$_{12}$: 113.47±9.78 mA, α-motor$_{16}$: 80.52±8.83 mA, α-motor$_{20}$: 64.34±8.01 mA, Aα-sensory$_{12}$: 55.25±6.16 mA, Aα-sensory$_{16}$: 36.34±4.53 mA, Aα-sensory$_{20}$: 27.58±3.36 mA, Aβ-sensory$_{6}$: 128.47±33.93 mA, Aβ-sensory$_{9}$: 55.72±8.57 mA, and Aβ-sensory$_{12}$: 34.54±3.67 mA; mean ± standard deviation). Multiple pairwise comparisons with Bonferroni corrections showed that the activation thresholds between a majority of the fibers were significantly different ($p<.05$). Notably, the Aβ-sensory$_{12}$, Aα-sensory$_{16}$, and Aα-sensory$_{20}$ fibers, as well as α-motor$_{20,}$ α-motor$_{16}$, Aβ-sensory$_{9}$, and Aα-sensory$_{12}$ fibers were not significantly different ($p>.05$) (Figure 2.4B).

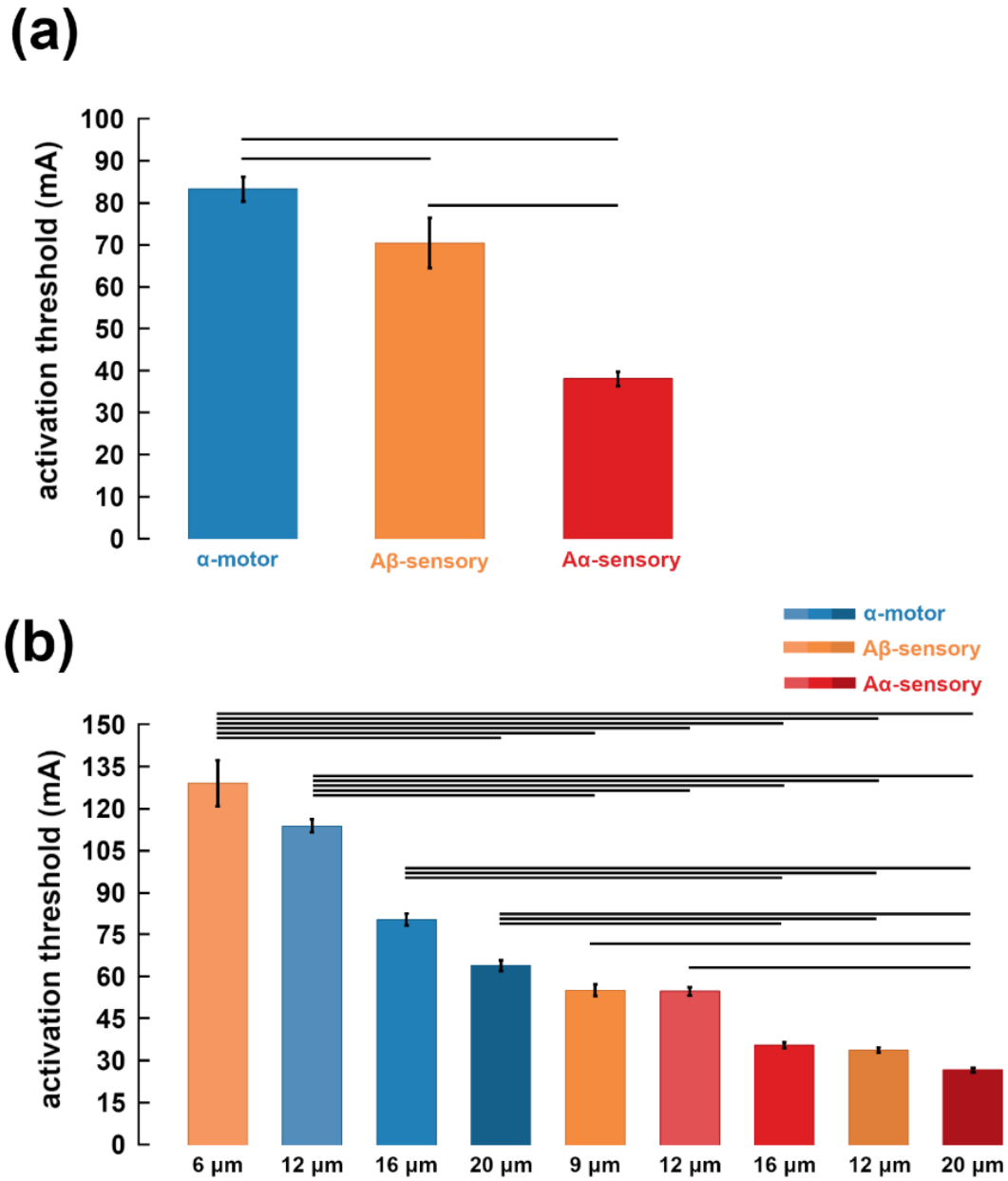

Figure 2.4 – Comparison between α-motor, Aα-sensory and Aβ-sensory fibers simulated with the Gaines models: (a) The minimum cervical transcutaneous spinal cord stimulation intensity, referred to activation threshold (mA), necessary to activate the α-motor (blue), Aα-sensory (red), and Aβ-sensory (orange) fibers was compared using the Kruskal-Wallis test. The α-motor and Aα-sensory fibers were both simulated with 12, 16 and 20 µm diameters, whereas the Aβ-sensory fibers were simulated with 6, 9 and 12 µm diameters. (b) The activation thresholds of the fibers were grouped by diameter sizes and compared using the Kruskal-Wallis test. In total, 9 groups of fibers (α-motor, Aα- and Aβ-sensory fibers simulated with 3 diameters sizes) were compared, each with 18 different trajectories. All the fibers were simulated with the myelinated nerve fiber membrane proposed by Gaines et al. (Gaines et al., 2018). Statistically significant differences found between the groups are indicated by the horizontal bars. The bar plot bins indicate the means of the activation thresholds of each analysis group, and the black vertical bars their standard errors.

2.3.2. MRG model simulations of motor and sensory fibers

We used the MRG nerve fiber model (McIntyre, Richardson & Grill, 2002) and the considerations used by Danner and colleagues (Danner et al., 2011) to simulate the motor and sensory fibers with 14 and 16 µm diameters (Danner et al., 2011), respectively. The activation thresholds were estimated using the same 18 trajectories as the α-motor and Aα-sensory fibers (see sections 2.2.4 and 2.3.2), which are shown as blue and red in Figure 2.3. The Mann-Whitney test was used to compare the motor and sensory activation thresholds simulated with the MGR model (*MRG fibers*: $MRG_{sensory16}$ and $MRG_{motor14}$). Under the same simulation conditions, we also simulated the motor (14 µm diameters) and sensory (16 µm diameters) fibers using the Gaines nerve fiber models (Gaines et al., 2018), and compared their activation thresholds using the Mann-Whitney test (*Gaines fibers*: $Gaines_{motor14}$ and $Gaines_{sensory16}$).

Comparison between $MRG_{sensory16}$ (16 µm diameter) and $MRG_{motor14}$ fibers (14 µm diameter) are summarized in Figure 2.5. Our result showed that activation thresholds of $MRG_{sensory16}$ and $MRG_{motor14}$ fibers were not significantly different (U=105.50, p=.074; $MRG_{motor14}$: 34.15±4.25 mA and $MRG_{sensory16}$: 31.41±4.00 mA; mean ± standard deviation). Moreover, our results also showed that activation thresholds of $Gaines_{sensory16}$ were significantly smaller compared with $Gaines_{motor14}$ fibers (U=171.00, p<.001; $Gaines_{motor14}$: 94.67±9.37 mA and $Gaines_{sensory16}$: 36.34±4.53 mA; mean ± standard deviation).

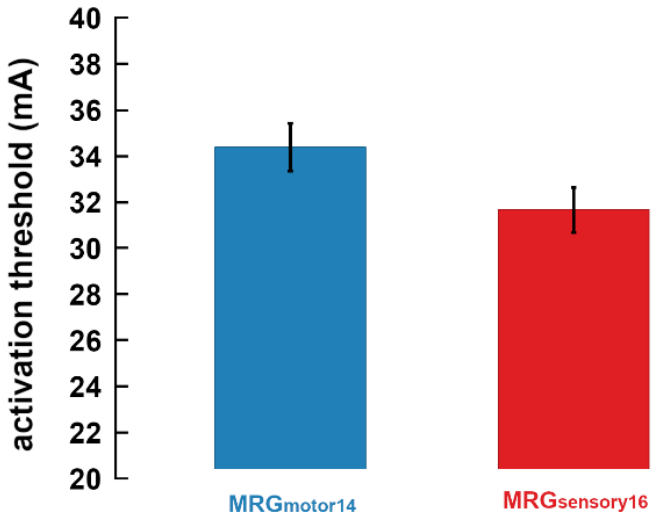

Figure 2.5 – Comparison between motor and sensory fibers simulated with the MRG model: The minimum cervical transcutaneous spinal cord stimulation intensity, referred as activation threshold (mA), necessary to activate the motor (blue) and sensory fibers (red) were compared using the Mann-Whitney test. The motor fibers were simulated with 14 µm and the sensory fibers with 16 µm using the myelinated nerve fiber membrane proposed by McIntyre et al., (McIntyre, Richardson & Grill, 2002). No statistically significant differences were found. The bar plot bins indicate the means of the activation thresholds of each analysis group, and the black vertical bars their standard errors.

2.4. Discussions

We developed a computational model to better understand the neural activation of motor and sensory fibers during cervical tSCS. We found that Aα-sensory and large Aβ-sensory fibers (9 and 12 µm diameters) had lower activation thresholds compared with α-motor fibers (Figure 2.4B). Moreover, the activation sites of α-motor and Aα-sensory fibers were located approximately at the middle portion of the ventral and dorsal roots, respectively, whereas the activation sites of Aβ-sensory were located around the interface between the dorsal rootlets and the white matter. Despite anatomical differences between the cervical and lumbar body, our findings also showed preferential sensory fiber activations at the cervical level as previously demonstrated for lumbar tSCS (Danner et al., 2011). Notably, our findings also suggest a large contribution of cutaneous (i.e., Aβ-sensory) fiber activations during cervical tSCS, despite their relatively small sizes. Taken together, our study elucidates the neural activation mechanisms and provide implications for the therapeutic application of cervical tSCS.

2.4.1. Motor and sensory fiber activations

Previous experimental studies in humans have used post-activation depression of distally recorded EMG responses to investigate weather the recruitment of Ia-sensory fibers affected the cervical tSCS evoked motor potentials (Pierrot-Deseilligny & Burke, 2005; Milosevic et al., 2019b; Wu et al., 2020; de Freitas et al., 2021; Sasaki et al., 2021). In agreement with our hypothesis that Aα-sensory fiber group (representing Ia- and Ib- sensory fibers) would have lower activation thresholds compared with α-motor fibers, our findings confirmed preferential activation of Aα-sensory compared with α-motor fibers (Figure 2.4A). These results are consistent with the mechanism inferred from post-activation depression, which suggested strong contribution of Ia-sensory fiber activation to spinally motor evoked potentials (Milosevic et al., 2019b; de Freitas et al., 2021). Despite not including specific considerations for distinguishing Ia- and Ib- fibers in our simulations, they are likely to be co-activated due to their overlapping range of diameters (Kandel et al., 2013). While the activation of Ib-sensory fibers may activate polysynaptic pathways that inhibit the of spinally motor evoked potentials, they are unlikely to have large a effect on post-activation depression (Pierrot-Deseilligny & Burke, 2005). Furthermore, we showed that large Aβ-sensory fibers ascending from the dorsal roots toward the dorsal column (9 and 12μm diameters) were activated with lower stimulation intensities compared with the α-motor fibers (Figure 2.4B). Comparison across all diameters seems to indicate that Aβ fibers are activated with higher stimulation intensities compared with Aα fibers (Figure 2.4A). However, a closer inspection of activations thresholds between different diameter sizes revealed that Aα- and Aβ-sensory fibers were co-activated across most fiber sizes (Figure 2.4B). Contrary to what was suggested in previous experimental studies, our simulations therefore showed an sizable contribution of cutaneous fibers to the motor evoked potentials during cervical tSCS (McNulty, Türker & Macefield, 1999; Pierrot-Deseilligny & Burke, 2005). While cutaneous afferents may

contribute to motor evoked potentials, they may also convey excitatory potentials to relevant spinal nodes and significantly contribute to the rehabilitative potential of non-invasive spinal stimulation (Peurala et al., 2002; Guidetti et al., 2021; Crema et al., 2022). Taken together, our results showed preferential recruitment of Aα- and Aβ-sensory fibers compared with α-motor fibers, suggesting large proprioceptive and cutaneous contribution to cervical tSCS evoked potentials.

It is well known that nerve fibers with larger diameters are preferentially activated compared with those with smaller diameters when extraneural electric potentials are applied, following an inverse recruitment order (Blair & Erlanger, 1933; Minassian et al., 2016). However, contrary to our hypothesis that Aβ-sensory fibers would have the highest activation thresholds due to their relatively small size, we showed that large Aβ fibers (9 and 12 μm diameters) were recruited at similar stimulation intensities as the Aα fibers (12 and 16 μm diameters) (Figure 2.4B). These results are consistent with the findings of Greiner and colleagues (Greiner et al., 2021) who showed co-activation of Aα and Aβ fibers using computer simulations in non-human primate models (Greiner et al., 2021). Despite the small range of diameter sizes and that cervical tSCS electrodes are located farther away from the targeted sensory dorsal roots, our results nonetheless also demonstrate a sizable contribution of cutaneous Aβ-sensory fibers during non-invasive cervical spinal stimulation. The co-activation Aα and Aβ fibers could be explained by the electric potential distributions along their trajectories, as illustrated in Figure 2.2C. Specifically, the trajectories of Aα-sensory fiber were defined along pathways towards the center of the gray matter structure, whereas Aβ-sensory fibers were defined along pathways ascending in the direction of rostral levels of the dorsal column (Burke & Glenn, 1996; Greiner et al., 2021). After the interface between the dorsal roots and the white matter (at approximately 115 mm in the example showed in Figure 2.2C), the electric potential distribution of Aβ-sensory fibers is increased as the fibers project further

away from the cathode and approach the anode electrode. The Aα-sensory fiber electric potential distributions do not have such large changes after entering the white matter. For instance, Aα-sensory fibers simulated using 12 μm diameter seemed to have higher activation thresholds compared with the Aβ-sensory fibers which were simulated using the same diameter size (Figure 2.4B). These fibers were simulated with same membrane dynamics, whereas they were only different in their trajectories after entering the spinal cord, highlighting the large influence of trajectories on defining the electric potential distributions and consequent activation thresholds. Although Aβ-sensory fibers were simulated using smaller dimeters compared with Aα-sensory fibers, they could be co-activated likely due to their different trajectories. (Figure 2.4B). Contrary to the expected inverse recruitment order, our simulations showed co-activation of cutaneous and proprioceptive nerve fibers despite their different diameters, which may also possibly suggest that non-invasive cervical tSCS can activate some common fiber types as cervical epidural spinal stimulation (Greiner et al., 2021).

2.4.2. Activation sites during cervical tSCS

Differences between the cervical and lower trunk body anatomy, such as the geometrical shape of the vertebra as well as the curvature of dorsal and ventral rootlets at the level where they enter the spinal canal, imply that results obtained from lumbar tSCS simulation studies (Ladenbauer et al., 2010; Danner et al., 2011) may not directly translate to cervical tSCS. These studies showed that activation sites of motor and sensory fibers were located approximately at the point where they enter the white matter or exit the spinal canal (Ladenbauer et al., 2010). In agreement with lumbar tSCS results, our simulations showed activation sites of Aβ-sensory fibers located around the interface between the dorsal rootlets and the white matter (Ladenbauer et al., 2010; Danner et al., 2011). However, activation sites

of α-motor and Aα-sensory fibers were located approximately at the middle portion of the rootlets structure (Figure 2.3). It is noteworthy that α-motor and Aα-sensory fibers were simulated using different membrane ion channel properties (see section 2.4.1) but were defined along similar trajectories that terminate inside the gray matter (Figure 2.3). As discussed already, the differences between the Aβ-sensory activation sites and that of α-motor and Aα-sensory fibers can likely be attributed to their different trajectories, and the consequent electric potential distribution along the respective fibers (Figure 2.2C) (Rattay, 1999). The anatomical structures used in our simulations, which consequently affected the geometry of motor and sensory nerve fiber trajectories, could explain activation site differences between cervical and lumbar tSCS simulations obtained previously (Ladenbauer et al., 2010; Danner et al., 2011).

2.4.3. Comparisons with previous simulations and experimental data

In the current study, the Gaines models were used for simulating motor and sensory fibers, accounting for their physiological differences (Dawson, 1956; Kiernan, Mogyoros & Burke, 1996; Forst et al., 2015). Contrary to the results obtained by Danner and colleagues (Danner et al., 2011), the activation thresholds of motor (14 µm diameter) and sensory (16 µm diameter) fibers simulated with the MRG model (McIntyre, Richardson & Grill, 2002) were not different in our current study, despite the activation threshold of the sensory fibers appearing to be lower (Figure 2.5). It is not clear why these specific diameter sizes were used by Danner et al. (Danner et al., 2011). However, it should be noted that increasing the difference between the motor and sensory diameters within a physiological range, e.g., using 13 µm diameter for motor and 17 µm diameter for sensory, can yield larger differences between their activation thresholds. On the contrary, the sensory fibers (16 µm diameter) had significantly lower activation thresholds compared with motor fibers (14 µm diameter) when

the Gaines models were used instead (see section 2.3.3). We used the motor and sensory fibers proposed by Gaines et al. (Gaines et al., 2018), which allowed us to directly compare motor and sensory fibers with the same diameters (Figure 2.4B). Notably, our findings also expanded the work of Danner and colleagues (Danner et al., 2011) by considering trajectories of Aβ-sensory fibers with pathways defined from the dorsal roots towards rostral levels of the dorsal column.

The activation intensities estimated using the Gaines models in our simulations are numerically compatible with previous experimental studies (de Freitas et al., 2021; Sasaki et al., 2021). For instance, de Freitas et al. (de Freitas et al., 2021) showed that motor thresholds of upper-limb muscles were in the range between 35 and 70 mA, which is compatible with the range of the activation thresholds of Aα- and large Aβ-sensory fibers (i.e., activation thresholds between 25 and 60 mA in Figure 2.4B). Moreover, their results also showed that the range of stimulation amplitudes between muscle activation threshold and maximum post-activation depression was approximately 20 mA for all upper-limb muscles that were analyzed (de Freitas et al., 2021). This range is comparable with the recruitment thresholds found for Aα-sensory fibers in our current simulation study (i.e., 28 mA to 55 mA shown in Figure 2.4B), adding to validity of our computational model. Similarly, Sasaki et al. (Sasaki et al., 2021) showed that the stimulation intensity range for eliciting post-activation depression were approximately 57.0 ± 4.0 mA, also in the range of the thresholds obtained in our simulations (Figure 2.4B). Therefore, our simulation results obtained herein have a close correspondence with previous experimental studies, supporting the robustness of our model.

2.4.4. Implications for therapeutic application of cervical tSCS

Our results demonstrated the contribution of proprioceptive fibers during cervical tSCS, which has been suggested to contribute to neuromodulation (Courtine et al., 2016; Formento et al., 2018; Kumru et al., 2021) and motor rehabilitation of spinal cord injured patients (Inanici et al., 2018; Gad et al., 2018; Benavides et al., 2020). Specifically, proprioceptive fiber activation may compensate for the scarce signal transmissions during motor tasks in spinal cord injured patients (Formento et al., 2018; Rowald et al., 2022). During attempted voluntary movements, Ia-sensory fiber activation could convey excitatory inputs onto motoneurons to amplify their outputs, which could result in neuroplasticity across the spinal lesioned areas (Courtine et al., 2016; Formento et al., 2018; Rowald et al., 2022). Our finding also showed preferential activation of cutaneous fibers, indicating the potential use of cervical tSCS for the treatment of other clinical conditions. Considering the importance of cutaneous activation to the sensorimotor rehabilitation of stroke survivors (Peurala et al., 2002; Crema et al., 2022), it is possible that cervical tSCS may also be effective in post-stroke rehabilitation. Moreover, activation of Aβ-sensory fibers could activate inhibitory circuits at the spinal and supraspinal levels which attenuate nociceptive signals (Melzack & Wall, 1965; Oakley & Prager, 2002), implying possible benefits for chronic pain treatment. This reasoning is supported by the recent evidence showing utility of transcutaneous spinal direct current stimulation in chronic pain care (Guidetti et al., 2021). Irrespective of the intended application, the stimulation intensity of cervical tSCS should be configured just around the level to transsynaptically elicit motor potentials through activation of proprioceptive and cutaneous fibers without direct motor fiber activation (Hofstoetter et al., 2015b; Capogrosso et al., 2018; Benavides et al., 2020; Kumru et al., 2021). In clinical settings, this may be achieved by adjusting the stimulation intensity to elicit paresthesias (Hofstoetter et al., 2015b), which could be attained by Aβ-sensory fibers activation (Barolat et al., 1993; Greiner et al., 2021). However, it is important to note that other

parameter selection such as the duration of stimulation (Sasaki et al., 2021) and voluntary involvement during stimulation (Kumru et al., 2021) are likely required for effective neuromodulation during cervical spinal stimulation. These implications should be carefully considered when other electrode configurations (e.g., the anode electrode is placed on the iliac crests (Gad et al., 2018; Benavides et al., 2020; Inanici et al., 2021; Barss et al., 2022)) are used while continuous stimulation is delivered, since the excitability of the sensory and motor fibers could be different (Hofstoetter et al., 2015a; de Freitas et al., 2021). For instance, de Freitas et al. (de Freitas et al., 2021) suggested that nerve fiber activation thresholds are higher when the anode is placed at the iliac crests compared to the anterior neck anode placement. Moreover, facilitatory and inhibitory mechanisms, such as recurrent facilitation and inhibition, may affect the motor evoked during continuous stimulation pulses (Hofstoetter et al., 2015a) applied at frequencies used in tSCS rehabilitation protocols (Gad et al., 2018; Benavides et al., 2020; Inanici et al., 2021). However, similar groups of nerve fibers are likely activated compared to when single pulses are delivered (Zheng & Hu, 2020a). Taken together, our findings imply that the activation of Aα- and Aβ-sensory fibers during cervical tSCS likely plays a role in motor rehabilitation of spinal cord injured patients (Inanici et al., 2018; Gad et al., 2018; Benavides et al., 2020), also suggesting potential utility of this technology for treatment of other clinical conditions such as sensorimotor impairment caused by stroke (Peurala et al., 2002; Crema et al., 2022) and for chronic pain (Guidetti et al., 2021).

2.4.5. Limitations and future directions

A limitation of our 3D geometry is related to some simplifications adopted by the model. For instance, the back muscles were designed to fill the distance between the vertebra and fat, whereas the gray matter was approximated using a clyndrical shape (Figure 2.3). On

the other hand, the rootlets and the spinal canal curvature, which are the main neural tragets in our study, were developed with detailed considerations such that the dimensional curvature of the nerve fibers were fully representative (Figure 2.3). Considering the distance between the stimulating electrodes and the fibers where the electric potentials were calculated, these geometrical abstractions are considered acceptable, or perhaps even more detailed than previous simulations (Ladenbauer et al., 2010; Danner et al., 2011). In our model, we accounted for microanatomical variabilities, i.e., different fiber trajectories and diameters, which allowed for statistical analyses of the activation thresholds, consistent with previous simulation studies (Gaines et al., 2018; Greiner et al., 2021). Although such variability does not account for gross anatomical features, they enabled robust assessment of motor and sensory fiber activation threshold, which is the variable of interest in our current study (Figure 2.4 and 2.5). Future studies could consider including personalized anatomical models to account for interindividual anatomical features (Rowald et al., 2022). Future studies are nonetheless warranted to expand the complexity of the current cervical tSCS model in order to study the activation of nerve fibers at different spinal levels and using different electrode configurations.

2.5. Conclusions

Our computational simulations showed that groups of dorsal root proprioceptive Aα and cutaneous Aβ fibers were co-activated at lower stimulating intensities compared with the ventral root α-motor fibers during cervical tSCS. Preferential activation of sensory fibers can be attributed to their physiological proprieties and trajectories which define the electric potential distributions along their extent. Notably, our study demonstrated sizable cutaneous contributions during non-invasive spinal stimulation, which co-activated with the proprioceptive fibers. Understanding these neural mechanisms is critical for defining

parameters to preferentially activate dorsal root sensory fibers, an important consideration for rehabilitation effectiveness of spinal stimulation.

CHAPTER III

Selectivity and excitability of upper-limb muscle activation during cervical transcutaneous spinal cord stimulation in humans

The material presented in this chapter has been published in the article:

de Freitas RM, Sasaki A, Sayenko DG, Masugi Y, Nomura T, Nakazawa K, Milosevic M. 2021. Selectivity and excitability of upper-limb muscle activation during cervical transcutaneous spinal cord stimulation in humans. Journal of Applied Physiology 131:746–759. DOI: 10.1152/japplphysiol.00132.2021.

***NOTE**: The content of this chapter is identical to the material presented in the publication.*

CHAPTER III

Abstract

Cervical transcutaneous spinal cord stimulation (tSCS) efficacy for rehabilitation of upper-limb motor function was suggested to depend on recruitment of Ia afferents. However, selectivity and excitability of motor activation with different electrode configurations remains unclear. In this study, activation of upper-limb motor pools was examined with different cathode and anode configurations during cervical tSCS in 10 able-bodied individuals. Muscle responses were measured from six upper-limb muscles simultaneously. First, post-activation depression was confirmed with tSCS paired pulses (50 ms interval) for each cathode configuration (C6, C7, and T1 vertebral levels), with anode on the anterior neck. Selectivity and excitability of activation of the upper-limb motor pools were examined by comparing the recruitment curves (10-100 mA) of first evoked responses across muscles and cathode configurations. Our results showed that hand muscles were preferentially activated when the cathode was placed over T1 compared to the other vertebral levels, while there was no selectivity for proximal arm muscles. Furthermore, higher stimulation intensities were required to activate distal hand muscles than proximal arm muscles, suggesting different excitability thresholds between muscles. In a separate protocol, responses were compared between anode configurations (anterior neck, shoulders, iliac crests, and back), with one selected cathode configuration. The level of discomfort was also assessed. Largest muscle responses were elicited with the anode configuration over the anterior neck, while there were no differences in the discomfort. Our results therefore inform methodological considerations for electrode configuration to help optimize recruitment of Ia afferents during cervical tSCS.

Keywords: cervical; transcutaneous spinal cord stimulation; post-activation depression; upper-limbs; reflex.

CHAPTER III

3.1. Introduction

Epidural stimulation of cervical spinal cord has been used to restore upper-limb movements after spinal cord injury (SCI) (Lu et al., 2016). Similarly, non-invasive cervical transcutaneous spinal cord stimulation (tSCS) has recently gained considerable interest in rehabilitation of upper-limb motor function after SCI (Inanici et al., 2018; Gad et al., 2018; Freyvert et al., 2018; Benavides et al., 2020). While both approaches may activate common neural structures within the spinal cord (Hofstoetter et al., 2018), the extent of selectivity of activation of upper-limb muscles using different cathode and anode configurations with tSCS remains unclear.

Electrical impulses reaching the spinal cord using either surface or implanted electrodes can activate monosynaptic and oligosynaptic connections between sensory afferents and α-motoneurons (Danner et al., 2011; Capogrosso et al., 2013; Hofstoetter et al., 2018). Such transsynaptic activation of muscles may compensate for the scarce, or even absent, proprioceptive information during motor tasks in individuals with SCI (Gad et al., 2018; Wagner et al., 2018; Formento et al., 2018). Specifically, excitation of Ia monosynaptic pathways was suggested to be critical for strengthening descending commands through the spinal lesioned site to caudal levels, and may promote reorganization of neural motor pathways (Park et al., 2008; Formento et al., 2018; Murray & Knikou, 2019; Courtine & Sofroniew, 2019). Paired pulses delivered using tSCS with short inter-stimulus intervals (e.g., 50 ms) can be used to test the excitation of Ia monosynaptic pathways by confirming suppression of the second evoked response in relation to the first (Minassian et al., 2007; Milosevic et al., 2019b). Although other sensory fibers and interneurons may also be excited, it was previously suggested that suppression may primarily be attributed to post-activation depression (Pierrot-Deseilligny & Burke, 2005). Such mechanism can be used to confirm the reflex nature of these evoked responses (Hofstoetter et al., 2018; Milosevic et al., 2019b).

CHAPTER III

Selectivity of the electrical stimulation to specific spinal regions as well as excitability to recruitment of motor pools were suggested to be important for enhancing rehabilitation effects after SCI (Wagner et al., 2018; Formento et al., 2018; Greiner et al., 2021). It has recently been demonstrated that continuous cervical tSCS may selectively yield independent and coordinated movements in proximal and distal upper-limb joints (Zheng & Hu, 2020b). Additionally, cervical tSCS was shown to elicit post-activation depression in the spinally evoked motor responses with both intact (Milosevic et al., 2019b; Zheng & Hu, 2020a) and SCI (Wu et al., 2020) individuals. Various cervical tSCS configurations have been used for targeting upper-limb muscles. Cathode electrodes were typically configured medially over the C3-T4 vertebral regions on the posterior side of the neck (Inanici et al., 2018; Gad et al., 2018; Milosevic et al., 2019b; Wu et al., 2020), while the upper-limb motor pools were suggested to be arranged rostral to T1 vertebra (Kendall et al., 2005; Cramer & Darby, 2014; Cadotte et al., 2015). Anode electrodes were placed over the anterior neck (Milosevic et al., 2019b; Wu et al., 2020), clavicles (Murray & Knikou, 2017; Islam et al., 2020), iliac crests (Inanici et al., 2018; Gad et al., 2018; Freyvert et al., 2018; Benavides et al., 2020), or the back (Massey et al., 2018; Villar Ortega et al., 2019). However, since these studies applied cervical tSCS for different proposes (e.g., SCI rehabilitation or for assessment of motor responses), as well as with different stimulation paradigms (e.g., trains of pulses or single pulses), direct comparison between electrode configurations is not possible. Furthermore, selectivity and excitability of electrode configurations on the transsynaptic activation of the upper-limb muscles have not been examined. Better understanding of the evoked responses can inform methodological considerations to help optimize recruitment of Ia afferents.

In the present study, we therefore assessed spinally evoked muscle responses in multiple upper-limb muscles with cervical tSCS delivered using different cathode and anode electrode configurations. First, post-activation depression in the evoked responses was confirmed in all

analyzed muscles for the cathode electrode placed over C6, C7, and T1 vertebral levels while the anode was fixed over the anterior neck. The selectivity of spinal regions and excitability to the recruitment of motoneurons during cervical tSCS were then compared between the three cathode configurations using recruitment curves (Study 1). Specifically, in this study, selectivity is referred to as activation of motor pools in different spinal regions using different cathode locations (C6, C7, and T1), and excitability as the susceptibility to which motoneurons are recruited during cervical tSCS. In a separate protocol (Study 2), four anode configurations were compared by varying the anodes over the anterior neck (Milosevic et al., 2019b; Wu et al., 2020), distal end of clavicles (Murray & Knikou, 2017; Islam et al., 2020), iliac crests (Inanici et al., 2018; Gad et al., 2018; Freyvert et al., 2018; Benavides et al., 2020), or the back (Massey et al., 2018; Villar Ortega et al., 2019).

Based on theoretical mechanisms underlying motor activation during tSCS and previous experimental studies, we hypothesized that post-activation depression would be observed in all muscles for all cathode configurations. Moreover, based on the anatomy and myotome maps of the cervical spinal cord (Kendall et al., 2005; Cramer & Darby, 2014), we further hypothesized that tSCS would preferentially evoke responses in proximal arm muscles with cathode configured more rostrally over the C6 level, and distal hand muscles with cathodes more caudally, over T1 level. Specifically, considering the organization of hand muscles motor pools in more caudal spinal levels compared to the arm muscles (Kendall et al., 2005), the use of relatively large cathode electrodes placed over the C6 vertebra (overlapping C6 and C7 spinal levels) and T1 vertebra (overlapping C8 and T1 spinal levels) was therefore expected to yield different levels of activation of distal and proximal upper-limb muscles. Moreover, placing the cathode electrode over C7 vertebra (overlapping C7 and C8 spinal levels) would serve as an intermediate level for confirming the selectivity of distal and proximal muscles when the cathode is varied to rostral (C6) and caudal (T1) levels. This would be analogous to

what has been demonstrated with lumbar tSCS in the lower-limb muscles (Minassian et al., 2007; Roy, Gibson & Stein, 2012; Krenn et al., 2013; Sayenko et al., 2015a). We further hypothesized that greater recruitment of upper-limb muscles would be yielded by configuring the anode over the anterior neck (Milosevic et al., 2019b; Wu et al., 2020) due to the proximity to the cathode which may maximize the electric field flow across the spinal cord.

3.2. Methods

3.2.1. Participants

Ten able-bodied male individuals were recruited for this study. The age, weight, and height of the participants were: 25.8±2.6 years, 68.8±8.3 kg, and 173.4±5.1 cm (mean±SD), respectively. All participants were right-handed in accordance with the Edinburgh Handedness Inventory (scores across participants were between 0.55 and 1, where 1 indicates completely right-handed and −1 indicates completely left-handed) (Oldfield, 1971). None of the participants had a history of neurological and/or musculoskeletal impairments. All participants gave written informed consent in accordance with the Declaration of Helsinki prior to participating in the study. The experimental procedures were approved by the local institutional ethics committee of the Graduate School of Arts and Science at The University of Tokyo.

3.2.2. Data acquisition

Electromyographic (EMG) signals were recorded using Ag/AgCl surface electrodes (Vitrode F-150S, Nihon Kohden, Tokyo, Japan) simultaneously from upper-limb muscles on the right (dominant) hand, since handedness and hand dominance may affect motor responses (Sathiamoorthy & Sathiamoorthy, 1990; Pereira et al., 2012; Gordon et al., 2012). Electromyographic signals from six muscles innervated by cervical spinal levels were recorded on: (1) biceps brachii (BB), innervated by C5-C6 spinal levels; (2) triceps brachii (TB),

innervated by C6-T1 spinal levels; (3) flexor carpi radialis (FCR), innervated by C6-C7 spinal levels; (4) extensor carpi radialis (ECR), innervated by C5-T1 spinal levels; (5) first dorsal interosseous (FDI), innervated by C5-T1 spinal levels; and (6) abductor pollicis brevis (APB), innervated by C5-T1 spinal levels (Kendall et al., 2005; Milosevic et al., 2019b). Specifically, two electrodes were placed over the belly of each muscle with an inter-electrode distance of approximately 20 mm, while the ground electrode was placed around the lateral epicondyle (Milosevic et al., 2019b). Prior to application of electrodes, the skin was cleaned using alcohol to reduce skin impedance.

All EMG signals were amplified (×1,000) using a bipolar configuration and band-pass filtered between 5 and 1,000 Hz using a multichannel EMG amplifier (MEG-6108, Nihon Kohden, Tokyo, Japan). Moreover, the EMG signals were digitized at a sampling frequency of 4,000 Hz using an analog-to-digital converter (Powerlab/16SP, AD Instruments, Castle Hill, Australia) and stored on the computer for post-processing.

3.2.3. Experimental protocol

During the experiment, participants remained at rest in the supine position with both arms resting on the bed along the body (Figure 3.1A). A small pillow was placed under the neck to ensure that the head was rested comfortably and that tSCS electrodes remained fixed. The tSCS stimuli were applied by delivering two monophasic pulses with an inter-stimuli interval of 50 ms of equal pulse amplitudes and 2 ms pulse width (Milosevic et al., 2019b) using a constant current electrical stimulator (DS7A, Digitimer, Welwyn Garden City, UK). The two evoked responses elicited by the stimuli were recorded at each muscle simultaneously. For each participant, the experimental protocol of Study 2 was conducted following Study 1 in a single experimental session, while at least 10 min rest was given between experiments.

3.2.3.1. Cathode electrode configurations (Study 1)

Study 1 was conducted to confirm post-activation of evoked responses in multiple upper-limb muscles with different cathode electrode configurations, and to further investigate the selectivity to spinal regions and excitability of recruitment of motoneurons during cervical tSCS. Three configurations were compared by positioning the cathode electrode (5 x 5 cm) on the skin surface of the posterior side of the neck centered over the spinous process of: (1) C6; (2) C7; and (3) T1 vertebrae, while the anode electrode (7.5 x 10 cm; horizontally positioned) remained fixed along the midline on the anterior side of the neck (Figure 3.1A), consistent to Milosevic et al. (Milosevic et al., 2019b). Specifically, stimulating pulses were applied (see section 3.2.3) and the stimulating current amplitude was varied from 10 to 100 mA, in 10 mA increments (Kitano & Koceja, 2009; Roy, Gibson & Stein, 2012). Large size electrodes were used to alleviate the pain felt by the participants during the stimulation. Nonetheless, the maximal current amplitude stimulated in two participants was below 100 mA (90 mA and 80 mA) due to discomfort during stimulation. For all participants, three responses (Danner et al., 2016) were recorded for each stimulation amplitude with intervals of 10-15 s to obtain the recruitment curves as depicted in the Figure 3.2 for each muscle (BB, TB, FCR, ECR, FDI, and APB) and each cathode configuration (C6, C7, and T1), analogous to a previous study examining lower-limb muscles (Sayenko et al., 2015a). The order of cathode configurations (C6, C7, and T1) was randomized between participants and a break of at least 3 min was administered between conditions.

3.2.3.2. Anode electrode configurations (Study 2)

After completion of the Study 1 experimental protocol, a cathode location (C6, C7, or T1) and stimulation amplitude were chosen for each subject to be used in the subsequent

experiments of Study 2. The experimenter identified the cathode location and stimulation intensity which could yield a suppression of the second responses in relation to the first (i.e., post-activation depression) simultaneously in all muscles by visual inspection of the data recorded during Study 1. Specifically, the location and stimulation amplitude were chosen to be on the ascending part of the recruitment curve, when the second response had a smaller peak-to-peak amplitude compared to the first response simultaneously for all six muscles, as previously described by Milosevic et al. (Milosevic et al., 2019b). The chosen cathode location and stimulus amplitude were then used for experiments in Study 2 (cathode location C6: n=0, C7: n=2, T1: n=8; current amplitude mean±SD: 65.0±10.8 mA). These locations are similar to those used previously when the anode was configured over the neck (Milosevic et al., 2019b), shoulders (Islam et al., 2020), iliac crests (Inanici et al., 2018) and the back (Massey et al., 2018). The choice of the cathode location and stimulus amplitude was confirmed in post-processing (see section 3.3.2).

Study 2 was conducted to investigate post-activation depression in different anode electrode configurations elicited in multiple upper-limb muscles. Two monophasic pulses were applied (see section 3.2.3.) at the chosen cathode location and stimulus amplitude to compare the four different anode configurations illustrated in Figure 3.1B: (1) one anode electrode (7.5 x 10 cm) located on the midline of the anterior side of the neck (Neck) (Milosevic et al., 2019b; Wu et al., 2020); (2) two anode electrodes (5 x 5 cm) located bilaterally over the distal end of the clavicles (Shoulders) (Murray & Knikou, 2017; Islam et al., 2020); (3) two anode electrodes (5 x 5 cm) located bilaterally over the iliac crests (Iliac Crests) (Inanici et al., 2018; Gad et al., 2018; Freyvert et al., 2018; Benavides et al., 2020); (4) one anode electrode (5 x 5 cm) located approximately 4 cm below the cathode electrode on the posterior side of the neck (Back) (Massey et al., 2018; Villar Ortega et al., 2019). Three responses (Danner et al., 2016) for each anode configuration were recorded with intervals of 10-15 s. The order of conditions (Neck,

Shoulder, Iliac Crest, and Back) was randomized between participants and a break of at least 3 min was administered between conditions.

A numeric rating scale (NRS) was used to evaluate self-reported pain from 0 to 10, where 0 corresponds to “no pain” and 10 corresponds the “worst pain imaginable” (Hawker et al., 2011). The pain level was evaluated by showing participants a visual analog scale and asking them to rate the pain experienced during stimulation delivered with each anode configuration immediately after each protocol (Neck, Shoulder, Iliac Crest and Back).

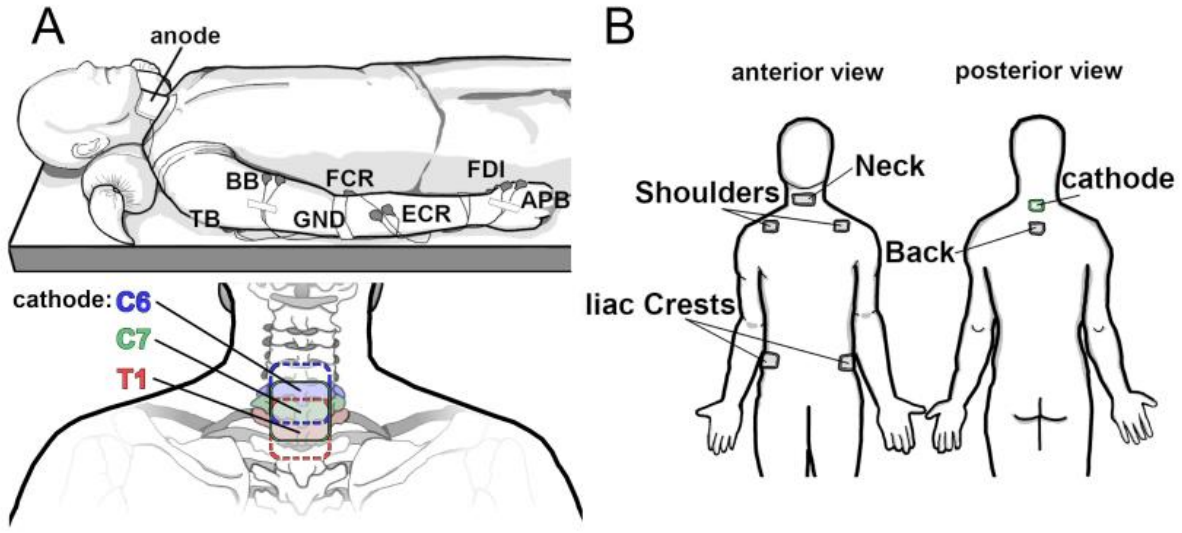

Figure 3.1 – Experimental setups: Illustration of the experimental setups of (A) Study 1; and (B) Study 2. The upper image of (A) illustrates the cervical tSCS applied with anode placed over the anterior neck while the EMG signals were recorded from biceps brachii (BB), triceps brachii (TB), flexor carpi radialis (FCR), extensor carpi radialis (ECR), first dorsal interosseous and abductor pollicis brevis (APB), while the ground electrode (GND) was fixed around the elbow. In the bottom image of (A), the configuration of the cathode electrode over C6, C7, and T1 vertebral levels are shown. In (B), the Neck, Shoulders, Iliac Crests and Back configurations of anodes are illustrated.

3.2.4. Data analysis

In post-processing, which was performed using a custom written MATLAB script (MathWorks, Natick, MA), the peak-to-peak amplitudes were measured from the first and second evoked responses to the pair of pulses of each muscle. The peak-to-peak amplitude of the first and second responses within three pairs of pulses delivered for each stimulus amplitude were averaged (Danner et al., 2016). The averaged values were then used to analyze the activation of upper-limb muscles for different cathode (Study 1) and anode (Study 2) electrode configurations.

3.2.4.1. Cathode electrode configuration

Post-activation depression

To evaluate tSCS post-activation depression in the second responses compared to the first (Minassian et al., 2007; Courtine et al., 2007; Sayenko et al., 2015b; Milosevic et al., 2019b) for different cathode locations (C6, C7, and T1) using data obtained in Study 1, the following parameters were analyzed (Figure 3.2): (i) peak-to-peak amplitudes of the first and second responses at their maximum difference were compared across cathode configurations for each muscle individually; (ii) maximum normalized difference of the second peak-to-peak evoked response compared to the first response (D_{MAX}), which was calculated as $D_{MAX} = max((F[X] - S[X])/F[X])$, where $F[X]$ and $S[X]$ correspond to the first and second experimentally obtained responses at $X = 10, \dots, 100$ mA; and (iii) stimulus intensity at the maximum post-activation depression (X_D), which was the stimulating current intensity at D_{MAX}. These variables, which represent the maximal normalized post-activation depression on the recruitment curve (D_{MAX}) and the corresponding stimulus intensity of the maximal post-activation depression (X_D), were compared between muscles and cathode configurations.

CHAPTER III

Recruitment curves

In Study 1, for each cathode configuration (C6, C7, and T1 levels, while the anode was fixed on the anterior side of the neck), the average peak-to-peak amplitudes obtained for each stimulation intensity (10 to 100 mA, in 10 mA increments) was used to obtain the recruitment curve of the first responses for each muscle (BB, TB, FCR, ECR, FDI, and APB) for each participant. Specifically, data for each recruitment curve were first normalized to the maximum value elicited between the three cathodes configurations. The signal-to-noise ratio of these responses were compared between muscles, and the results showed no statistically significant differences ($F(5,45)=1.81$, $p = .130$). Normalized responses were then fitted using a Boltzmann sigmoidal function (Devanne, Lavoie & Capaday, 1997; Smith, Rymer & Knikou, 2015; Murray & Knikou, 2019):

$$RC(x) = \frac{PL}{1 + e^{\frac{(X_{50} - x)}{K}}} \tag{3.1}$$

where the recruitment curve, *RC*, is a function of the stimulus intensity, x, while parameter PL is the function's maximum value (plateau), X_{50} is the stimulus intensity at 50% of the plateau value, and K is a slope parameter. For sigmoid fits that yielded the plateau value greater than 2 (i.e., fits that extrapolated features not implicitly represented by the experimental data), data were re-fitted by defining $X_{50} = 100\ mA$ as the initial condition for the fitting (23 out of 180 cases). If the sigmoid functions plateau still remained greater than 2 after re-fitting, the data were discarded from the analysis (4 out of 180 cases) as it was deemed that the fit could not represent the data. Moreover, it was verified that the coefficient of determination (R^2) was greater than 0.9 for each sigmoid fit (mean±SD: 0.99±0.01) (Devanne, Lavoie & Capaday, 1997; Capaday, 1997; Sekiguchi, Nakazawa & Suzuki, 2003). After the recruitment curve

functions were obtained, four parameters were extracted from each fit, as shown in Figure 3.2: (1) threshold stimulus intensity to motor activation (X_{TH}), indicating the excitability to the initial recruitment of motoneurons; (2) maximum slope (*SL*), indicating the excitability to the recruitment of motoneurons with the increase of stimulation current amplitude; (3) stimulus intensity at 50% of the plateau (X_{50}), serving as a comparative index between the excitability to the initial recruitment of motoneurons (X_{TH}) and the increase of current amplitude (*SL)*; (4) plateau (*PL*), indicating the total motor output. The parameters *PL* and X_{50} were obtained from the output of the fitting algorithm, *SL* was calculated as *PL/4K* , and X_{TH} was obtained from the line equation defined by X_{50}, $PL/2$ and *SL*, as described previously (Devanne, Lavoie & Capaday, 1997; Capaday, 1997; Smith, Rymer & Knikou, 2015; Murray & Knikou, 2019).The selectivity of activation of different upper-limb muscles was compared between cathode configurations (C6, C7, and T1) through the excitability parameters *SL*, X_{50} and X_{TH} and motor output parameter, *PL*.

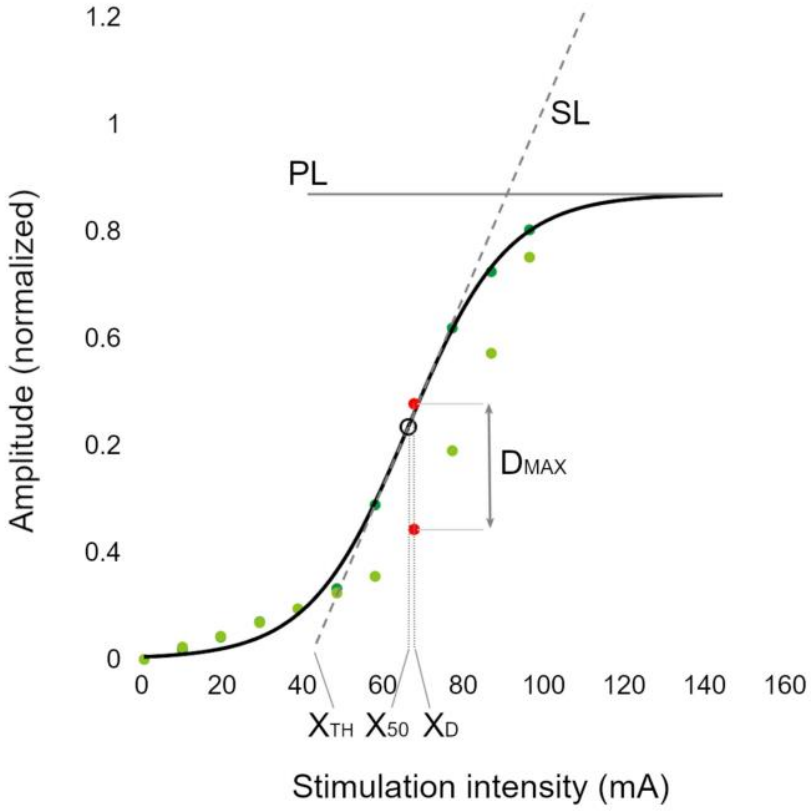

Figure 3.2 – Parameters analyzed from the sigmoid functions fit to the recruitment curves: Boltzmann sigmoid function fitted to the recruitment curve (black line) of the peak-to-peak amplitude of the first responses (dark green circles) of a representative muscle evoked using cervical tSCS stimulating currents from 10 mA to 100 mA (increments of 10 mA) with the cathode electrode placed over the C7 vertebral level. The parameters extracted from the sigmoid fit: slope (*SL*), plateau (*PL*), stimulus intensity at 50% of the plateau (X_{50}), and threshold stimulus intensity (X_{TH}) are indicated. Additionally, the second evoked responses (light green circles) are shown. Using the peak-to-peak amplitude of the first and second responses, the maximal normalized suppression (D_{MAX}) and the current intensity where the maximal suppression occurred (X_D) are indicated. For each stimulation intensity, each a pair of data points consists of average peak-to-peak values of three pairs of stimulation pulses (50 ms inter-stimuli interval). Comparisons were performed between different upper-limb muscles (BB, TB, FCR, ECR, FDI, and APB) and different cathode locations (C6, C7, and T1).

3.2.4.2. Anode electrode configurations

First, the post-activation depression in the second responses elicited at the stimulus intensity and cathode location chosen by the experimenter for each participant to be used in Study 2 (see section 3.2.3.2.) was confirmed in using data recorded in Study 1. Since post-processing confirmed correct selection of stimulus intensity and cathode location parameters (see section 3.3.2.), the peak-to-peak amplitudes of the first and second responses elicited with different anode configurations (Neck, Shoulders, Iliac Crests, and Back) were compared to

evaluate effects of different anode configurations on the transsynaptic activation of each muscle in Study 2.

3.2.5. Statistics

First, for each muscle separately, a within-subjects design two-way ANOVA was used to compare the peak-to-peak amplitudes of the first and second responses at maximum suppression (post-activation depression: first and second response) between cathode configurations (cathode: C6, C7, and T1). Additionally, to compare post-activation depression, D_{MAX} and X_D were also analyzed using a within-subjects design two-way ANOVA to compare responses between muscles (muscle: BB, TB, FCR, ECR, FDI, and APB) and different cathode locations (cathode: C6, C7, and T1). The selectivity of activation of upper-limb muscle motor pools with different cathode configurations were analyzed by comparing excitability parameters *SL*, X_{50} and X_{TH} and motor output parameter, *PL*, using a within-subjects design two-way ANOVA between cathode locations (cathode: C6, C7, and T1) across different muscles (muscle: BB, TB, FCR, ECR, FDI, and APB).

The post-activation depression in the second responses elicited with stimulus intensity and cathode configurations used for each participant in Study 2 (see section 3.2.3.2. and section 3.2.4.3.) was analyzed using a t-test to compare the first and second response amplitudes for each muscle separately. In Study 2, a within-subject design two-way ANOVA was used to compare different anode configurations (anode: Neck, Shoulder, Iliac Crests and Back) and suppression of the second response compared to the first (post-activation depression: first and second response) for each muscle separately.

When significant interactions were found on the two-way ANOVA, a within-subject design one-way ANOVA (or a t-test) was performed for each factor separately. Post-hoc multiple

comparisons were conducted when significant ANOVA results were found and adjusted using the Bonferroni correction factor. Greenhouse-Geisser correction was used when the sphericity assumption was violated, which was confirmed using the Mauchly's test. Normality of data distributed was tested using the Shapiro-Wilk's test prior to performing the analysis. Although most of the data were found to be normally distributed, the results of non-normally distributed data were confirmed using the non-parametric equivalent Friedman's test and Wilcoxon test. Furthermore, the NRS scores for different anode configurations were compared using Friedman's test, since it is an ordinal variable. All statistical tests were performed using SPSS (IBM, Armonk, NY) with a significance level of $\alpha = .05$.

3.3. Results

3.3.1. Cathode electrode configurations (Study 1)

Averaged evoked responses of a representative participant in Study 1 for different cathode configurations (C6, C7, and T1) across stimulus intensities varying from 10 to 100 mA are shown in Figure 3.3. For this representative participant, post-activation depression can be seen in most muscles. Distal hand muscles (FDI and APB) were preferentially activated when the cathode was placed over T1 compared to C6 and C7 vertebral levels, while that was not true for the proximal arm muscles (BB, TB, FCR and ECR). Moreover, higher stimulation intensities were required to elicit responses in distal muscles (FDI and APB) compared to proximal muscles (BB, TB, FCR and ECR).

CHAPTER III

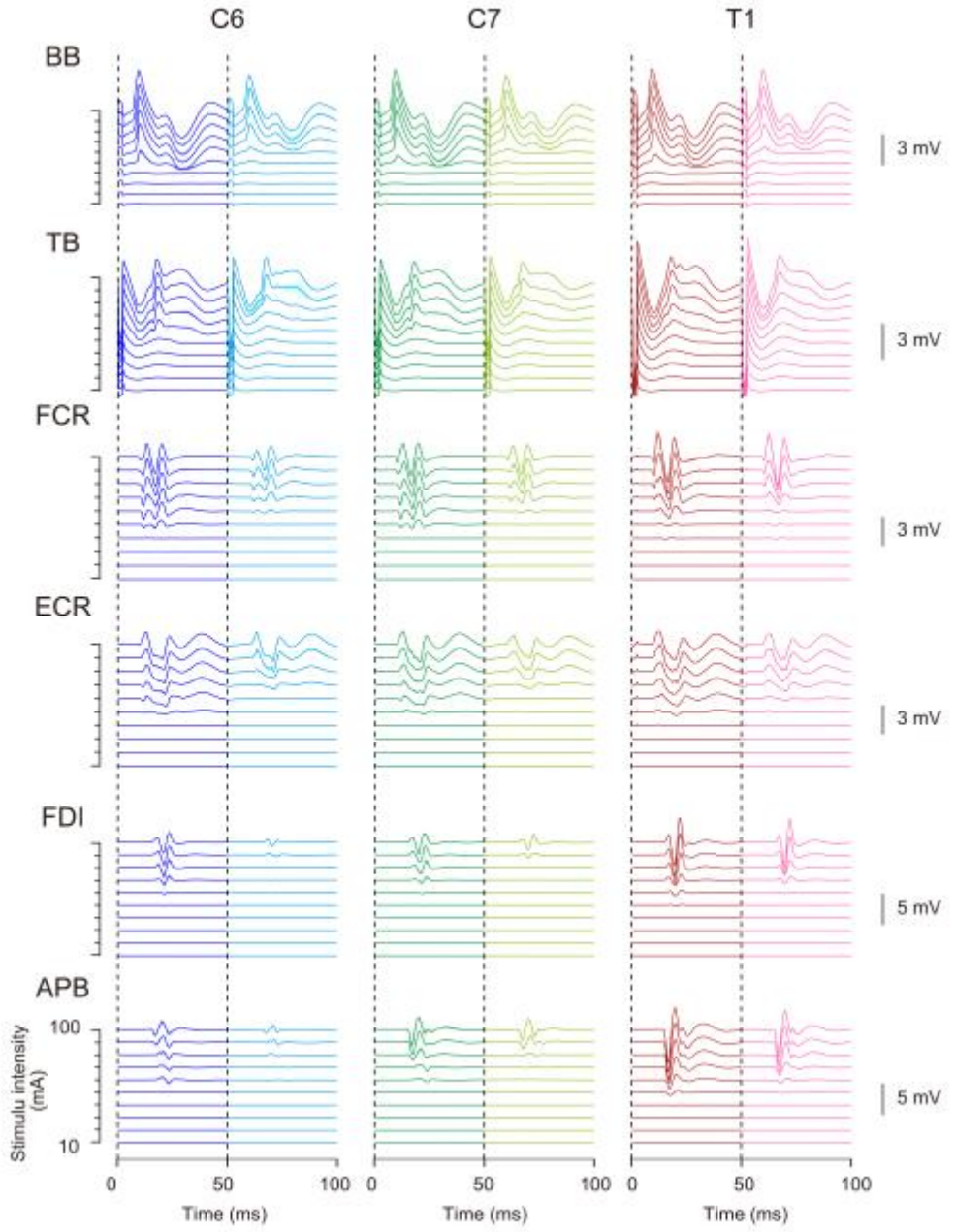

Figure 3.3 – Representative cervical tSCS evoked responses using different cathode configurations: Representative participant averaged responses evoked in the six muscles (BB, TB, FCR, ECR, FDI, and APB) using cervical tSCS with the anode was placed over the anterior neck and the cathode placed over C6, C7, and T1 vertebral levels. Three responses elicited with stimulations delivered as two monophasic pulses (50 ms inter-stimuli interval) were averaged for each stimulation amplitude (from 10 mA to 100 mA, in increments of 10mA) and cathode configuration. The first and second averaged responses elicited with the cathode placed over C6, C7, and T1 are shown for each muscle. Each trace corresponds to the averaged EMG time series with amplitudes varying from 10 mA (bottom) to 100 mA (top), where the darker shade color indicates the first elicited response and the lighter shade color the second response. The shaded areas in the corresponding colors indicate the standard deviation of the three responses. The dotted lines indicate the instant at which the first and second stimuli were delivered.

CHAPTER III

Post-activation depression

Results obtained from the comparison of the maximum peak-to-peak amplitude difference between the second and first responses (post-activation depression: first vs. second responses) with three cathode configurations (cathode: C6, C7, and T1) for each muscle are summarized in Figure 3.4, while Table 3.1 shows the main statistical results. For BB, TB, FCR, and ECR, two-way ANOVA showed no significant interactions and statistically significant main effect for post-activation depression, but not for cathode comparisons. For FDI and APB, since interactions were shown, follow-up analyses with one-way ANOVA or t-tests indicate statistically significant post-activation depression for all cathode configurations; moreover, cathode comparisons showed that the first and second responses were different for the APB muscle only. In Figure 3.4, post-hoc multiple comparisons further indicate differences in the first and second responses between C6 and T1 for the APB muscle.

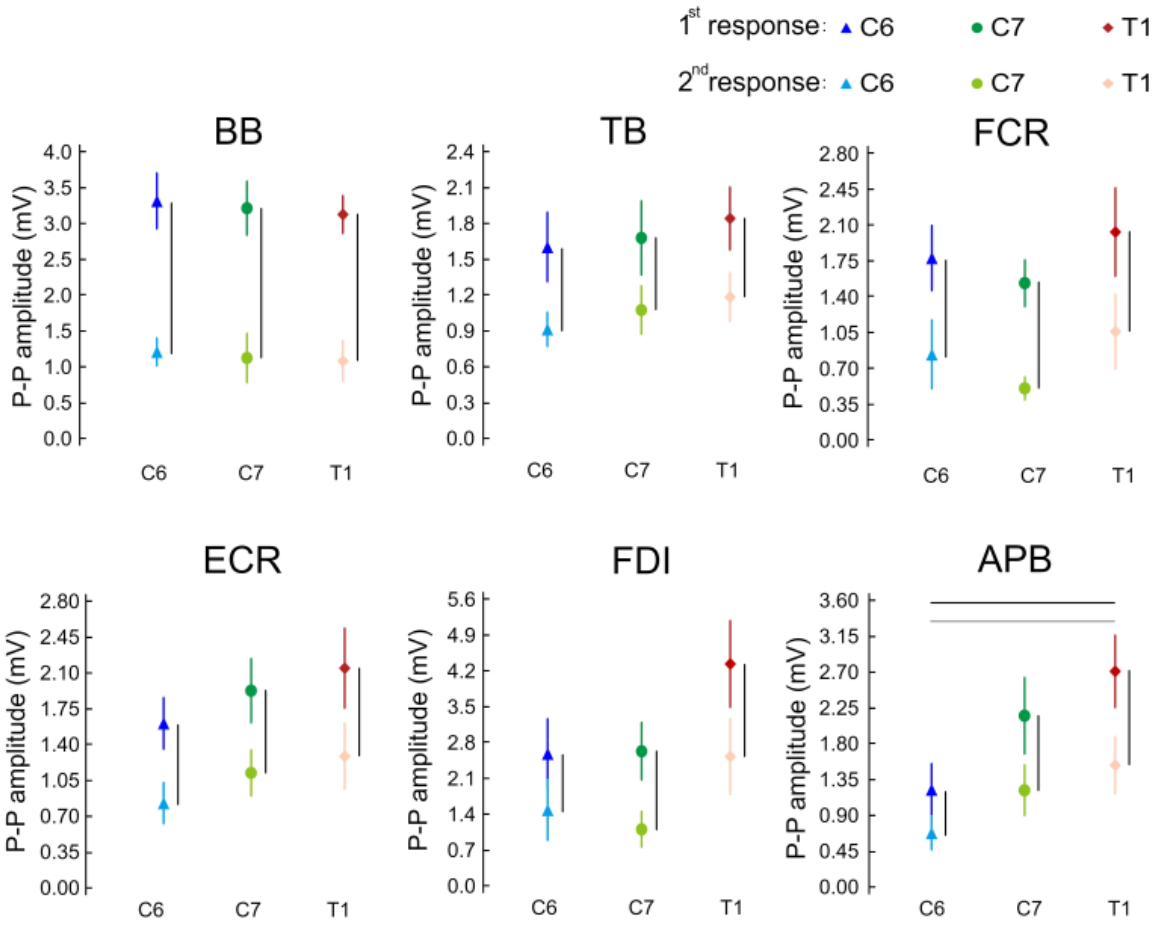

Figure 3.4 – Post-activation depression responses using different cathode configurations: The mean values of the responses at the maximal suppression point are indicated with blue triangles, green circles, and red diamonds for C6, C7, and T1, respectively. Shown are the corresponding standard error vertical bars. The sample size of each data sets is n = 10. The dark shades represent the first responses, and the light shades represent the second responses. Significant differences between cathode configurations are indicated with black and gray bars for the first and second responses, respectively. Significant differences between the first and second responses are indicated with vertical black bars.

Table 3.1: Statistical analyses results showing within subject two-way ANOVA interactions and main effect results for post-activation depression (first and second responses) and cathode configurations (C6, C7, and T1) comparisons of the responses evoked in each muscle (BB, TB, FCR, ECR, FDI, and APB) separately. When interaction was significant, the factors were compared separately with within subject one-way ANOVA or a t-test. Greenhouse-Geisser correction was used when the sphericity assumption was violated. The *p* values in bold indicate significant differences for a significance level of $\alpha = .05$.

	interaction	**post-activation depression**			**cathode**	
		C6	**C7**	**T1**	**First**	**Second**
BB	F (2,18)=0.1 *p*=.872		**F (1,9)=35.1 *p*<.001**		F (2,18)=0.2 *p*=.799	
TB	F (2,18)=0.7 *p*=.526		**F (1,9)=13.2 *p*=.005**		F (2,18)=0.8 *p*=.454	
FCR	F (2,18)=0.5 *p*=.646		**F (1,9)=28.7 *p* <.001**		F (2,18)=2.5 *p*=.114	
ECR	F (1.2,10.9)=0.3 *p*=.618		**F (1,9)=26.8 *p*<.001**		F (2,18)=1.6 *p*=.237	
FDI	**F (2,18)=5.4 *p*=.015**	**t(9)=4.2 *p*=.002**	**t (9)=5.2 *p*<.001**	**t (9)=6.3 *p*<.001**	F (2,18)=2.9 *p*=.080	F (2,18)=2.3 *p*=.128
APB	**F (1.2,10.6)=8.8 *p*=.011**	**t (9)=3.3 *p*=.009**	**t (9)=4.4 *p*=.002**	**t (9)=5.0 *p* <.001**	**F (2,18)=9.3 *p*=.002**	**F (2,18)=4.2 *p*=.031**

Results obtained from the analyses of the two parameters examined for the maximum post-activation depression (D_{MAX} and X_D) are summarized in Figure 3.5A, while Table 3.2 summarizes the main statistical results. For both D_{MAX} and X_D, the two-way ANOVA showed no significant interactions and statistically significant main effects for muscle, but not for cathode comparisons. In Figure 3.5A, post-hoc multiple comparisons between muscles indicated differences between BB and TB for D_{MAX} (NOTE: despite statistical significance in the two-way ANOVA for X_D, post-hoc analyses with Bonferroni correction did not show significant differences).

Table 3.2: Statistical analyses results showing within subject two-way ANOVA interactions and main effect results for cathode (C6, C7, and T1) and muscle (BB, TB, FCR, ECR, FDI, and APB) comparisons of post-activation depression (D_{MAX} and X_D) and recruitment curve parameters (SL, PL, X_{50}, and X_{TH}). When interaction was significant, the factors were compared separately with within subject one-way ANOVA. Greenhouse-Geisser correction was used when the sphericity assumption was violated. The p values in bold indicate significant differences for a significance level of $\alpha = .05$.

	interaction	**cathode**						**muscle**		
		BB	**TB**	**FCR**	**ECR**	**FDI**	**APB**	**C6**	**C7**	**T1**
D_{MAX}	F(10,90)=1.0 *p*=.453			F(2,18)=2.2 *p*=.144					**F(5,45)=6.0 *p*<.001**	
X_D	F(3.0,26.9)=0.8 *p*=.502			F(1.3,11.5)=2.0 *p*=.183					**F(3.0,27.1)=3.8 *p*=.032**	
SL	**F(10,80)=4.0 *p*<.001**	F(1.2,10.9)=0.4 *p* =.574	F(2,16)=0.8 *p*=.478	F(1.2,11.2)=1.8 *p*=.201	F(1.2,9.9)=0.9 *p*=.381	**F(2,16)=13.3 *p*<.001**	**F(2,16)=18.8 *p*<.001**	F(1.8,14.6)=3.0 *p*=.084	F(1.7,15.7)=1.2 *p*=.314	**F(5,40)=6.2 *p*<.001**
PL	**F(10,80)=2.2 *p*=.025**	**F(2,18)=4.4 *p*=.028**	F(2,16)=1.0 *p*=.387	F(2,18)=1.5 *p*=.242	F(2,16)=1.2 *p*=.321	**F(2,16)=8.4 p=.003**	**F(2,16)=7.5 *p*=.005**	**F(5,40)=2.9 *p*=.025**	F (5,45)=1.7 *p*=.158	F(2.5,19.8)=1.1 *p*=.345
X_{50}	**F(10,80)=1.9 *p*=.049**	F(2,18)=1.0 *p*=.385	F(2,16)=1.2 *p*=.323	F(1.2,11.2)=1.0 *p*=.339	F(2,16)=1.2 *p*=.336	F(2,16)=2.5 *p*=.109	**F(2,16)=5.1 *p*=.019**	**F(5,40)=7.9 *p*<.001**	**F (5,45)=6.6 *p*<.001**	**F(5,40)=3.3 *p*<.001**
X_{TH}	**F(10,80)=2.0 *p*=.039**	F(2,18)=0.4 *p*=.666	F(2,16)=0.9 *p*=.420	F(2,18)=0.5 *p*=.618	F(2,16)=1.8 *p*=.198	**F(2,16)=5.7 *p*=.013**	F(2,16)=2.4 *p*=.124	**F(5,40)=16.0 *p*<.001**	**F(2.7,24.4)=12.4 *p*<.001**	**F(5,40)=8.9 *p*<.001**

Recruitment curves

Results obtained from the analyses of the four parameters extracted from the sigmoid fits of the recruitment curves: SL, PL, X_{TH}, and X_{50} are summarized in Figure 3.5B, while Table 3.2 summarizes the main statistical results. For SL, PL, X_{TH}, and X_{50}, since interactions were shown, follow-up analyses with one-way ANOVA indicate mostly significant differences between cathodes for the FDI and APB muscles; moreover, muscle comparisons showed mostly significant differences for X_{TH} and X_{50}. In Figure 3.5B, post-hoc multiple comparisons showed significant differences between cathodes configurations indicating that distal hand muscles (FDI and APB) were preferentially activated when the cathode was placed over T1 compared to C6 and C7 vertebral levels (c.f. PL in Figure 3.5B), while this was not true for the proximal arm muscles (BB, TB, FCR and ECR) (NOTE: despite statistical significance in the one-way ANOVA for PL and X_{TH} across muscles, and for X_{TH} and X_{50} across different cathodes configurations, post-hoc analyses with Bonferroni correction did not show significant differences).

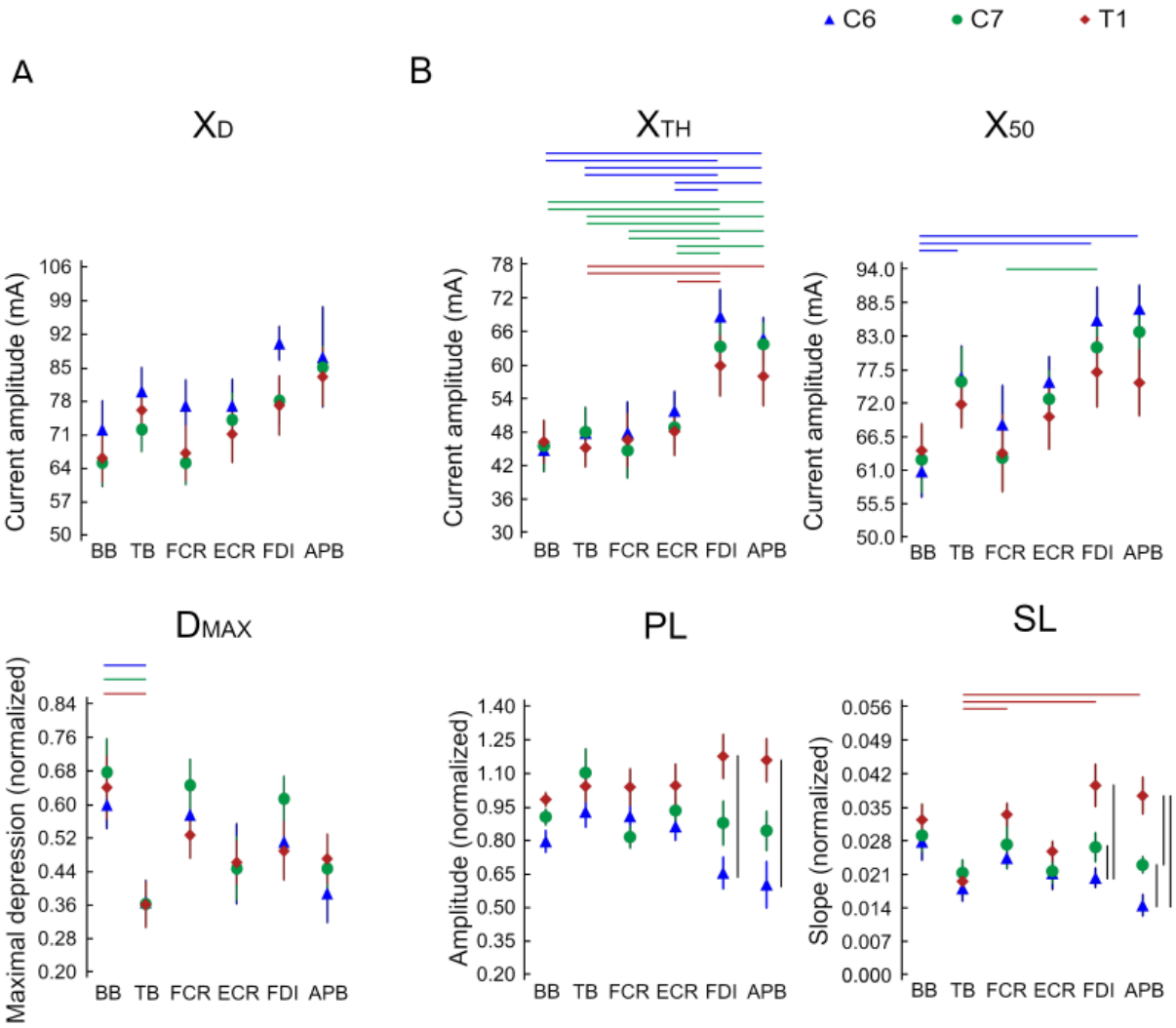

Figure 3.5 – Comparisons between different cathode configurations: (A) Post-activation depression (Study 1): parameters computed from the difference between the peak-to-peak values of the first and second responses (X_D and D_{MAX}) compared for the six muscles (BB, TB, FCR, ECR, FDI, and APB) and the three cathodes configurations (C6, C7, and T1). The sample sizes of the parameters X_D and D_{MAX} are n = 10. (B) Cathode configuration (Study 1): parameters obtained from the fits of the recruitment curves of the first responses (SL, PL, X_{50} and X_{TH}) compared for six muscles and three cathode configurations. The sample sizes of the parameters SL, PL, X_{50} and X_{TH} are n = 9. The mean values of each variable are indicated with blue triangles, green circles, and red diamonds for C6, C7, and T1, respectively. Shown are the corresponding standard error vertical bars. Significant differences between muscles are indicated with blue, green, and red horizontal bars representing C6, C7, and T1 cathode configurations, respectively. Significant differences between cathodes configurations are indicated with vertical black bars.

3.3.2. Anode electrode configurations (Study 2)

Suppression of the second responses compared to the first elicited using the cathode configurations and stimulus intensity that were chosen for each participant to be used in Study 2 (see section 3.2.3.2.) were confirmed using t-tests for each muscle (BB: $t(9)=4.8$, $p<.001$; TB: $t(9)=3.7$, $p=.005$; FCR: $t(9)=3.9$, $p=.004$; ECR: $t(9)=3.6$, $p=.005$; FDI: $t(9)=3.4$, $p=.008$; APB: $t(9)=2.8$, $p=.019$).

Averaged first and second evoked responses of a representative participant in Study 2 for different anode configurations (Neck, Shoulder, Iliac Crest, and Back) are shown in Figure 3.6. For this representative participant, the largest responses were recorded with the Neck anode in all muscles, except TB, while the smallest responses were recorded with the Back anode.

Results obtained from the comparison of the peak-to-peak amplitude of the second response compared to the first (post-activation depression) with three anode configurations (Neck, Shoulder, Iliac Crest, and Back) elicited with the stimulation intensity chosen by the experimenter for each muscle are summarized in Figure 3.7, while Table 3.3 summarizes the main statistical results. For FCR, the two-way ANOVA showed no significant interactions and statistically significant main effects for anode, but not for post-activation depression comparisons. For BB, TB, ECR, FDI and APB, since interactions were shown, follow-up analyses with one-way ANOVA or t-tests indicate statistically significant post-activation depression mostly for the Neck anode configuration; moreover, anode comparisons showed that the first and second responses were different for most muscles. In Figure 3.7, post-hoc multiple comparisons further indicated mostly differences between the Neck first and second responses elicited with those of the Iliac Crest and Back anode configuration in all muscles except for FDI (NOTE: despite statistical significance between anode factor in the one-way ANOVA for first responses from FDI and second responses from BB, post-hoc analyses with

Bonferroni correction did not show significant differences; significant effects for post-activation factor at APB obtained for the Shoulder and Back anode configurations were not confirmed using non-parametric tests).

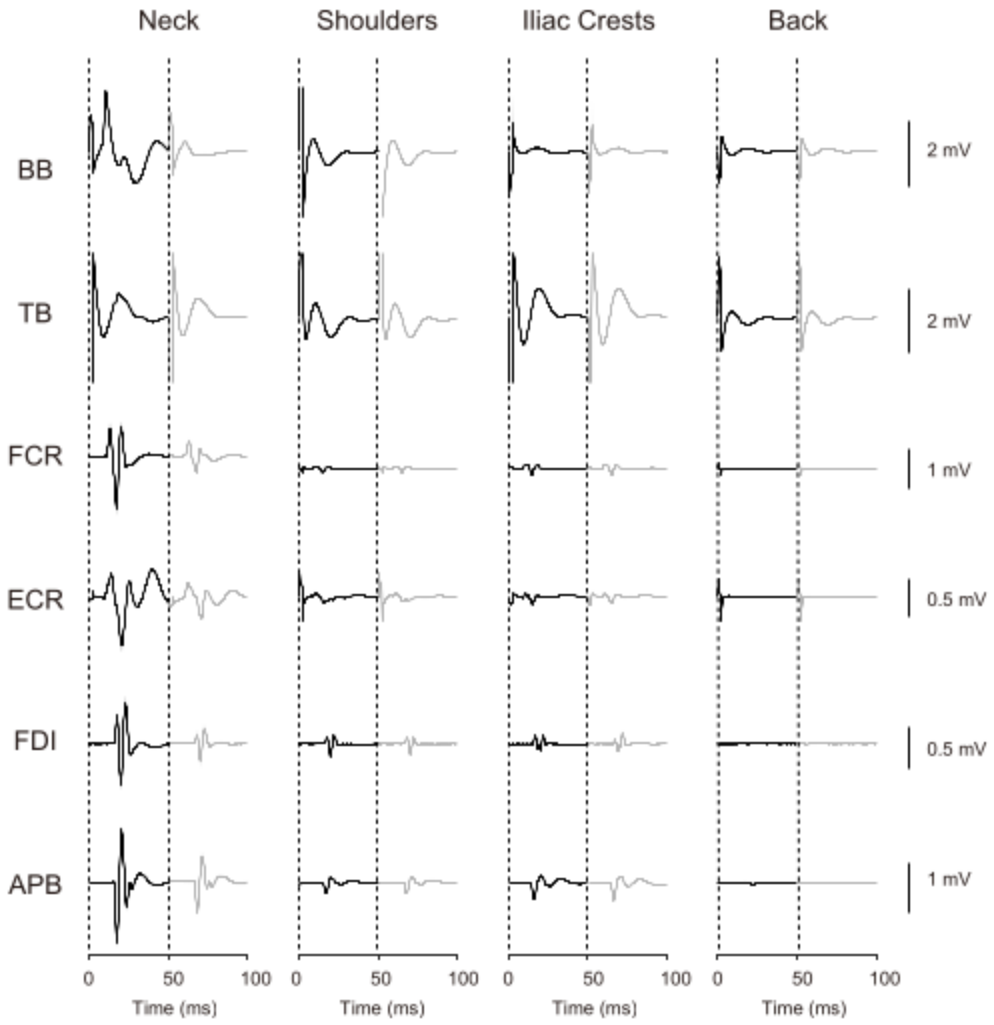

Figure 3.6 – Representative cervical tSCS evoked responses using different anode configurations: Representative participant averaged responses evoked in the six muscles (BB, TB, FCR, ECR, FDI and APB) using cervical tSCS with four anode configurations (Neck, Shoulders, Iliac Crests and Back). Three responses elicited with stimulations delivered as two monophasic pulses (50 ms inter-stimuli interval) were averaged for each anode configuration with the cathode location and stimulation amplitude chosen specifically for each participant. Representative averaged responses were obtained with the cathode placed over T1 and stimulation intensity at 60 mA. From left to right are the responses elicited with the anode placed the Neck, Shoulders, Iliac Crests, and Back, and from top to bottom are the averaged responses elicited for each muscle. Each trace corresponds to the averaged EMG time series, where the black trace indicates the response elicited by the first stimulus, and the gray trace by the second. The shaded areas in the corresponding colors indicate the standard deviation of the three responses. The dotted lines indicate the instant at which the first and second stimuli were delivered.

Table 3.3: Statistical analyses results showing within subject two-way ANOVA interactions and main effect results for post-activation depression (first and second responses) and anode configurations (Neck, Shoulders, Iliac Crests, and Back) comparisons of the responses evoked in each muscle (BB, TB, FCR, ECR, FDI, and APB) separately. When interaction was significant, the factors were compared separately with within subject one-way ANOVA or a t-test. Greenhouse-Geisser correction was used when the sphericity assumption was violated. The p values in bold indicate significant differences for a significance level of $\alpha = .05$.

	interaction	**post-activation depression**				**anode**	
		Neck	**Shoulders**	**Iliac Crest**	**Back**	**First**	**Second**
BB	**F (1,9.4)=16.2** ***p*=.003**	**t (9)=4.2** ***p*=.002**	t (9)=1.6 *p*=.132	t (9)=1.7 *p*=.121	t (9)=0.9 *p*=.400	**F (1.4,12.5)=11.4** ***p*=.003**	**F (1.7,15.0)=4.1** ***p*=.044**
TB	**F (3,27)=10.4** ***p*<.001**	**t (9)=3.4** ***p*=.007**	t (9)=-0.6 *p*=.561	t (9)=0.3 *p*=.781	**t (9)=-3.2** ***p*=.012**	**F (3,27)=6.1** ***p*=.003**	**F (3,27)=4.2** ***p*=.014**
FCR	F (1.2,10.8)=3.4 *p*=.087	F (1,9)=4.3 *p*=.067				**F (3,27)=4.5** ***p*<.001**	
ECR	**F (1,9.2)=9.2** ***p*=.013**	**t (9)=2.8** ***p*=.022**	t (9)=1.7 *p*=.131	t (9)=1.3 *p*=.219	**t (9)=1.1** ***p*=.296**	**F (1,9.2)=12.1** ***p*=.007**	**F (1,9.2)=9.3** ***p*=.013**
FDI	**F (1.1,10.1)=13.2** ***p*=.004**	**t (9)=3.8** ***p*=.004**	t (9)=1.2 *p*=.260	t (9)=1.5 *p*=.171	t (9)=0.5 *p*=.620	**F (1.1,9.5)=7.9** ***p*=.019**	F (1.1,9.8)=3.7 *p*=.083
APB	**F (1.1,10.3)=7.5** ***p*=.018**	**t (9)=3.2** ***p*=.010**	**t (9)=2.3** ***p*=.048**	t (9)=1.5 *p*=.160	**t (9)=2.3** ***p*=.048**	**F (1.2,10.6)=9.7** ***p*=.008**	**F (1.1,10.3)=5.0** ***p*=.045**

The NRS self-reported discomfort scores across participant for different anode configurations were Neck: 3.5±1.6, Shoulders: 3.5±1.5, Iliac Crests: 3.2±1.5, Back: 3.7±1.9 (mean±SD). Note that all participants reported a discomfort score of zero at the start of the study. Friedman's test showed no significant differences in the scores for different anode configurations ($\chi^2(3, 10) = 1.8$, $p = .606$).

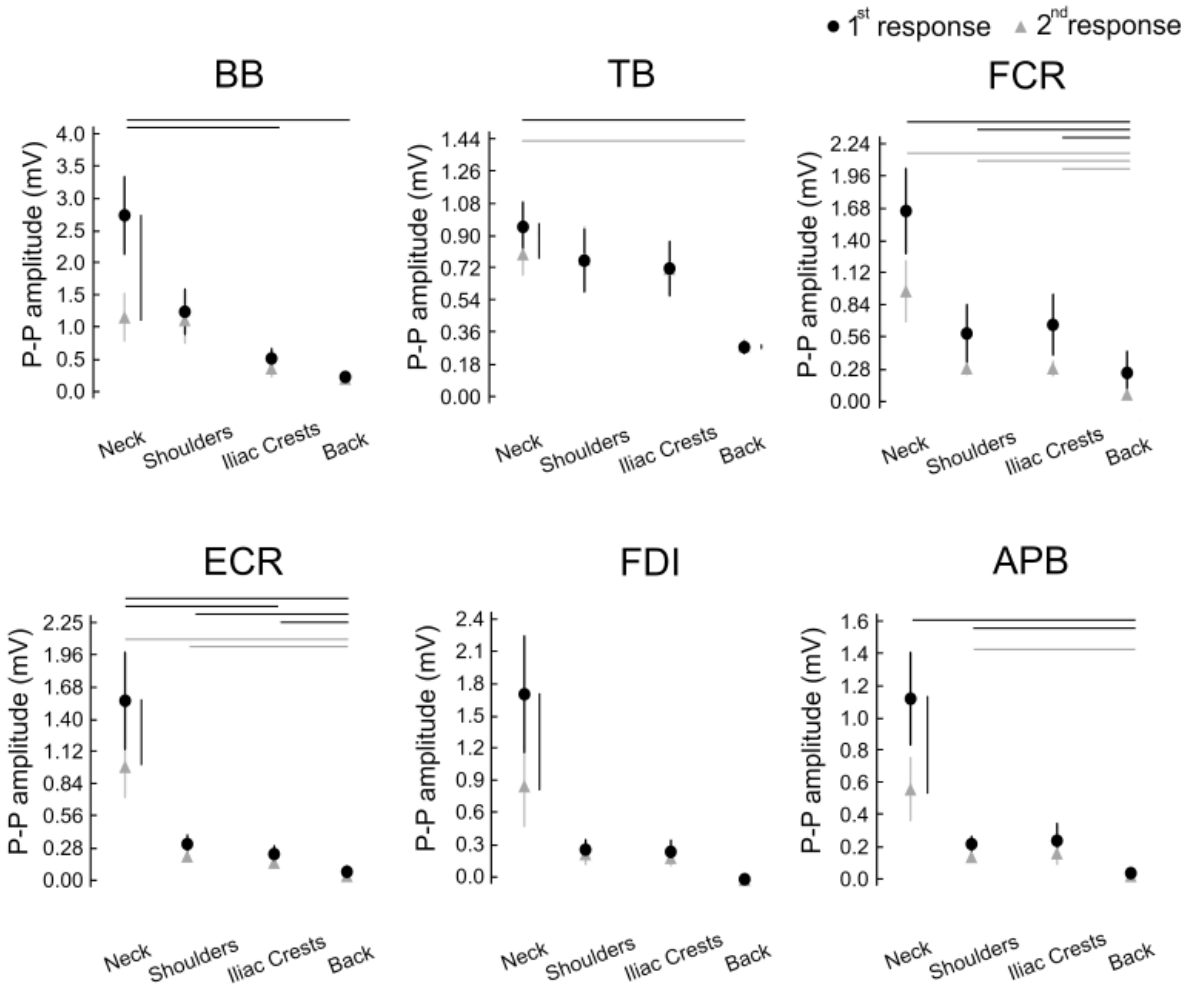

Figure 3.7 – Comparisons between different anode configurations: Anodes configurations (Study 2): the first and the second responses elicited with four anodes configurations (Neck, Shoulders, Iliac Crests and Back) were compared individually for each muscle. The mean of the first and second responses are indicated with black circles and gray triangles, respectively. Shown are the corresponding standard error vertical bars. The sample size of each data sets is n = 10. Significant differences between anode configurations are indicated with black and gray bars for the first and second responses, respectively. Significant differences between the first and second responses are indicated with vertical black bars.

3.4. Discussions

In this study, we showed post-activation depression in multiple muscles with all three cathode configurations (C6, C7, and T1). Moreover, we demonstrated that distal (FDI and APB) and proximal (BB, TB, FCR and ECR) upper-limb muscles had different activation excitability elicited by tSCS with different cathode configurations. Specifically, distal hand muscles were preferentially activated with the cathode configured over the T1 vertebra

compared to C6 and C7 configurations, while there was no selectivity for proximal arm muscles. Activation of distal hand muscles also required higher stimulation intensities compared to proximal arm muscles. Furthermore, larger responses were elicited with the Neck anode than other anode configurations (Iliac Crests, Shoulders and Back), while the levels of discomfort were similar. Although post-activation depression in the elicited responses was achieved with anode configurations in multiple muscles, the Neck configuration may elicit transsynaptic and direct motor activation during cervical tSCS with less current amplitude.

3.4.1. Post-activation depression in the spinally evoked motor responses during cervical tSCS

Transcutaneous spinal cord stimulation can elicit motor responses in muscles through activation of motoneurons via monosynaptic and oligosynaptic pathways with sensory fibers or interneurons and/or through direct excitation of motor axons in the ventral roots of the spinal cord (Minassian et al., 2007; Courtine et al., 2007; Hofstoetter et al., 2018). Primarily, the contribution of monosynaptic Ia excitation to the recruitment of α-motoneurons has been suggested when assessed using paired stimuli by examining the magnitude of suppression of the conditioned (second) evoked response in relation to the unconditioned (first) response (Minassian et al., 2007; Hofstoetter et al., 2014, 2018; Milosevic et al., 2019b). In the current study, paired stimuli delivered with 50 ms inter-stimuli interval and the anode configured over the anterior neck (Study 1) produced post-activation depression in all muscles regardless of the cathode configuration (C6, C7, and T1), as previously described (Minassian et al., 2007; Hofstoetter et al., 2014; Milosevic et al., 2019b). Although not statistically significant, suppression of the second responses was also possible when anode configurations other than the anterior neck (Shoulders, Iliac Crests, and Back) were employed with equivalent

stimulation intensities (Study 2; c.f. Figure 3.7). These results confirm the predominant reflex origins of the spinally evoked motor responses at multiple cervical spinal segments using various electrode configurations, which suggests that monosynaptic pathways were activated (Minassian et al., 2007; Hofstoetter et al., 2014; Milosevic et al., 2019b). Overall, regardless of the cathode configuration (C6, C7, or T1), post-activation depression in multiple upper-limb muscles may be elicited.

The stimulation intensity (X_D) which yielded the maximal post-activation depression was not different between the muscles and cathode configurations examined in this study (c.f., X_D in Figure 3.5A). This suggests that maximal post-activation depression can be elicited simultaneously in multiple upper-limb muscles using the same stimulus intensity (c.f., Figure 3.5A), as previously suggested (Milosevic et al., 2019a,b). Nonetheless, our results also showed that maximal post-activation depression amount (D_{MAX}) was significantly greater in the elbow extensors (TB) compared to elbow flexors (BB) (c.f., D_{MAX} in Figure 3.5A). Since the amount of reciprocal inhibition between BB and TB to their motor pools were shown to be similar (Katz, Penicaud & Rossi, 1991), heteronymous projections from other joint muscles (i.e. trans-joint projections) may have contributed to greater inhibition of the TB motor pool. In fact, the strength of projections of Ia fibers from wrist extensor (ECR) and flexor (FCR) muscles onto triceps (TB) motoneurons, may have yielded more inhibitory contributions to the recruitment of elbow extensors (Cavallari & Katz, 1989). While it is possible that that trans-joint projections may interfere in the transsynaptic activation of upper limbs during cervical tSCS, further studies are warranted to confirm this.

Unlike the observed post-activation depression in the lower-limb muscles (Minassian et al., 2007; Sayenko et al., 2015b; Milosevic et al., 2019a), our results demonstrated lack of complete abolishment of the second response even at the maximal suppression point (i.e., Figure 3.4, which shows post-activation depression at X_D), consistent to Milosevic et al. (Milosevic et al.,

2019b) and Wu et al. (Wu et al., 2020). It is possible that upper-limb responses during cervical tSCS were not fully supressed due to antidromic activation of motoneurons, which may reduce the post-activation depression by cancelling synaptic inputs (Milosevic et al., 2019b). Although unconfirmed, this may also be attributed to shorter post-stimulus recovery times of upper-limb responses compared to the lower-limbs, as suggested by Rossi-Durand et al. (Rossi-Durand et al., 1999) for explaining the FCR and Soleus H-reflexes responses using paired stimuli. Future investigations should therefore examine different inter-stimulus intervals on the post-activation depression of the upper-limb muscles using cervical tSCS.

3.4.2. Selectivity and excitability of transsynaptic activation across different cervical vertebral levels using tSCS

The selectivity of activation of upper-limb muscles with different cathode locations (C6, C7, and T1) was analyzed through the parameters obtained from the recruitment curves which estimate excitability attributes of muscle activations using cervical tSCS. Specifically, the stimulus intensity threshold (X_{TH}) and the maximum slope (*SL*) can be interpreted as excitability factors for the initial recruitment of motoneurons and the increase of the recruitment with increased stimulation current amplitude, respectively. Moreover, the stimulus intensity at 50% of the plateau (X_{50}) can be interpreted as comparative index between X_{TH} and *SL* (Devanne, Lavoie & Capaday, 1997; Capaday, 1997; Smith, Rymer & Knikou, 2015). Our results showed differences between distal hand muscles (FDI and APB) and proximal arm muscles (BB, TB, FCR, and ECR) for X_{TH}, suggesting more excitability to the initial recruitment of motoneurons projecting to proximal arm muscles for all cathodes configurations (c.f., smaller X_{TH} in Figure 3.5B). Moreover, selectivity to the recruitment of the motoneurons projecting to hand muscles is indicated by the greater values of the *SL* parameter for T1 cathode

configuration compared to C6 and C7 (c.f. *SL* in Figure 3.5B). Although not statistically significant, this selectivity is further supported by a decrease of the values of X_{TH} and X_{50} in hand muscles (c.f., differences between proximal and distal muscles for X_{TH} and X_{50} in Figure 3.5B). Finally, the recruitment curve plateau (*PL*), which can be interpreted as an index of motor activation, was greater with the cathode electrode configured over T1 compared to C6 in distal hand muscles (c.f., *PL* in Figure 3.5B). These findings suggest selectivity of motor pool recruitment of distal muscles with different cathode configurations, which agrees with our hypothesis since distal muscles were preferentially activated with the T1 (caudal) cathode electrode placement compared to C6 (rostral) vertebral level placement. The three cathode configurations used in this study were chosen based on the more caudal organization of dorsal roots and motor pools projecting distal compared to proximal muscles of human upper-limb (Kendall et al., 2005; Cadotte et al., 2015). Likewise, it is plausible that electrode configurations other than those examined herein (e.g., different sizes and locations) would be selective to the activation of upper-limb motor pools. Nonetheless, despite the larger cathode electrodes (5 x 5 cm) used in the present study compared to previous studies, e.g., 2.5 cm round electrodes used by Gad et al. (Gad et al., 2018) and Inanici et al. (Inanici et al., 2018), we showed preferential activation of distal hand muscles (FDI and APB) with the T1 cathode configuration. Possibly, configuration of the cathodes more rostrally (e.g., over the C4 vertebra) could preferentially activate proximal upper-limb muscles. Future studies are therefore warranted to test different cathode sizes and more rostral cathode configurations on the responses in upper-limbs using cervical tSCS.

Facilitatory heteronymous projections of the Ia-afferents from distal-to-proximal upper-limb muscles motor pools (Cavallari & Katz, 1989; Marchand-Pauvert, Nicolas & Pierrot-Deseilligny, 2000), which are absent from proximal-to-distal muscles in humans (Cavallari, Katz & Penicaud, 1992; Pierrot-Deseilligny & Burke, 2005), may also have contributed to the

differences in the activation excitability observed in proximal and distal muscles (X_{TH}). In other words, while the activation of Ia-afferents from distal muscles may contribute to the recruitment of motoneurons of proximal muscles, a mutual relation may not exist from proximal-to-distal muscles in the upper-limbs. In addition, different distributions of motoneuron sizes in hand and arm muscles (Enoka & Fuglevand, 2001; Enoka, 2015) might have preferentially activated proximal arm muscles through either direct excitation of motor nerves (Rattay, 1999), and/or excitation of Ia-monosynaptic pathways (Buller, Garnett & Stephens, 1980; Pierrot-Deseilligny & Burke, 2005). Other oligosynaptic pathways connecting group Ib, group II, and cutaneous afferents may also add significant contributions to the motor responses (Gerasimenko et al., 2015a). Taken together, different selectivity and excitability factors of recruitment during cervical tSCS may have contributed to preferential activation of distal hand muscles for the T1 cathode configuration, while this was not true for proximal muscles.

The results obtained in the present study inform methodological considerations for placement of the cathode electrode during cervical tSCS to assess spinally evoked motor potentials and/or for rehabilitation protocols using continuous stimulation. For instance, tSCS delivered with the cathode placed over the C6 vertebra (or possibly more rostrally as Gad et al. (Gad et al., 2018) and Inanici et al. (Inanici et al., 2018)) may be effective to transsynaptically recruit proximal arm muscles, while caudal placement over the T1 vertebrae may be effective for activating distal hand muscles (c.f., Figure 3.3). Similarly, stimulation paradigms involving both rostral and caudal cathode electrodes (Inanici et al., 2018; Gad et al., 2018; Benavides et al., 2020) may produce selective activation of cervical spinal networks with tSCS during specific movement tasks. Such preferential activation of arm muscles motor pools may help strength descending commands across spinal lesioned sites during voluntary arm contractions,

thus potentially enhancing neuroplasticity effects during rehabilitation (Park et al., 2008; Formento et al., 2018; Murray & Knikou, 2019; Courtine & Sofroniew, 2019).

3.4.3. Anode configurations may optimize transsynaptic activation of the spinally evoked responses during cervical tSCS

The stimulating parameters for comparing anode configurations were chosen to be on the ascending part of the recruitment curve and to yield post-activation depression in the second responses when the anode was placed on the anterior side of the neck. Therefore, responses elicited with other anode configurations (Shoulders, Iliac Crests, and Back) were compared relative to the Neck configuration. As summarized in Figure 3.7, our results indicate that elicited responses were largest when the anode was placed over the anterior neck as well as that post-activation depression was less prevalent when the anodes were not on the anterior neck. Although the proximity between the anode and cathode electrodes and the geometry comprising the cervical body were similar between Shoulders and Neck configuration, our results indicate greater transsynaptic activation with the Neck configuration compared to the Shoulders. The larger responses yielded with the Neck configuration may not only be due to the proximity between the cathode and anode electrodes, but also a better convergence of the electrical current across the dorsal roots. However, transsynaptic motor activation with other anodes configurations can not be ruled out and may be elicited using higher stimulation intensities.

3.4.4. Discomfort during tSCS

In our study, the pain experienced during tSCS was not different between the four anode configurations. Participants typically reported discomfort scores between 3 and 5,

corresponding to moderate levels of pain (Hawker et al., 2011). Discomforts included skin prickling under the stimulating electrodes and, less commonly, contraction of the neck muscles. It is therefore expected that configuration of the anode electrode over the neck can yield larger spinally evoked responses in the upper-limb muscles (Figure 3.7) with similar discomfort levels. Taken together, our results suggest that anterior neck electrode configuration may, at least within the chosen parameters of our study, be more effective in eliciting transsynaptic activation of upper-limb muscles. However, these findings only extent to applications using single and double pulses (i.e., electrophysiological testing), and further testing is required to compare discomfort levels during rehabilitation applications using continuous stimulation.

There were no serious adverse events experienced during the experiments, consistent with previous reports examining cervical tSCS (Sabbahi & Sengul, 2012; Wu et al., 2020). However, it should also be noted that only monophasic double pulses were used with current amplitudes up to 100 mA in the current study.

3.4.5. Limitations

The maximal current intensity was not reached in two participants due to the discomfort experienced, which may have limited the data available for estimating the recruitment curves. While we used relatively large cathodes (5 x 5 cm) that might have helped alleviate some of the pain felt during stimulation (Verhoeven & VANDIJK, 2006; Roy, Bosgra & Stein, 2014), the size of these electrodes could have caused less selectivity for targeting specific upper-limb motor pools (Figure 3.5B). Despite these limitations, our study showed that it was possible to preferentially activate distal hand muscle with the cathode configured over the T1 level compared to C6 and C7 cathode configurations. Another limitation of the study is the relatively small sample size, despite being comparable to previous studies with able-bodied participants

(Minassian et al., 2007; Courtine et al., 2007; Krenn et al., 2013; Sayenko et al., 2015a; Danner et al., 2016; Milosevic et al., 2019b). It should also be noted that responses were only recorded unilaterally from the right upper-limb muscles of right-handed participants. It is possible that hand dominance may have influenced the motor responses (Sathiamoorthy & Sathiamoorthy, 1990; Pereira et al., 2012; Gordon et al., 2012), and thus our results should be carefully considered and generalized. Finally, despite similar signal-to-noise ratios across muscles in our current study, possible cofounding factors related to comparisons between muscles should further be investigated using non-linear regression models in future studies.

3.5. Conclusions

The results obtained in this study showed that transsynaptic activation of motor pools projecting to the upper limb muscles is achievable using all three cathode configurations (C6, C7, and T1). Distal hand muscles (FDI and APB) were preferentially activated with the cathode configured over the T1 vertebra compared to C6 and C7, while there was no selectivity for proximal arm muscles (BB, TB, FCR and ECR). We showed higher stimulation thresholds for activation of distal hand muscles compared to proximal arm muscles. The elicited responses were largest when the anode was placed over the anterior neck, compared to other configurations (shoulders, iliac crests, and back) with equivalent stimulation intensities. Our results therefore provide methodological considerations for electrode configuration that can help elicit transsynaptic motor activation during cervical tSCS with less current amplitude. The utility of these results concerns the use of tSCS for assessing the state of spinal cord neural circuitries through single and double pulses, while further testing is warranted to confirm these findings during continuous stimulation.

CHAPTER IV

Optimizing sensory fiber activation during cervical transcutaneous spinal stimulation using different electrode configurations: A computational analysis

The material presented in this chapter has been published in the article:

de Freitas, R. M., Capogrosso, M., Nomura, T., & Milosevic, M. 2022. Optimizing sensory fiber activation during cervical transcutaneous spinal cord stimulation using different electrode configurations: A computational analysis. *Artificial Organs*. 00:1-12. DOI: 10.1111/aor.14323.

***NOTE**: The content of this chapter is identical to the material presented in the publication.*

CHAPTER IV

Abstract

Cervical transcutaneous spinal cord stimulation (tSCS) is a rehabilitation tool which has been used to promote upper-limb motor recovery after spinal cord injury. Importantly, optimizing sensory fiber activation at specific spinal segments could enable activity-dependent neuromodulation during rehabilitation. An anatomically realistic cervical tSCS computational model was used to analyze the activation of α-motor and Aα-sensory fibers at C7 and C8 spinal segments using nine cathode electrode configurations. Specifically, the cathode was simulated at three vertebral level positions: C6, C7, and T1; and in three sizes: 5.0 x 5.0, 3.5 x 3.5; and 2.5 x 2.5 cm^2, while the anode was on the anterior neck. Finite element method was used to estimate the electric potential distribution along α-motor and Aα-sensory fibers, and computational models were applied to simulate the fiber membrane dynamics during tSCS. The minimum stimulation intensity necessary to activate the fibers (activation threshold) was estimated and compared across cathode configurations in an effort to optimize sensory fiber activation. Our results showed that nerve fibers at both C7 and C8 spinal segments were recruited at lower stimulation intensities when the cathode was positioned over the C7 or T1 vertebra compared with the C6 position. Sensory fibers were activated at lower stimulation intensities using smaller electrodes, which could also affect the degree of nerve fiber activation across different positions. Importantly, Aα-sensory fibers were consistently recruited before α-motor fibers. These results imply that cathode positioning could help optimize preferential activation of hand muscles during cervical tSCS.

Keywords: cervical; transcutaneous spinal cord stimulation; upper-limb; computational simulation; finite element method.

CHAPTER IV

4.1. Introduction

Recent clinical studies have demonstrated the efficacy of cervical transcutaneous spinal cord stimulation (tSCS) for recovery of upper-limb motor function after spinal cord injury (Gad et al., 2018; Benavides et al., 2020; Inanici et al., 2021). Spatiotemporal synchronization between motor intentions (i.e., descending commands) and sensory fiber activations during tSCS can strengthen the neural connections across the lesioned spinal regions and promote neural changes towards motor recovery (Formento et al., 2018; Rowald et al., 2022). The recruitment of sensory fibers is thus critical for activating the spinal circuits, which can compensate for scare sensory feedback in spinal cord injured individuals and transsynaptically amplify the motor outputs during the intended tasks (Formento et al., 2018; Milosevic et al., 2019b; Rowald et al., 2022). In addition, activation of neural circuits at specific spinal segments is thought to be important in rehabilitation to active specific movement synergies (Greiner et al., 2021; Rowald et al., 2022; Barra et al., 2022). Therefore, optimizing the electrode placement and size for cervical tSCS delivery may improve activity-dependent spinal neuromodulation methods for upper-limb rehabilitation.

Spatiotemporal activation of sensory afferent fibers was recently demonstrated in experimental and computational studies during cervical tSCS (Milosevic et al., 2019b; Wu et al., 2020; Zheng & Hu, 2020b; de Freitas et al., 2021, 2022a; Sasaki et al., 2021). Specifically, it was suggested that proprioceptive sensory fibers were preferentially recruited at lower stimulation intensities compared with motor fibers (Milosevic et al., 2019b; Wu et al., 2020; de Freitas et al., 2021, 2022a; Sasaki et al., 2021). Moreover, activation of nerve fibers at specific spinal segments using different cervical tSCS electrode configurations could be inferred from Zheng et al. (Zheng & Hu, 2020b), which showed that independent and synergistic upper-limbs joint movements were enabled during continuous cervical tSCS. Supporting evidence for activation of fibers at specific spinal segments was recently also

demonstrated in an experimental study by de Freitas and colleagues who compared activation of hand muscles using different cathode electrode configurations (de Freitas et al., 2021). It may also be possible that such selective spinal activation is improved by using smaller tSCS cathode electrode sizes. Therefore, a better understanding of how different cathode configurations activate nerve fibers at specific spinal segments may optimize spatiotemporal activation of sensory fibers during cervical tSCS.

Computational simulations have been developed in the recent years for better understanding nerve fiber recruitment during spinal stimulation (Ladenbauer et al., 2010; Danner et al., 2011; Capogrosso & Lempka, 2020; de Freitas et al., 2022a). Specifically, these simulations combine finite element method (FEM) and mathematical models to simulate the fiber membrane dynamics (McIntyre, Richardson & Grill, 2002; Ladenbauer et al., 2010; Danner et al., 2011; Rattay et al., 2014; Gaines et al., 2018; Greiner et al., 2021). Previous spinal stimulation studies have used this methodological approach to quantify the activation efficiency of different electrode configurations (Ladenbauer et al., 2010; Greiner et al., 2021; Rowald et al., 2022). However, such computational simulations have not yet been applied to cervical tSCS, although they could provide useful information about the electrode configurations which optimize sensory fiber activation at different spinal segments. Realistic anatomical considerations of the cervical body should also be included in computational models to improve the translation of results from modelling studies.

We developed a cervical tSCS computational model to analyze activation of nerve fibers at two spinal segments (i.e., C7 and C8 spinal nerves) by comparing different cathode electrode configurations. We estimated the minimum stimulation intensities necessary to recruit α-motor and Aα-sensory fibers (i.e., activation thresholds) at C7 and C8 spinal segments using different cathode configurations. In total, nine different cathode configurations were simulated, including placement on three vertebral level positions: C6, C7, or T1, and three

electrode sizes: 5.0 x 5.0 (L) (Milosevic et al., 2019b; de Freitas et al., 2021; Sasaki et al., 2021), 3.5 x 3.5 (M), or 2.5 x 2.5 (S) cm^2, while the anode electrode remained configured on the anterior neck. Specifically, we used the activation threshold as a dependent (measured) variable and the cathode configuration as an independent (manipulated) variable in an effort to optimize activation of sensory fibers. Considering their relative proximity, we hypothesized that both motor and sensory fibers at the C7 spinal segment would be recruited at lower stimulation intensities for the cathode positioned over the C6 vertebrae compared with the other cathode configurations. Analogously, we also hypothesized that nerve fibers at the C8 spinal segment would be recruited at lower stimulation intensities when the cathode is positioned over the T1 vertebrae due to their proximity. In other words, activation of sensory fibers at specific spinal segments would be optimized by configuring the cathode in closer proximity to the targeted fibers. Moreover, we also hypothesized that using smaller electrodes would affect how C7 and C8 spinal nerves are activated when the cathode is configured at different positions. Finally, we expected that sensory fibers would have lower activation thresholds compared with motor fibers for both C7 and C8 spinal segments, consistent with previous computational simulations (de Freitas et al., 2022a) and experimental implications (Milosevic et al., 2019b; Wu et al., 2020; de Freitas et al., 2021; Sasaki et al., 2021).

4.2. Methods

4.2.1. Extraneural electric potential estimation

A 3D model of the cervical body and stimulation electrodes was developed using Autodesk Inventor Professional 2021 (Autodesk Inc., USA). The geometrical structures of the cervical body were designed based on the MRI reconstructed volume of a 34 year old male (Christ et al., 2010), and from human anatomical proportions (Lee & Hwang, 2002; West et

al., 2012; Torriani et al., 2014; Sass et al., 2017, 2020; Calabrese et al., 2018; Wade et al., 2020; Mendez et al., 2021). Illustrations of the 3D geometry are shown in Figure 4.1, and all its tissue components, as well as their respective electrical conductivities, are listed in Table 4.1. The cathode electrode was centered at C6, C7, or T1 spinous process, reproducing the experimental conditions of (de Freitas et al., 2021). Moreover, the cathode electrode was square shaped with three different sizes: 5.0 x 5.0 (L), 3.5 x 3.5 (M), or 2.5 x 2.5 (S) cm^2. The L cathode size is the same as the one used by previous cervical tSCS experimental studies (Milosevic et al., 2019b; de Freitas et al., 2021; Sasaki et al., 2021), whereas the other cathode sizes were designed to approximately correspond to half (M: 3.5 x 3.5 cm^2 = 12.25 cm^2) (Benavides et al., 2020; Islam et al., 2020) and one forth (S: 2.5 x 2.5 cm^2 = 6.25 cm^2) (Benavides et al., 2020) of the L cathode size area (25 cm^2) (Milosevic et al., 2019b; de Freitas et al., 2021; Sasaki et al., 2021). In total, nine cathode electrode configurations were developed (3 positions x 3 sizes = 9 cathode configurations). An anode electrode (7.5x10 cm^2) was placed on the anterior side of the neck (Milosevic et al., 2019b; Wu et al., 2020; de Freitas et al., 2021; Sasaki et al., 2021). Illustrations of the nine different cathode electrode configurations used in our simulations are shown in Figure 4.2.

CHAPTER IV

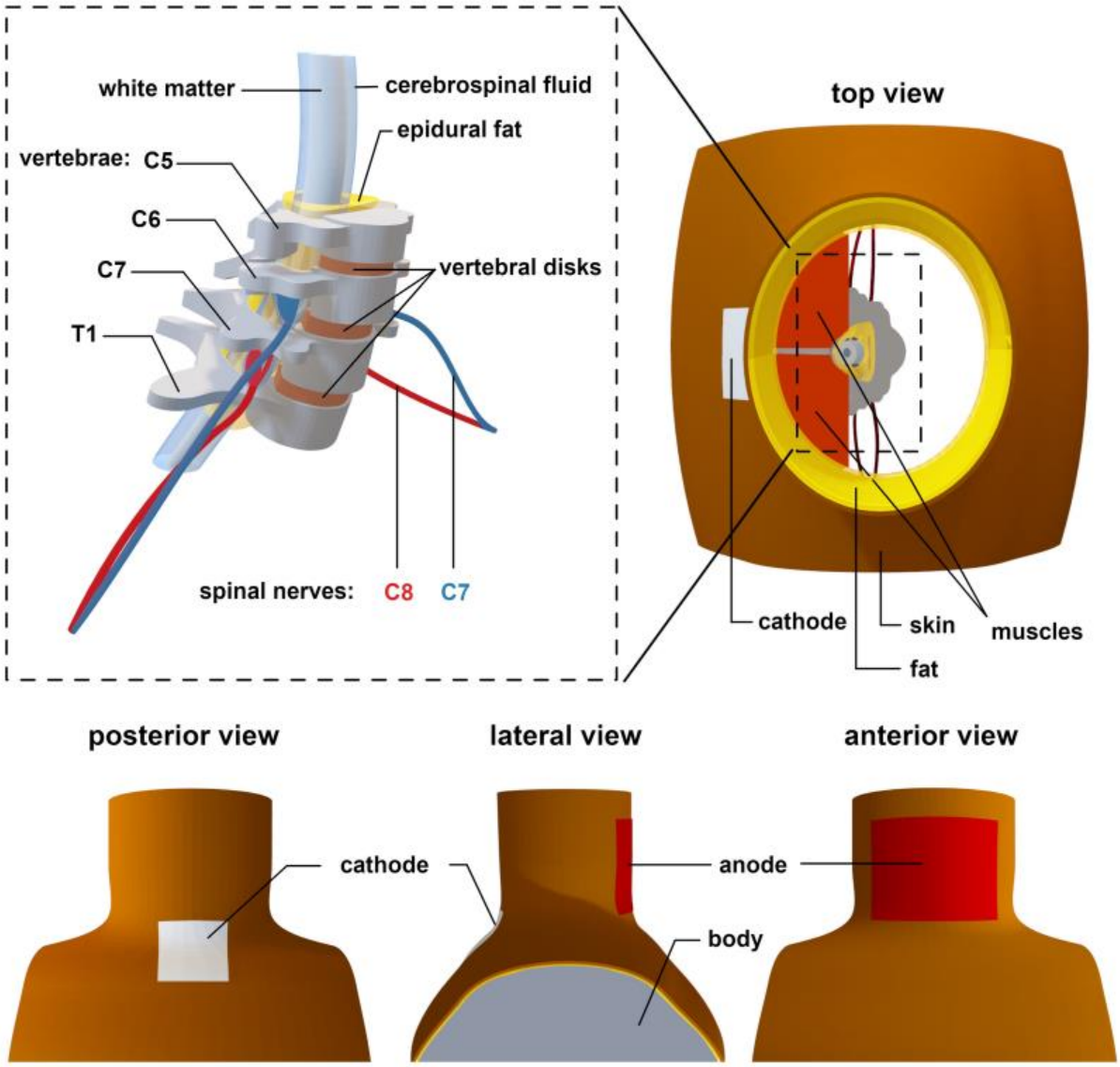

Figure 4.1 – 3D model of the cervical spinal cord including C7 and C8 spinal nerves: Illustrations of the cervical body 3D model and transcutaneous spinal cord stimulation electrodes used in the simulations. At the top left, structures surrounding the spinal canal are shown: white matter; cerebrospinal fluid; epidural fat; C5, C6, C7, and T1 vertebra; C5-C6, C6-C7, and C7-T1 vertebral disks; and C8 and C7 spinal nerves. At the top right, the top view of the 3D model shows the back muscles, skin and fat structures. The body structure is not visible. At the bottom, the posterior, lateral and anterior views of the model are shown.

The 3D model was imported in COMSOL Multiphysics (v.5.6, COMSOL Inc., USA) for meshing and FEM computations. The geometry was meshed with approximately 11 million tetrahedral elements. The conductivities of the tissue components and electrodes were assigned according to previous spinal cord stimulation computational studies (Ladenbauer et al., 2010; Danner et al., 2011; Khadka et al., 2020). Moreover, anisotropic electrical conductivities to

longitudinal and transversal directions were assigned to the white matter and back muscles using Curvilinear Coordinates toolbox available in COMSOL, consistent with the methodology used in (Greiner et al., 2021; de Freitas et al., 2022a). Specifically, the diffusion method was applied by defining the bottom surfaces of the structures to the inlet condition and their top surfaces to the outlet condition. The conductivities assigned to each component are presented in Table 4.1. Insulating boundary condition was applied to all external surfaces of the geometry, except for the largest outer surfaces of the electrodes (Khadka et al., 2020). For the cathode electrodes, $V(\boldsymbol{x}) = 0$ was adopted, where $V(\boldsymbol{x})$ is the electric potential at the **x** point of the domain. For the anode electrode, normal current density condition was applied such that 1 A current was injected (Khadka et al., 2020; Greiner et al., 2021). The Laplace equation ($(\nabla.(\sigma\nabla V)(\boldsymbol{x}) = 0$) was solved with the FEM in COMSOL to obtain the electric potentials across the 3D geometry. The materials were considered as purely resistive, while a quasi-stationary approximation was assumed for estimating the electric potentials (Bossetti, Birdno & Grill, 2008), consistent with previous tSCS simulation studies (Ladenbauer et al., 2010; Danner et al., 2011). This assumption enabled solving the governing electromagnetic equations of our system by neglecting capacitive and inductive effects of the body tissues, as well as wave propagation effects during the stimulation (Bossetti, Birdno & Grill, 2008).

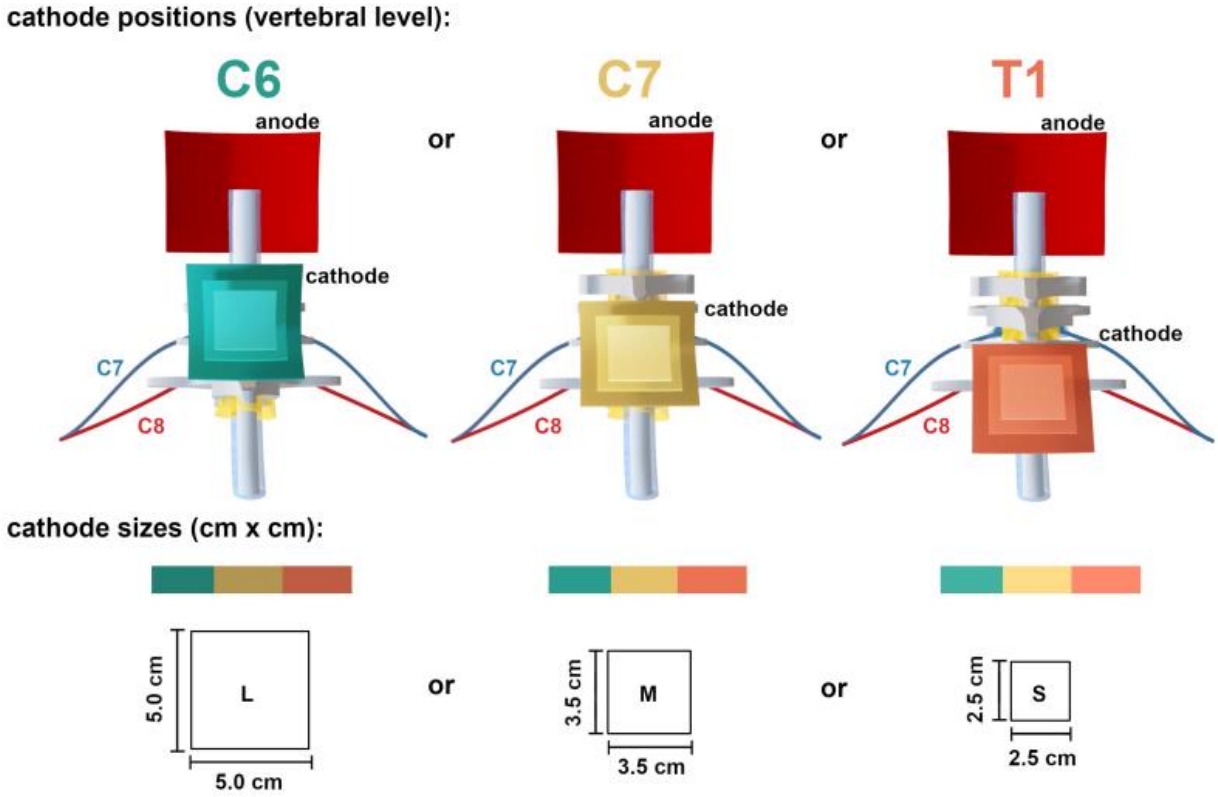

Figure 4.2 – Nine different cathode configurations simulated: Illustrations of the nine different cathode electrode configurations simulated, including three vertebral level positions and three sizes. The cathode sizes are 5.0 x 5.0 cm² (L) in dark shades, 3.5 x 3.5 cm² (M) in medium shades, and 2.5 x 2.5 cm² (S) in light shades. The cathode positions are C6 (blue), C7 (yellow), and T1 (orange) vertebral levels. The anode electrode (red) is remained on the anterior neck. The C7 and C8 spinal nerves are indicated in blue and red, respectively.

Table 4.1: Conductivity values, in siemens per meter, assigned to the components of the geometrical model of the cervical body and transcutaneous spinal cord stimulation electrodes. The components of the cervical body are the gray matter; white matter; ventral/dorsal roots and rootlets, dorsal root ganglia; C7 and C8 spinal nerves; cerebrospinal fluid; epidural fat; C5-C6, C6-C7 and C7-T1 intervertebral disks; C5, C6, C7 and T1 vertebra; back muscles; general cervical body; skin and fat. In total, the cathode electrode was developed in nine configurations, including three locations (C6, C7 and T1 vertebral levels) and three sizes (5.0 x 5.0, 3.5 x 3.5 and 2.5 x 2.5 cm^2). The anode electrode was positioned on the anterior neck. For white matter and muscles, anisotropic conductivities were assigned to longitudinal (L) and transversal (T) components.

Component	Conductivity σ (S/m)
Gray matter (Calabrese et al., 2018)	0.276
White matter (Calabrese et al., 2018)	L: 0.6; T: 0.083
C7 and C8 spinal nerves (Wade et al., 2020)	0.1432
Dorsal and ventral roots (Sass et al., 2017; Mendez et al., 2021)	0.1432
Dorsal and ventral rootlets (Sass et al., 2017; Mendez et al., 2021)	0.1432
Dorsal root ganglia (West et al., 2012)	0.1432
C5, C6, C7 and T1 vertebra (Christ et al., 2010)	0.02
C5-C6, C6-C7 and C7-T1 intervertebral disk (Christ et al., 2010)	0.6
Cerebrospinal fluid (Sass et al., 2020)	1.7
Epidural fat (Christ et al., 2010)	0.04
Back muscles (Christ et al., 2010)	L: 0.5; T: 0.08
Body (Christ et al., 2010)	0.25
Skin (Lee & Hwang, 2002)	0.0025
Fat (Torriani et al., 2014)	0.04
Cathode and anode electrodes (Milosevic et al., 2019b; Wu et al., 2020; Benavides et al., 2020; Islam et al., 2020; de Freitas et al., 2021; Sasaki et al., 2021)	0.01

Legend: L – longitudinal; T – transversal

Extraneural electric potential distributions along nerve fiber trajectories were obtained from the FEM computation outcomes and applied to dedicated nerve fiber models to simulate the activation of α-motor and Aα-sensory fibers (Gaines et al., 2018) (Figure 4.3). The trajectories of α-motor and Aα-sensory fibers were defined from the clavicle levels until the center of the gray matter structure (Figure 4.3A). Specifically, at the foramen level, three trajectory segments spanned the ventral and dorsal root structures until the white matter. At the interface of the rootlets with the white matter, three other segments were defined until the center of the gray matter, simulating the nerve fiber curvature entering the dorsal and ventral horns

(Greiner et al., 2021). In total, 18 trajectories were defined for the α-motor fibers and Aα-sensory fibers in the C7 and C8 spinal nerves (i.e., 3 segments at the rootlets level x 3 segments entering the white matter x 2 sides = 18 trajectories), as shown in Figure 4.3A. These trajectories were representative of the motor and sensory nerve fiber microanatomies within the ventral and dorsal root structures, respectively.

4.2.2. Simulation of α-motor and Aα-sensory fibers

The membrane potential dynamics of α-motor and Aα-sensory fibers were simulated with dedicated nerve fiber models developed by Gaines and colleagues (Gaines et al., 2018). The Gaines models (Gaines et al., 2018) consider specific channel gating parameters for motor and sensory fibers, which account for their physiological differences (Kiernan, Mogyoros & Burke, 1996). Notably, the Gaines models have been validated for transcutaneous peripheral nerve stimulation in able-bodied individuals (Gaines et al., 2018). The α-motor and Aα-sensory fibers were simulated using 14 and 16 μm diameters, respectively, since Aα-sensory fibers have larger diameters compared with α-motor fibers (Kandel et al., 2013). This range of fiber sizes is consistent with that used in previous simulation studies (Danner et al., 2011; Gaines et al., 2018; de Freitas et al., 2022a). The motor and sensory axon fiber models (available for download in https://modeldb.yale.edu/243841) were implemented in Python 3.9 using NEURON 8.0 (Hines & Carnevale, 1997), with no changes to the original implementation.

To estimate the activation thresholds, we used a direct computation of the membrane equations of the Gaines models, consistent with previous simulation studies (Greiner et al., 2021; de Freitas et al., 2022a), instead of the second spatial derivative of the extraneural potentials along the fiber trajectories (Rattay et al., 2014). The minimum stimulation intensities necessary to activate the fibers, i.e. activation thresholds, were estimated by scaling the

extraneural distribution of electric potentials along the fiber trajectories applied to the Gaines axon fiber models (Grill, 1999; Richardson, McIntyre & Grill, 2000). Specifically, the distributions of electric potentials along the trajectories of motor and sensory fibers obtained from the FEM simulations (Figure 4.3A) were linearly scaled (i.e., multiplied by a constant factor) and applied as extraneural potentials to the compartments of the Gaines fiber models. Considering the linear relationship between the FEM-calculated electric potentials and the current injected at the anode electrode, the scaling factors used to adjust the extraneural potential distributions were a fraction of the 1 A stimulation current initially applied (Khadka et al., 2020; Greiner et al., 2021; de Freitas et al., 2022a). A bisection algorithm was used to adjust the scaling factor and estimate the minimum stimulation intensities to the fiber activation (Danner et al., 2011; Khadka et al., 2020), i.e. the activation thresholds. The stimulation was simulated as rectangular monophasic pulse with 2 ms duration, in agreement with previous cervical tSCS experimental studies (Milosevic et al., 2019b; de Freitas et al., 2021; Sasaki et al., 2021). A single monophasic pulse was used in our simulations to enable a better understanding of neural targets during tSCS, consistent with previous experimental(Milosevic et al., 2019b; de Freitas et al., 2021) and simulation (Ladenbauer et al., 2010; Danner et al., 2011; Greiner et al., 2021) studies, and also to compare our simulation results with previous experimental data (Milosevic et al., 2019b; de Freitas et al., 2021; Sasaki et al., 2021). The rheobase and chronaxie of motor fibers are 1.21 nA and 0.12 ms, respectively, for an injected rectangular current pulse. Moreover, the rheobase and chronaxie of sensory fibers are 0.69 nA and 0.19 ms, respectively, confirming higher excitability of sensory compared with motor fibers (Kiernan, Mogyoros & Burke, 1996). The 18 representative trajectories defined for α-motor and Aα-sensory fibers at C7 and C8 spinal segments added microanatomical randomness to estimation of the activation thresholds, such that statistical tests could be used for comparisons.

4.2.3. Statistics

To compare the activation of nerve fibers at different spinal segments, the activation thresholds of α-motor and Aα-sensory at C7 and C8 spinal segments were compared across nine different cathode configurations, including three cathode positions (C6, C7, and T1 vertebral levels) and three cathode sizes (L, M, and S). The activation threshold was used as a dependent (measured) variable, whereas the cathode configuration was used as an independent (manipulated) variable in an effort to optimize activation of sensory fibers. For the α-motor and the Aα-sensory fibers separately, a mixed design two-way analysis of variance (ANOVA) test was used to compare nerve fibers at C7 and C8 spinal segments (between-subjects factor *spinal segment*: C7 and C8) using different cathode configurations (within-subjects factor *cathode configuration*: $C6_L$, $C6_M$, $C6_S$, $C7_L$, $C7_M$, $C7_S$, $T1_L$, $T1_M$, and $T1_S$). Moreover, a mixed design two-way ANOVA test was used to compare α-motor and Aα-sensory fibers pooled together from C7 and C8 spinal segments (between-subjects factor *fiber type*: *α-motor* and *Aα-sensory*) using the same cathode configurations (within-subjects factor *cathode configuration*: $C6_L$, $C6_M$, $C6_S$, $C7_L$, $C7_M$, $C7_S$, $T1_L$, $T1_M$, and $T1_S$). When significant interactions were found for the two-way ANOVA, a within- or between-subjects one-way ANOVA was performed for each factor separately. Post hoc multiple comparisons were performed with Bonferroni corrections when one-way ANOVA main results were significant. Greenhouse-Geisser corrections were used when the Mauchly's test results showed that the sphericity assumption was violated. Since normality of the data was not confirmed for all of analysis groups using the Shapiro-Wilk test, we confirmed all results with non-parametric Mann-Whitney, Friedman and Dunn-Bonferroni tests. All statistical tests were performed using SPSS (IBM, Armonk, NY) and the significance level was set to $\alpha=0.05$.

CHAPTER IV

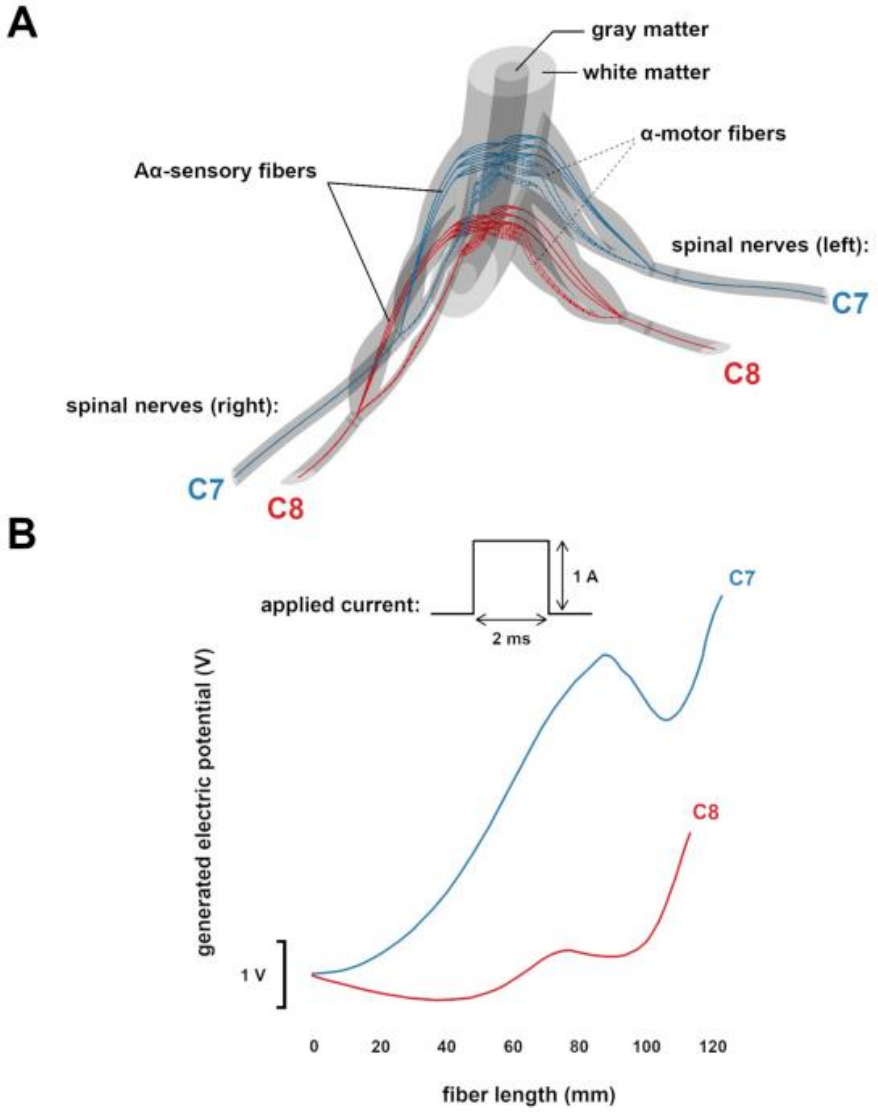

Figure 4.3 – Distribution of electric potential along nerve fibers at C7 and C8 spinal segments: (A) Trajectories of α-motor (dashed lines) and Aα-sensory (solid lines) fibers along the C7 (blue) and C8 (red) spinal nerves until the gray matter structure. In total, 18 trajectories are shown for each α-motor and Aα-sensory fiber at each spinal segment (i.e., C7 and C8 spinal nerves). (B) The electric potential distribution (V) along a Aα-sensory fiber at C7 (blue) and C8 (red) spinal segments estimated with a finite element method is shown. These distributions of electric potential were obtained when 1A was injected in the anode electrode, while a cathode with 2.5 x 2.5 cm² size was positioned at T1 vertebral level.

4.3. Results

Comparisons between spinal segments

Comparison results between α-motor and Aα-sensory fibers at C7 and C8 spinal segments (*spinal segment*: C7 and C8) across different cathode configurations (*cathode*

configuration: $C6_L$, $C6_M$, $C6_S$, $C7_L$, $C7_M$, $C7_S$, $T1_L$, $T1_M$, and $T1_S$) are summarized in Figure 4.4. For α-motor fibers, our results showed significant interactions between *spinal segment* and *cathode configuration* factors (F(1.150, 39.098)=26.419, p<.001). Since interactions were found, comparisons across *cathode configuration* were performed for each spinal segment using one-way ANOVA tests. Statistically significant differences between cathode configurations were found for both C7 and C8 spinal segments (*C7*: F(1.158, 19.692)=224.231, p<.001; *C8*: F(1.143, 19.426)=134.161, p<.001). Multiple-pairwise comparisons were thus performed using Bonferroni corrections, which are shown in Figure 4.4A. Moreover, comparisons across *spinal segment* were performed for each cathode configurations using t-tests. Statistically significant differences between C7 and C8 spinal segments were found for all cathode configurations ($C6_L$: t(34) = -14.193, p<.001; $C6_M$: t(34) = -13.721, p<.001; $C6_S$: t(34) = -13.142, p<.001; $C7_L$: t(34) = -14.914, p<.001; $C7_M$: t(34) = -14.112, p<.001;$C7_S$: t(34) = -13.521, p<.001; $T1_L$: t(34) = -14.384, p<.001; $T1_M$: t(34) = -13.415, p<.001; and $T1_S$: t(34) = -13.217, p<.001). All α-motor fibers at C7 spinal segment were recruited at lower stimulation intensities compared with C8 spinal segment (Figure 4.4A). For Aα-sensory fibers, our results showed significant interactions between *spinal segment* and *cathode configuration* factors (F(1.324, 45.025)=84.151, p<.001). Since interactions were found, comparisons across *cathode configuration* were performed for each spinal segment using one-way ANOVA tests. Statistically significant differences between cathode configurations were found for both C7 and C8 spinal segments (*C7*: F(1.247, 21.203)=355.280, p<.001; *C8*: F(1.249, 21.236)=206.320, p<.001). Multiple-pairwise comparisons were thus performed using Bonferroni corrections, which are shown in Figure 4.4B. Moreover, comparisons across *spinal segment* were performed for each cathode configurations using t-tests. Statistically significant differences between C7 and C8 spinal segments were found for all cathode configurations ($C6_L$: t(34) = -16.043, p<.001; $C6_M$: t(34) = -15.648, p<.001; $C6_S$: t(34) = -15.460, p<.001; $C7_L$: t(34) = -

14.992, p<.001; $C7_M$: t(34) = -14.535, p<.001;$C7_S$: t(34) = -14.086, p<.001; $T1_L$: t(34) = -14.909, p<.001; $T1_M$: t(34) = -14.567, p<.001; and $T1_S$: t(34) = -14.453, p<.001). All Aα-sensory fibers at C7 spinal segment were recruited at lower stimulation intensities compared with C8 spinal segment (Figure 4.4B). In some cases, the recruitment of the nerve fibers at the C7 spinal segment was optimal for the T1 cathode position (c.f., activation thresholds for C7 fibers using L and M cathode sizes in Figure 4.4B), whereas the recruitment of fibers at the C8 spinal segment was optimal for the C7 cathode position (c.f., activation thresholds for C8 fibers using M and S cathode sizes in Figure 4.4B). Nonetheless, the C6 cathode configuration elicited the highest activation thresholds for each cathode size examined.

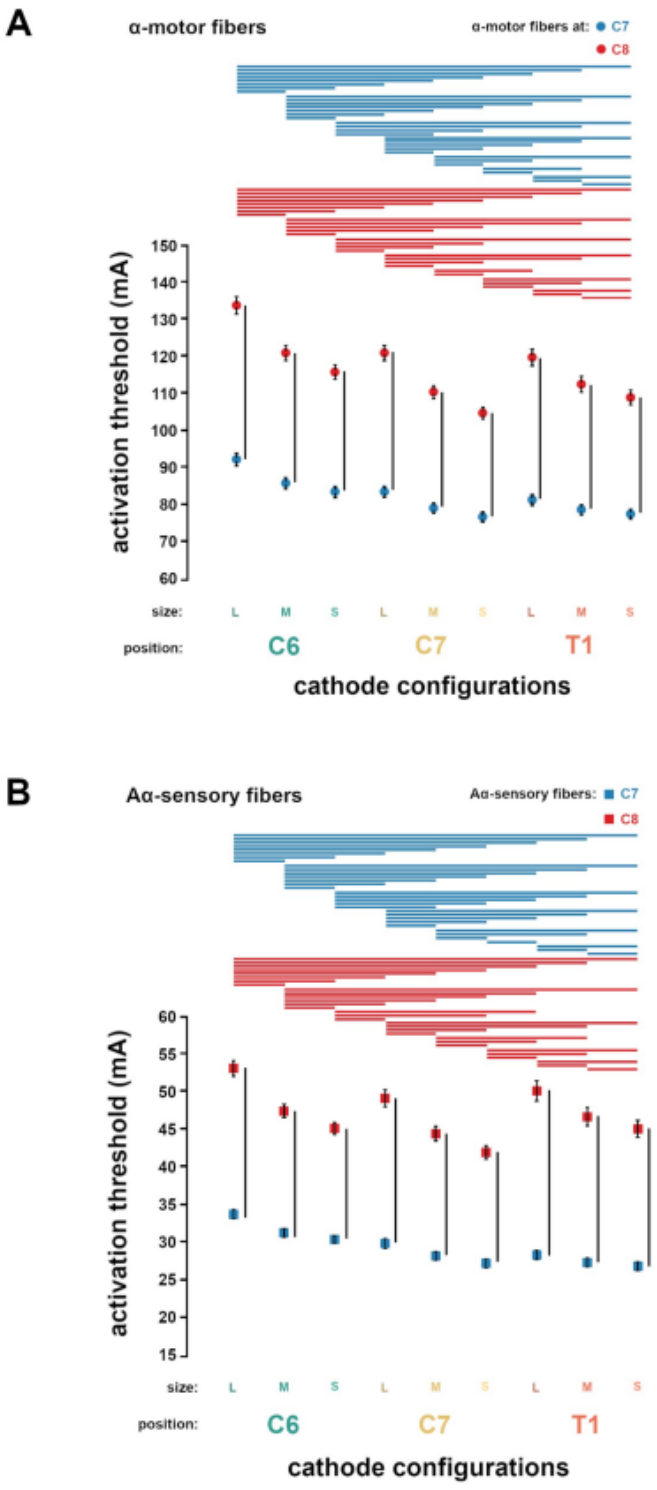

Figure 4.4 – Difference between activation thresholds of fibers at C7 and C8 spinal segments: A) Activation thresholds (mA) of α-motor fibers at C7 (blue) and C8 (red) spinal segments estimated using nine different cathode configurations. The cathode configurations include three vertebral level positions: C6, C7, and T1 vertebral levels; and three cathode sizes: 5.0 x 5.0 cm² (L), 3.5 x 3.5 cm² (M), and 2.5 x 2.5 cm² (S). (B) Activation thresholds of Aα-sensory fibers at C7 (blue) and C8 (red) spinal segments estimated using the same nine cathode configurations. The fiber length is the distance along the fiber trajectory, starting from clavicle level (0 mm) and terminating at the center of gray matter structure (maximum fiber length). The circles and squares in (A) and (B) indicate the activation threshold means, along with vertical bars showing the standard errors. The spinal segments and the cathode configurations were compared using two-way ANOVA test. Statistically significant differences found between cathode configurations and spinal segments are indicated by horizontal and vertical bars, respectively.

CHAPTER IV

Comparisons between α-motor and Aα-sensory fibers

Comparison results between α-motor and Aα-sensory fibers pooled together from C7 and C8 spinal segments (*fiber type*: *α-motor* and *Aα-sensory*) across different cathode configurations (*cathode configuration*: $C6_L$, $C6_M$, $C6_S$, $C7_L$, $C7_M$, $C7_S$, $T1_L$, $T1_M$, and $T1_S$) are summarized in Figure 4.5. Our results showed significant interactions between *fiber type* and *cathode configuration* factors ($F(2.012, 140.844)=50.176$, $p<.001$). Since interactions were found, comparisons across *cathode configuration* were performed for each fiber type using one-way ANOVA tests. Statistically significant differences between cathode configurations were found for both α-motor and Aα-sensory fibers (*α-motor*: $F(1.909, 66.803)=159.978$, $p<.001$; *Aα-sensory*: $F(1.249, 43.732)=115.813$, $p<.001$). Multiple-pairwise comparisons were thus performed using Bonferroni corrections, which are shown in Figure 4.5. Moreover, comparisons across *fiber type* were performed for each cathode configurations using t-tests. Statistically significant differences between α-motor and Aα-sensory fibers were found for all cathode configurations ($C6_L$: $t(70) = -16.580$, $p<.001$; $C6_M$: $t(70) = -17.965$, $p<.001$; $C6_S$: $t(70) = -18.777$, $p<.001$; $C7_L$: $t(70) = -16.336$, $p<.001$; $C7_M$: $t(70) = -18.009$, $p<.001$;$C7_S$: $t(70) = -19.132$, $p<.001$; $T1_L$: $t(70) = -15.142$, $p<.001$; $T1_M$: $t(70) = -16.241$, $p<.001$; and $T1_S$: $t(70) = -16.992$, $p<.001$). All Aα-sensory fibers were recruited at lower stimulation intensities compared with α-motor fibers (Figure 5). For each cathode size, no differences were found between C7 and T1 cathode positions. The activation thresholds of α-motor and Aα-sensory fibers were highest when the cathode was positioned over the C6 vertebrae.

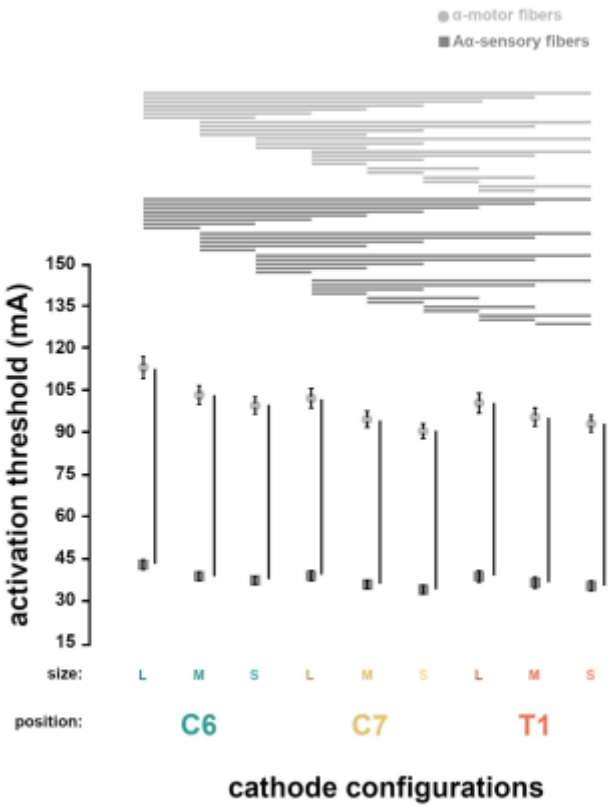

Figure 4.5 – Difference between activation thresholds of motor and sensory fibers: Activation thresholds (mA) of α-motor (light gray circle) and Aα-sensory (dark gray square) fibers estimated using nine different cathode configurations. The cathode configurations include three vertebral level positions: C6, C7, and T1 vertebral levels; and three cathode sizes: 5.0 x 5.0 cm² (L), 3.5 x 3.5 cm² (M), and 2.5 x 2.5 cm² (S). The activation thresholds of α-motor and Aα-sensory fibers at C7 and C8 spinal segments were pooled together. The α-motor and Aα-sensory fibers were compared across cathode configurations using two-way ANOVA test. The circles and squares indicate the activation threshold means, along with vertical bars showing the standard errors. Statistically significant differences found between cathode configurations and spinal segments are indicated by horizontal and vertical bars, respectively.

4.4. Discussions

We developed an anatomically realistic cervical tSCS computational model to analyze the activation of motor and sensory fibers at C7 and C8 spinal segments across nine different cathode electrode configurations. To optimize the activation of sensory fibers, we used the activation threshold as a dependent variable, while manipulating and comparing different cathode configurations. First, our results demonstrated lower activation thresholds of sensory fibers at both C7 and C8 spinal segments by positioning the cathode electrodes at the C7 or T1 vertebral levels, compared with the C6 position. We also found that smaller cathodes required

lower stimulation intensities to activate the nerve fibers. Smaller electrodes could also achieve a degree of selectivity to activate sensory fibers at the C8 spinal segment, while larger electrodes also offer a degree of selectivity to recruit fibers at the C7 spinal segment. Importantly, sensory fibers were always recruited at lower stimulation intensities compared with motor fibers.

4.4.1. Nerve fiber activation at different cervical spinal segments could be optimized using cathode configuration

Previous experimental results showed facilitated activation of distal hand muscles when the cathode was positioned at the C7 or T1 vertebral levels, compared with the placement over the C6 vertebrae (de Freitas et al., 2021). These results implied that optimized activation of caudal segments of the cervical spinal cord (e.g., C7 and C8 spinal segments), where the hand muscle motor pools are mostly organized (e.g., first dorsal interosseous and abductor pollicis brevis muscles) (Kendall et al., 2005; McIntosh et al., 2022), could be achieved with cathode placement at the C7 or T1 vertebral levels. Our simulation results showed highest activation thresholds when the cathode was positioned over the C6 vertebrae (Figure 4.4 and 4.5). These results suggest less effective activation of Aα-sensory fibers at rostral spinal segments, in agreement with previous experimental findings in which inter-individual anatomical variabilities in young adults were accounted for (de Freitas et al., 2021). Moreover, contrary to our hypothesis, our results also demonstrated that sensory fibers at C7 and C8 spinal segments were more effectively activated when the cathode electrode was configured at the T1 and C7 positions, respectively. This result could be explained by the position of the fibers in relation to the cathode electrode and the vertebra, as shown in (Ladenbauer et al., 2010). Nonetheless, when fibers at C7 and C8 spinal segments were pooled together for analysis, no differences were found between C7 and T1 cathode positions (Figure 4.5), suggesting a similar degree of

nerve fiber activation between these cathode configurations. Therefore, our results showed a more efficient activation of sensory fibers at caudal cervical spinal segments (i.e., C7 and C8 spinal segments) by positioning the cathode electrode over the C7 or T1 vertebrae.

Consistently across all cathode configurations, our results also showed higher activation thresholds for sensory fibers at the C8 compared with the C7 spinal segment. A possible explanation for this difference is the distinct geometrical curvature of C7 and C8 spinal roots in relation to the spinal cord (Figure 4.3A) (de Freitas et al., 2022a). Another important consideration is the relative proximity of the spinal segments to the anode positioned on the anterior neck, which attained higher electric potentials at the C7 spinal segment compared with the C8 spinal segment (Figure 4.3B). This rationale implies that fibers closer to the anode electrode may be preferentially recruited compared with those located farther away, highlighting a possible relevance of the anode electrode positioning during cervical tSCS (de Freitas et al., 2021). Interestingly, these results suggest that it may be possible to exclusively recruit sensory fibers from a single spinal segment by adjusting the stimulation intensity during cervical tSCS. However, additional simulation and experimental studies are warranted to confirm sensory fiber activations using different anode configurations and the effects of spinal curvature.

For sensory fiber activations at the C7 spinal segment, the optimal cathode placement was shown to be the T1 position when using L or M electrodes (Figure 4.4B); moreover, the cathode placement over the C7 vertebrae was equally efficient for activating sensory fibers as when it was placed over the T1 vertebrae for the S size electrodes (Figure 4.4B). On the contrary, when examining sensory fiber recruitment at the C8 spinal segment, the optimal cathode placement was the C7 position using the S size electrodes, whereas the C7 position was similar to the T1 cathode placement when L size electrodes were used (Figure 4.4B). These results suggest that reducing the cathode size could affect the degree of nerve fiber activations

at the C8 spinal segment, which agrees with our hypothesis. Nonetheless, the reverse effects observed for the sensory fibers at the C7 spinal segment may be explained by the distance between the transcutaneous electrodes and the targeted nerve fibers, which is also supported by results showing a decrease in selectivity when epidural electrode were moved away from the targeted dorsal root sensory fibers (Greiner et al., 2021; McIntosh et al., 2022). Importantly, our results also demonstrated that smaller electrodes required lower stimulation intensities to activate the sensory fiber (Figure 4.4 and 4.5). Therefore, smaller electrodes could be used to attain a degree of selectivity to activate sensory fibers at the C8 spinal segment during non-invasive cervical spinal stimulation, while requiring lower stimulation intensity compared with larger electrodes.

4.4.2. Sensory and motor fiber recruitment during cervical tSCS

The activation of sensory fibers using cervical tSCS without the co-activation of motor fibers was suggested to be crucial for achieving activity-dependent neuromodulation during upper-limb rehabilitation (Formento et al., 2018; Milosevic et al., 2019b; Rowald et al., 2022). In previous experimental studies, muscle-level motor evoked potentials were used to infer preferential recruitment of sensory fibers (Milosevic et al., 2019b; de Freitas et al., 2021; Sasaki et al., 2021). In agreement with our hypothesis, our simulation results showed lower activation thresholds of Aα-sensory fibers compared to α-motor fibers for both C7 and C8 spinal segments (Figure 4.4 and 4.5). Taken together, these findings corroborate previous experimental and simulation studies (Milosevic et al., 2019b; de Freitas et al., 2021, 2022a; Sasaki et al., 2021), confirming that preferential recruitment of sensory fibers could be achieved at lower stimulation intensities during cervical transcutaneous stimulation.

4.4.3. Implications for experimental and clinical applications

Irrespective of the cathode electrode size, our results showed that C7 or T1 cathode positions were most efficient to activate C7 and C8 spinal segment nerve fibers, where distal hand muscle motor pools are primarily organized (Kendall et al., 2005; McIntosh et al., 2022) (Figure 4.4 and 4.5). Moreover, Aα-sensory fibers were preferentially recruited using lower stimulation intensities compared with α-motor fibers (Figure 4.5). Therefore, hand muscle activations could be facilitated by positioning the cathode electrode at the C7 or T1 vertebral levels, and stimulation intensity should be adjusted around or below the muscle motor threshold levels to recruit Aα-sensory fibers without co-activating the α-motor fibers (de Freitas et al., 2022a). It is important to note that we did not simulate continuous biphasic stimulation pulses which are most commonly used in therapeutic tSCS applications (Gad et al., 2018; Benavides et al., 2020; Inanici et al., 2021), thus caution should be taken when interpreting our results for clinical use. For instance, sensory fibers could be activated at lower stimulation intensities using biphasic pulses compared with monophasic pulses (Field-Fote et al., 2003). Nonetheless, the groups of nerve fibers activated during continuous stimulation (Gad et al., 2018; Benavides et al., 2020; Inanici et al., 2021) is similar to that activated during single-pulse stimulation (Hofstoetter et al., 2015a; Zheng & Hu, 2020a). Furthermore, use of smaller cathode electrodes at C7 or T1 vertebral levels could offer means for optimizing activation of sensory fibers projecting to the hand muscles, while requiring lower stimulation intensities. However, further studies are needed to confirm this observation, and to apply our modelling approach for further reducing the parameter space of electrode configurations used during cervical tSCS. This could help substantially reduce the burden on clinical experimentation. Our current study is a proof-of-principle demonstrating the utility of cervical tSCS models for optimizing sensory fiber activations using different electrode configurations.

4.4.4. Limitations

A limitation of the 3D geometry used in our simulations is the representation of only two spinal segments (i.e., C7 and C8). However, the dorsal and ventral roots and rootlets structure, as well as the spinal canal curvature, were developed to represent the curvature of the nerve fibers with realistic anatomical considerations (Figure 4.3A) (Ladenbauer et al., 2010; Danner et al., 2011). Importantly, although we did not include a large variability of the nerve fiber trajectories in the spinal tracts and diameter sizes in our simulations, our outcomes were consistent with previous experimental findings (Milosevic et al., 2019b; de Freitas et al., 2021). Inter-individual gross anatomical features were also not included in our simulations as non-invasive electrodes are placed relatively far away from the targeted neural structures. Future studies should compare the effects of inter-individual anatomical features (e.g., sensitivity analyses) and consider the development of personalized models for optimizing placement of stimulating electrodes (Rowald et al., 2022). Another limitation of our simulations was neglecting capacitive effects of the body tissues, which may decrease the activation thresholds of nerve fibers (Kuhn et al., 2009). However, assuming all materials to be purely resistive is a reasonable approximation in our model for the 2 ms stimulation pulse and conductivity values shown in Table 4.1 (Bossetti, Birdno & Grill, 2008). Furthermore, to fully translate our findings for therapeutic applications in rehabilitation (Gad et al., 2018; Benavides et al., 2020; Inanici et al., 2021), simulations using the Gaines models should also consider neurodegenerative processes (e.g., nerve fiber demyelination), which takes place after spinal cord injury and could affect nerve fiber activations. In the future, the geometrical model should also include more rostral spinal segments and other fiber groups to analyze their activation at spinal segments where proximal arm muscle motor pools are organized (Kendall et al., 2005; McIntosh et al., 2022). Moreover, non-uniform spatial distribution of nerve fiber trajectories in the spinal tracts

and distributions of fiber diameter sizes should be considered in the future to improve the simulations.

4.5. Conclusions

Our computational simulations showed that more caudal cathode electrode positioning (C7 or T1 vertebral levels) was more effective to activate nerve fibers at C7 and C8 spinal segments compared with the more rostral position (C6 vertebrae). We also found that smaller cathodes required lower stimulation intensities to activate the Aα-sensory fibers, while they could also affect the degree of activation across different positions. Importantly, sensory fibers were always recruited at lower stimulation intensities compared with the motor fibers. Overall, our results suggest that positioning cathode electrodes at the C7 or T1 vertebral levels could optimize activation of hand muscles during cervical tSCS.

CHAPTER V

General conclusions

5.1. Scientific contributions

Previous studies have suggested that spatiotemporal activation of sensory fibers during tSCS is critical for effective motor recovery after spinal cord injury (Gerasimenko et al., 2015a; Moraud et al., 2016; Wenger et al., 2016; Minassian et al., 2016; Taccola et al., 2018; Capogrosso et al., 2018; Formento et al., 2018; Seáñez & Capogrosso, 2021; Barss et al., 2022). To analyze the neural targets activated during cervical tSCS and improve the spatiotemporal activation of sensory fibers, I conducted three studies using experimental and computational approaches. Specifically, the objectives of these studies were: 1) to analyze the activation of different groups of motor and sensory fibers during cervical tSCS with computational simulations (Chapter II); 2) to examine the selectivity and excitability of different spinal segments using different cathode (C6, C7, and T1 positions) and anode (neck, shoulders, iliac crests, and back) electrode configurations in a experimental study (Chapter III); 3) to analyze the activation of motor and sensory fibers at two spinal segments (i.e., C7 and C8 spinal segments) with computational simulations of different cathode electrode configurations (Chapter IV). Through these investigations, in brief, I could conclude that 1) groups of proprioceptive and cutaneous sensory fibers were co-activated at lower stimulation intensities compared with motor fibers; 2) hand muscles were more effectively activated when the cathode was placed at C7 or T1 vertebral level, while the anode was placed at the anterior neck; 3) proximal arm muscles were recruited at lower stimulation intensities compared with distal hand muscles; and 4) sensory fibers at C7 and C8 spinal segments were more effectively recruited

using small cathode electrodes placed at C7 or T1 vertebral levels. Taking together, these results contributed for a better understanding of the neural targets of non-invasive cervical tSCS, and also for informing stimulation configuration parameters to improve rehabilitation protocols.

5.2. Nerve fiber activation during cervical tSCS

A computational model was developed and used to compare the activation of motor, proprioceptive sensory and cutaneous sensory nerve fibers during cervical tSCS (Chapter II). My simulation results showed co-activation of groups of proprioceptive and cutaneous at lower stimulation intensities compared with motor fibers, corroborating the previous experimental results found by Milosevic and colleagues (Milosevic et al., 2019b). Specifically, the recruitment of sensory fibers at lower stimulation intensities compared with motor fibers could be explained by the physiological differences between motor and sensory fibers which are implemented in the compartment model used in the simulations (Gaines et al., 2018). Moreover, the co-activation of proprioceptive and cutaneous fibers could be explained by their different trajectories after the rootlet-white matter interface (Figure 2.3). Importantly, these results suggest a sizable contribution of proprioceptive and cutaneous fiber activations for upper-limb motor recovery after spinal cord injury.

5.3. Cervical tSCS selectivity and excitability

To examine the selectivity and excitability of cervical spinal segments during cervical tSCS, motor evoked responses recorded from four proximal arm muscles (BB, TB, FCR, and ECR) and two distal hand muscles (FDI and APB) were compared using different cathode (C6, C7, and T1) and anode (neck, shoulders, iliac crests, and back) electrode configurations

(Chapter III). My results showed preferential activation of distal hand muscles (FDI and APB) using C7 and T1 cathode configurations compared with C6 cathode position. Considering the organization of the motor pools of proximal and distal upper-limb muscles along the rostral and caudal extent of the cervical spinal cord (Kendall et al., 2005), these results suggested that caudal spinal segments were preferentially activated when the cathode electrode was placed at C7 and T1 vertebral levels. For all cathode configurations, the motor threshold of distal hand muscles was higher compared with proximal arm muscles. Moreover, motor evoked responses elicited using the neck anode position were higher compared with the other anode configurations (shoulders, iliac crests, and back). Taking together, these results showed that the transsynaptic activation of motor pools projecting to the upper limb muscles can be affected using different cervical tSCS cathode and anode configurations.

5.4. Optimization of sensory fiber recruitment

To analyze the activation of nerve fibers at cervical spinal segments using different configurations of cervical tSCS electrodes, the recruitment of sensory and motor fibers was simulated using different cathode positions and sizes (Chapter IV). My simulation results showed more effective activation of sensory fibers at C7 and C8 spinal levels when the cathode electrode was positioned on the C7 and T1 vertebral levels compared with C6 cathode position, corroborating my previous experimental results (de Freitas et al., 2021). These results could be explained by the relative position of the cathode and anode electrodes to the nerve fibers at C7 and C8 spinal segments, which affected the extraneural distribution of electric potentials along the sensory and motor fibers. Moreover, sensory fibers were activated at lower stimulation intensities when small cathode electrodes were used. In conclusion, this methodological approach is a proof of principle demonstrating that computational simulations can complement

experimental approaches towards optimization of electrodes configuration for rehabilitation applications.

5.5. Informing therapeutic applications of cervical tSCS

In summary, to improve cervical tSCS rehabilitation effectiveness, the following settings should be considered when the cathode is placed between C6 and T1 vertebral levels and the anode is fixed on the anterior neck: (1) low stimulation intensities should be used to recruit mostly proprioceptive and cutaneous sensory fibers, while not activating motor fibers (de Freitas et al., 2022a). For instance, the stimulation intensity can be configured to elicit paresthesia sensations (Hofstoetter et al., 2015b; Sasaki et al., 2021), which indicates activation of cutaneous sensory fibers (Barolat et al., 1993; Greiner et al., 2021). Alternatively, the stimulation intensity can be configured around the level to elicit motor potentials through proprioceptive spinal reflex (Hofstoetter et al., 2015b; Benavides et al., 2020; Kumru et al., 2021); (2) low stimulation intensities should also be used to selectively activate only proximal arm muscles, without activation of hand muscles (de Freitas et al., 2021); (3) small cathode electrodes should be placed at C7 or T1 vertebral levels to maximize the activation of hand muscles (de Freitas et al., 2021, 2022b).

5.6. Future directions

The series of studies presented herein show a proof of principle that experimental and computational simulations can help further understanding the neural mechanisms during cervical tSCS and optimize rehabilitation protocols. Nevertheless, future studies should be carried out using more sophisticated computational simulations and complementing experiments. In particular, selectivity and excitability of different cervical spinal segments

should be further investigated using different anode configurations, such as the iliac crests position (Inanici et al., 2018; Gad et al., 2018; Freyvert et al., 2018; Benavides et al., 2020). Computational simulation studies should complement experimental findings, serving as a high-speed methodological approach to limit the parameter space of electrode configurations and optimize spatiotemporal recruitment of sensory fibers at multiple spinal segments (de Freitas et al., 2022b). Moreover, subject-specific computational models should also be developed to account for between-subject characteristics (Rowald et al., 2022). These personalized models could be used to adjust the stimulation electrodes, and optimize sensory fiber activation considering individual anatomical proportions.

Appendix

A.1. Mesh size of the geometrical model

In the Chapter II and IV, the proper adjustment of the mesh size was critical to efficiently converge the FEM simulation results. To confirm that the quality of the mesh was suitable for these simulations, the activation threshold of a sensory fiber was estimated with the geometrical model used in Chapter II and the same geometrical model meshed with more tetrahedral elements. Specifically, the number of tetrahedral elements in the general body and the muscles of the back were increased, i.e., the mesh size was decreased (Figure A.1). The new meshed geometry was composed with approximately 28 million tetrahedral elements, i.e., 3.3 times more elements compared with the meshed geometry in Chapter II.

The activation threshold estimated with the geometrical model used in Chapter II was 34.096 mA, whereas the activation threshold estimated with the geometrical model meshed with more elements was 34.207 mA. The difference between the two meshed geometries was 0.111 mA, which is relatively small compared with the difference of activation thresholds between groups of fibers in Chapter II and between cathode configurations in Chapter IV. In fact, the distribution of electric potential along the sensory fiber has a very small variation for increasing the number of mesh elements (Figure A.1), which minimally affected the simulation results. Importantly, more computational memory is required for more fine meshes, which may be a limitation factor for FEM simulations. Therefore, the mesh size used in Chapter II and Chapter IV is suitable to efficiently converge finite element method simulation results.

APPENDIX

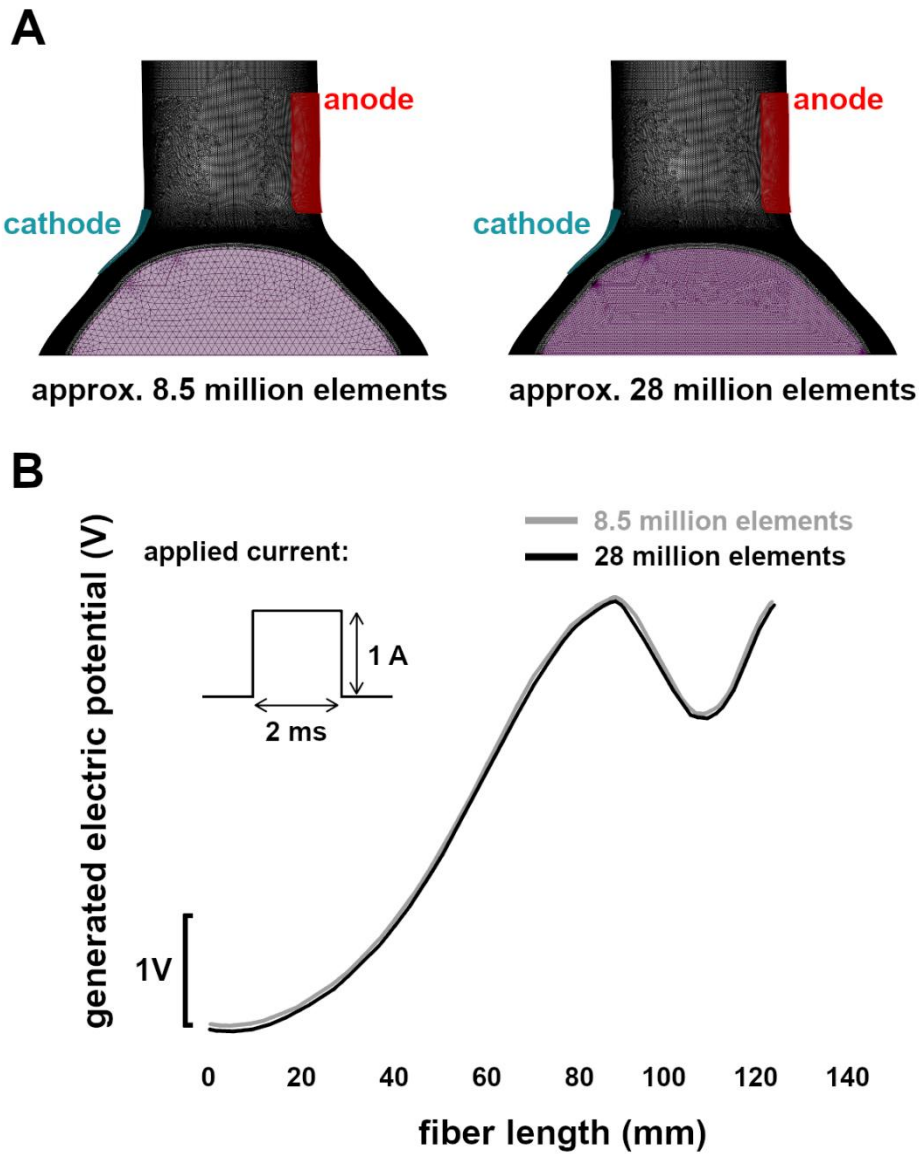

Figure A.1 – Effect of mesh size on activation thresholds: (A) On the left, the meshed geometry used in the finite element method simulations of the Chapter II with approximately 8.5 million tetrahedral elements. On the right, the same geometry is meshed with 28 million tetrahedral elements. (B) Distributions of electric potential along the extent of a sensory fiber estimated with finite element method for the geometry meshed with 8.5 million tetrahedral elements (gray) and for the geometry meshed with 28 million tetrahedral elements (black). The distribution of electric potential has a small variation for the increase of mesh elements.

APPENDIX

A.2. Finite element method equations

In Chapter II and IV, finite element method was used to estimate the distribution of electric potential along motor and sensory fibers during cervical tSCS. Specifically, the governing equation of this electromagnetic system is the Laplace equation:

$$\boldsymbol{\sigma \nabla^2 V = 0} \tag{A.1}$$

In Equation A.1, $\boldsymbol{\sigma}$ is the conductivity of tissues/materials (Table 2.1 and 4.1), $\boldsymbol{V}$ is the electric potential in the three-dimension geometry, and $\nabla^2$is the Laplace operator. The Laplace equation was solved for the boundary conditions below.

For the anode electrode, the boundary condition in Equation A.2 was applied to its largest external surface, such that 1 A electric current was injected. In Equation A.2, $\boldsymbol{n}$ is the normal vector, and A_{anode} is the total area of the largest external surface of the anode, i.e., approximately 75 cm^2.

$$\boldsymbol{n.\sigma \nabla V} = 1/A_{anode} \tag{A.2}$$

For the cathode electrode, the boundary condition in Equation A.3 was applied to its largest external surface, such that the electric potential is zero.

$$\boldsymbol{V = 0} \tag{A.3}$$

Except for the anode and cathode electrodes, the boundary condition in Equation A.4 was applied to the other external surfaces of the geometry, such that the system is isolated, i.e., net charge is constant.

$$\boldsymbol{n.\sigma \nabla V = 0} \tag{A.4}$$

APPENDIX

Inside the geometry, the boundary condition in Equation A.5 was applied to the interface between two surfaces, thus enabling continuity of the electric field.

$$\boldsymbol{n_o}.\boldsymbol{\sigma_o}\nabla\boldsymbol{V_o} - \boldsymbol{n_i}.\boldsymbol{\sigma_i}\nabla\boldsymbol{V_i} = \mathbf{0} \quad \text{(A.5)}$$

A.3. Compartment model equations

The Gaines model was used to simulate motor and sensory fibers in Chapter II and IV. The membrane of node (NODE) and internode (MYSA, FLUT, and STIN) segments are composed of ion gate channels. Generically, the ion channel currents are described in Equation A.6, where g_{ion} is the channel conductance, γ is a stochastic variable that defines the gating state, V^i is the membrane potential, and E_{ion} is the reversal potential of the ion channel.

$$I_{ion} = g_{ion}\gamma(V^i - E_{ion}) \quad \text{(A.6)}$$

The stochastic variable γ is defined with Equation A.7 in terms of α_γ and β_γ, which are determined differently for each ion channel. The specific equations of α_γ and β_γ are shown below for a temperature constant $\phi = 1.116$, i.e., internal temperature of 37°C. The values of A, B and C are defined in Table A.1 and A.2 for motor and sensory fibers, respectively.

$$\frac{d\gamma}{dt} = \alpha_\gamma(1-\gamma) - \beta_\gamma.\gamma \quad \text{(A.7)}$$

APPENDIX

For fast sodium channels (Na), the ion channel current is given by Equation A.8 in terms of the *m* and *h* factors. The α_m, β_m, α_h and β_h factors are given by Equation A.9, A.10, A.11, and A.12, respectively.

$$I_{Na} = g_{Na} m^3 h (V^i - E_{Na}) \tag{A.8}$$

$$\alpha_m = \phi \frac{A(V^i + B)}{1 - e^{[-\frac{V^i + B}{C}]}} \tag{A.9}$$

$$\beta_m = \phi \frac{A(-(V^i + B))}{1 - e^{[\frac{V^i + B}{C}]}} \tag{A.10}$$

$$\alpha_h = \phi \frac{A(-(V^i + B))}{1 - e^{[\frac{V^i + B}{C}]}} \tag{A.11}$$

$$\beta_h = \phi \frac{A}{1 + e^{[-\frac{V^i + B}{C}]}} \tag{A.12}$$

For persistent sodium channels (Na_p), the ion channel current is given by Equation A.13 in terms of the p factor. The α_p and β_p factors are given by Equation A.14 and A.15, respectively.

$$I_{Nap} = g_{Nap} p^3 (V^i - E_{Nap}) \tag{A.13}$$

APPENDIX

$$\alpha_p = \phi \frac{A(V^i + B)}{1 - e^{[-\frac{V^i+B}{C}]}} \tag{A.14}$$

$$\beta_p = \phi \frac{A(V^i + B))}{1 - e^{[\frac{V^i+B}{C}]}} \tag{A.15}$$

For slow potassium channels (K_s), the ion channel current is given by Equation A.16 in terms of the *s* factor. The α_s and β_s factors are given by Equation A.17 and A.18, respectively.

$$I_{Ks} = g_{Ks} s (V^i - E_{Ks}) \tag{A.16}$$

$$\alpha_s = \phi \frac{A}{1 + e^{[\frac{V^i+B}{C}]}} \tag{A.17}$$

$$\beta_s = \phi \frac{A}{1 + e^{[\frac{V^i+B}{C}]}} \tag{A.18}$$

For fast potassium channels (K_f), the ion channel current is given by Equation A.19 in terms of the *n* factor. The α_n and β_n factors are given by Equation A.20 and A.21, respectively.

$$I_{Kf} = g_{Kf} n^4 (V^i - E_{Kf}) \tag{A.19}$$

APPENDIX

$$\alpha_n = \phi \frac{A(V^i - B)}{1 - e^{\left[\frac{-V^i + B}{C}\right]}} \tag{A.20}$$

$$\beta_n = \phi \frac{A(V^i - B)}{1 - e^{\left[\frac{V^i - B}{C}\right]}} \tag{A.21}$$

For hyperpolarization-activated cyclic-nucleotide-gated (HCN) channels (H), the ion channel current is given by Equation A.22 in terms of the q factor. The α_q and β_q factors are given by Equation A.23 and A.24, respectively.

$$I_q = g_q q(V^i - E_q) \tag{A.22}$$

$$\alpha_q = \phi A e^{\left(\frac{V^i - B}{C}\right)} \tag{A.23}$$

$$\beta_q = \phi \frac{A}{e^{\left(\frac{V^i - B}{C}\right)}} \tag{A.24}$$

Finally, leak currents are given by Equation A.25, which does not depend on gating channel parameters.

APPENDIX

$$I_{Lk} = g_{Lk}(V^i - E_{Lk}) \tag{A.25}$$

Internode segments

Figure A.2 depicts the circuit diagram of the internode segments (i.e., MYSA, FLUT, and STIN), which indicates the extraneural potential as E^e, the periaxonal potential as E^p and the intraneural potential as E^i. The nerve fiber membrane of the internode segments is composed of fast potassium, slow potassium, HCN, and leak channels. The membrane potential is defined in Equation A.26, while the periaxonal potential is defined in Equation A.27.

$$V_k^i = E_k^i - E_k^p \tag{A.26}$$

$$V_k^p = E_k^p - E_k^e \tag{A.27}$$

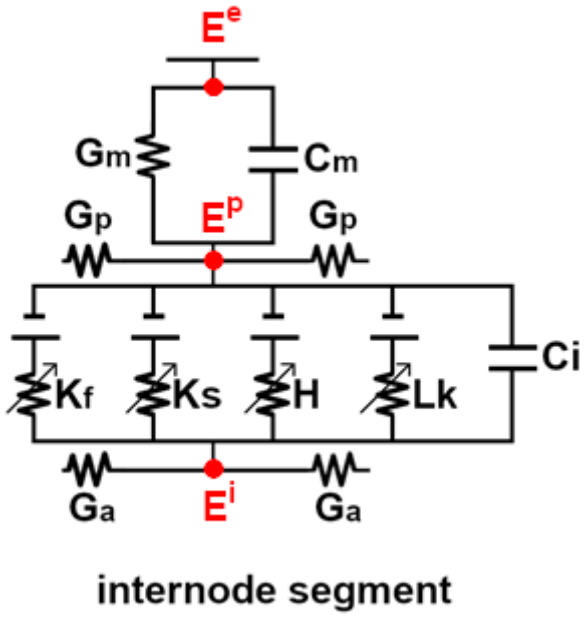

Figure A.2 – Circuit diagram of internode segment: The internode segment includes: fast K^+ (K_f), slow K^+ (K_s), leak current (L_k) and HCN (H) channels. The extraneural potential E^e, periaxonal potential E^p and intraneural potential E^i are indicated in red. Legend – C_i: internodal capacitance, C_m: myelin capacitance, G_a: axoplasmic conductance, G_p: periaxonal conductance, and G_m: myelin conductance.

APPENDIX

At the intraneural node, the Kirchhoff's law is applied resulting in Equation A.28. For the segment k, Equations A.29 and A.30 are derived by applying the Ohm's law to the currents to the $I_k^{i,left}$ and $I_k^{i,right}$. In the Equation A.29 and A.30, the axoplasmic resistance $R_k^a = 1/G_k^a$.

$$I_k^{i,left} + I_k^{i,right} + I_k^{i,mem} = 0 \tag{A.28}$$

$$I_k^{i,left} = \frac{E_k^i - E_{k-1}^i}{\frac{R_k^a + R_{k-1}^a}{2}} \tag{A.29}$$

$$I_k^{i,right} = \frac{E_k^i - E_{k+1}^i}{\frac{R_k^a + R_{k+1}^a}{2}} \tag{A.30}$$

The membrane current I_k^{mem} is the sum of the currents of fast potassium (Equation A.19), slow potassium (Equation A.16), HCN (Equation A.22) and leak (Equation A.25) channels, as well as the capacitive membrane current $I_k^{mem,cap}$:

$$I_k^{mem} = I^{Kf} + I^{Ks} + I^H + I^{Lk} + I_k^{mem,cap} \tag{A.31}$$

Substituting Equation A.28 in Equation A.31, we obtain:

$$I^{Kf} + I^{Ks} + I^H + I^{Lk} + C_k^{mem}.\frac{d(E_k^i - E_k^p)}{dt} = -I_k^{i,left} - I_k^{i,right} \tag{A.32}$$

APPENDIX

The differential equation of the membrane potential is thus derived:

$$\frac{dV_k^i}{dt} = -\left(I^{Kf} + I^{Ks} + I^H + I^{Lk} + I_k^{i,left} + I_k^{i,right}\right)/C_k^{mem} \quad \text{(A.33)}$$

At the periaxonal node, the Kirchhoff's law is applied resulting in Equation A.34. Equations A.35 and A.36 are derived by applying the Ohm's law to the currents to $I_k^{p,left}$ and $I_k^{p,right}$ for the segment k. In the Equation A.35 and A.36, the periaxonal resistance $R_k^p = 1/G_k^p$.

$$I_k^{p,left} + I_k^{p,right} + I_k^{myelin} - I_k^{mem} = 0 \quad \text{(A.34)}$$

$$I_k^{p,left} = \frac{E_k^p - E_{k-1}^p}{\frac{R_k^p + R_{k-1}^p}{2}} \quad \text{(A.35)}$$

$$I_k^{p,right} = \frac{E_k^p - E_{k+1}^p}{\frac{R_k^p + R_{k+1}^p}{2}} \quad \text{(A.36)}$$

The myelin current I_k^{myelin} is the sum of the ionic $I_k^{myelin,ion}$ (Equation A.38) and capacitive $I_k^{myelin,cap}$ (Equation A.39) myelin currents:

$$I_k^{myelin} = I_k^{myelin,ion} + I_k^{myelin,cap} \quad \text{(A.37)}$$

APPENDIX

$$I_k^{myelin,ion} = G_k^{myelin}.(E_k^p - E_k^e) \quad \text{(A.38)}$$

$$I_k^{myelin,cap} = C_k^{myelin}.\frac{d(E_k^p - E_k^e)}{dt} \quad \text{(A.39)}$$

Substituting Equation A.28 in Equation A.34, we obtain:

$$I_k^{p,left} + I_k^{p,right} + I_k^{myelin} + I_k^{i,left} + I_k^{i,right} = 0 \quad \text{(A.40)}$$

Finally, the differential equation of the periaxonal potential is thus derived:

$$\frac{dV_k^p}{dt} = -\left(I_k^{p,left} + I_k^{p,right} + I_k^{i,left} + I_k^{i,right} + G_k^{myelin}.V_k^p\right)/C_k^{myelin} \quad \text{(A.41)}$$

Node segments

Figure A.3 depicts the circuit diagram of the node which indicates the extraneural potential as E^e and the intraneural potential as E^i. The nerve fiber membrane of the node segments is composed of fast potassium, slow potassium, fast sodium, persistent sodium, and leak channels.

APPENDIX

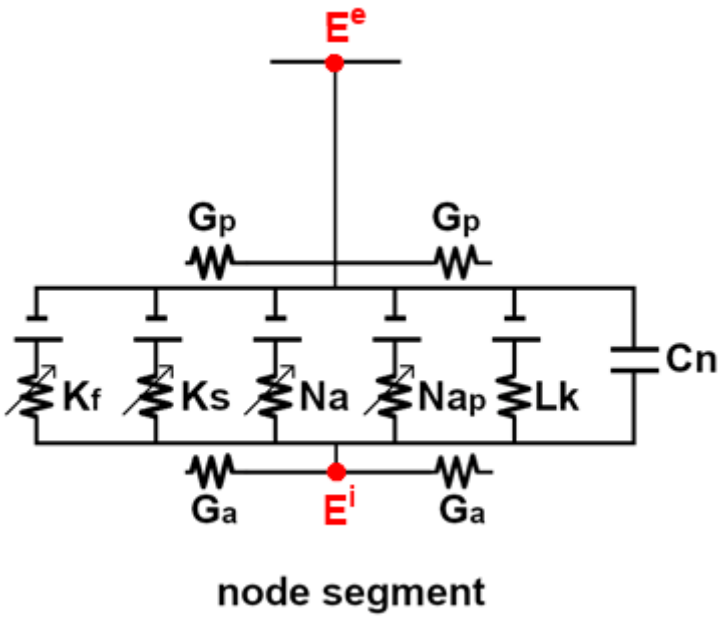

Figure A.3 – Circuit diagram of node segment: The node segment includes: fast K^+ (K_f), slow K^+ (K_s), fast Na^+ (Na), persistent Na^+ (Na_p), and leak current (L_k) channels. The extraneural potential E^e, periaxonal potential E^p and intraneural potential E^i are indicated in red. Legend – C_n: nodal capacitance, G_a: axoplasmic conductance, G_p: periaxonal conductance, and G_m: myelin conductance.

At the intraneural node, the Kirchhoff's law is applied resulting in Equation A.42.

$$I^{mem} = I^{Na} + I^{Nap} + I^{Ks} + I^{Kf} + I^{Lk} + I^{mem,cap} \tag{A.42}$$

Substituting Equation A.28 in Equation A.43, we obtain the differential equation for the membrane potential:

$$\frac{dV_k^i}{dt} = -(I^{Na} + I^{Nap} + I^{Ks} + I^{Kf} + I^{Lk} + I_k^{i,left} + I_k^{i,right})/C_k^{mem} \tag{A.43}$$

APPENDIX

Table A.1: Parameters defined in (Gaines et al., 2018) for simulating motor fibers. Gating channel parameters α_m, α_p, α_h, α_n, α_s, α_q, β_m, β_p, β_h, β_s and β_q are defined in terms of A (ms^{-1}), B (mV) and C (mV). Channel conductance and reversal potential of persistent sodium, fast sodium, slow potassium, hyperpolarization-activated cyclic-nucleotide-gated (HCN) and leak channels are displayed.

	Motor fibers					
	Node			**Internode**		
Potential and time dependent parameter	**A (ms^{-1})**	**B (mV)**	**C (mV)**	**A (ms^{-1})**	**B (mV)**	**C (mV)**
α_m	1.86	20.4	10.3	-	-	-
β_m	0.086	25.7	9.16	-	-	-
α_p	0.01	27	10.2	-	-	-
β_p	0.00025	34	10	-	-	-
α_h	0.062	114.0	11.0	-	-	-
β_h	2.3	31.8	13.4	-	-	-
α_n	0.0462	-83.2	1.1	0.0462	-83.2	1.1
β_n	0.0824	-66	10.5	0.0824	-66	10.5
α_s	0.3	-27	-5	0.3	-27	-5
β_s	0.03	10	-1	0.03	10	-1
α_q	-	-	-	0.00522	-107.3	-12.2
β_q	-	-	-	0.00522	-107.3	-12.2
Channel conductance	**(mS cm^{-2})**			**(mS cm^{-2})**		
Persistent sodium	10			-		
Fast sodium	3000			-		
Slow potassium	80			2.581		
Fast potassium	25.68			150.74 (MYSA); 25.68 (FLUT, STIN)		
Leak	7			2 (MYSA); 0.2 (FLUT, STIN)		
HCN	-			2.232		
Reversal potential	**(mV)**			**(mV)**		
Sodium	50			-		
Slow potassium	-90			-90		
Fast potassium	-90			-90		
Leak	-90			-90		
HCN	-			-54.9		

APPENDIX

Table A.2: Parameters defined in (Gaines et al., 2018) for simulating sensory fibers. Gating channel parameters α_m, α_p, α_h, α_n, α_s, α_q, β_m, β_p, β_h, β_s and β_q are defined in terms of A (ms^{-1}), B (mV) and C (mV). Channel conductance and reversal potential of persistent sodium, fast sodium, slow potassium, hyperpolarization-activated cyclic-nucleotide-gated (HCN) and leak channels are displayed.

	Sensory fibers					
	Node			**Internode**		
Potential and time dependent parameter	**A (ms^{-1})**	**B (mV)**	**C (mV)**	**A (ms^{-1})**	**B (mV)**	**C (mV)**
α_m	1.77753	20.1795	10.3	-	-	-
β_m	0.0823	25.4746	9.16	-	-	-
α_p	0.00957	26.852	10.2	-	-	-
β_p	0.00024	33.8333	10	-	-	-
α_h	0.075286	112.7124	8.391	-	-	-
β_h	2.8083	30.5435	10.2263	-	-	-
α_n	0.0462	-83.2	1.1	0.0462	-83.2	1.1
β_n	0.0824	-66	10.5	0.0824	-66	10.5
α_s	0.3	-27	-5	0.3	-27	-5
β_s	0.03	10	-1	0.03	10	-1
α_q	-	-	-	0.00522	-94.2	-12.2
β_q	-	-	-	0.00522	-94.2	-12.2
Channel conductance	**(mS cm^{-2})**			**(mS cm^{-2})**		
Persistent sodium	10			-		
Fast sodium	3000			-		
Slow potassium	41.06			1.324		
Fast potassium	27.37			164.2 (MYSA); 27.37 (FLUT, STIN)		
Leak	6.005			1.716 (MYSA); 0.1716 (FLUT, STIN)		
HCN	-			3.102		
Reversal potential	**(mV)**			**(mV)**		
Sodium	50			-		
Slow potassium	-90			-90		
Fast potassium	-90			-90		
Leak	-90			-90		
HCN	-			-54.9		

References

Barolat G, Massaro F, He J, Zeme S, Ketcik B. 1993. Mapping of sensory responses to epidural stimulation of the intraspinal neural structures in man. *Journal of Neurosurgery* 78:233–239. DOI: 10.3171/jns.1993.78.2.0233.

Barra B, Conti S, Perich MG, Zhuang K, Schiavone G, Fallegger F, Galan K, James ND, Barraud Q, Delacombaz M, Kaeser M, Rouiller EM, Milekovic T, Lacour S, Bloch J, Courtine G, Capogrosso M. 2022. Epidural electrical stimulation of the cervical dorsal roots restores voluntary upper limb control in paralyzed monkeys. *Nature Neuroscience*. DOI: 10.1038/s41593-022-01106-5.

Barss TS, Parhizi B, Porter J, Mushahwar VK. 2022. Neural Substrates of Transcutaneous Spinal Cord Stimulation: Neuromodulation across Multiple Segments of the Spinal Cord. *Journal of Clinical Medicine* 11:639. DOI: 10.3390/jcm11030639.

Benavides FD, Jo HJ, Lundell H, Edgerton VR, Gerasimenko Y, Perez MA. 2020. Cortical and Subcortical Effects of Transcutaneous Spinal Cord Stimulation in Humans with Tetraplegia. *The Journal of Neuroscience* 40:2633–2643. DOI: 10.1523/JNEUROSCI.2374-19.2020.

Blair EA, Erlanger J. 1933. A COMPARISON OF THE CHARACTERISTICS OF AXONS THROUGH THEIR INDIVIDUAL ELECTRICAL RESPONSES. *American Journal of Physiology-Legacy Content* 106:524–564. DOI: 10.1152/ajplegacy.1933.106.3.524.

Bossetti CA, Birdno MJ, Grill WM. 2008. Analysis of the quasi-static approximation for calculating potentials generated by neural stimulation. *Journal of Neural Engineering* 5:44–53. DOI: 10.1088/1741-2560/5/1/005.

REFERENCES

Buller NP, Garnett R, Stephens JA. 1980. The reflex responses of single motor units in human hand muscles following muscle afferent stimulation. *The Journal of physiology* 303:337–49. DOI: 10.1113/jphysiol.1980.sp013289.

Burke RE, Glenn LL. 1996. Horseradish peroxidase study of the spatial and electrotonic distribution of group Ia synapses on type-identified ankle extensor motoneurons in the cat. *The Journal of comparative neurology* 372:465–85. DOI: 10.1002/(SICI)1096-9861(19960826)372:3<465::AID-CNE9>3.0.CO;2-0.

Cadotte DW, Cadotte A, Cohen-Adad J, Fleet D, Livne M, Wilson JR, Mikulis D, Nugaeva N, Fehlings MG. 2015. Characterizing the Location of Spinal and Vertebral Levels in the Human Cervical Spinal Cord. *American Journal of Neuroradiology* 36:803–810. DOI: 10.3174/ajnr.A4192.

Calabrese E, Adil SM, Cofer G, Perone CS, Cohen-Adad J, Lad SP, Johnson GA. 2018. Postmortem diffusion MRI of the entire human spinal cord at microscopic resolution. *NeuroImage: Clinical* 18:963–971. DOI: 10.1016/j.nicl.2018.03.029.

Capaday C. 1997. Neurophysiological methods for studies of the motor system in freely moving human subjects. *Journal of Neuroscience Methods* 74:201–218. DOI: 10.1016/S0165-0270(97)02250-4.

Capogrosso M, Lempka SF. 2020. A computational outlook on neurostimulation. *Bioelectronic Medicine* 6:10. DOI: 10.1186/s42234-020-00047-3.

Capogrosso M, Wagner FB, Gandar J, Moraud EM, Wenger N, Milekovic T, Shkorbatova P, Pavlova N, Musienko P, Bezard E, Bloch J, Courtine G. 2018. Configuration of electrical spinal cord stimulation through real-time processing of gait kinematics. *Nature Protocols* 13:2031–2061. DOI: 10.1038/s41596-018-0030-9.

REFERENCES

Capogrosso M, Wenger N, Raspopovic S, Musienko P, Beauparlant J, Bassi Luciani L, Courtine G, Micera S. 2013. A Computational Model for Epidural Electrical Stimulation of Spinal Sensorimotor Circuits. *Journal of Neuroscience* 33:19326–19340. DOI: 10.1523/JNEUROSCI.1688-13.2013.

Cavallari P, Katz R. 1989. Pattern of projections of group I afferents from forearm muscles to motoneurones supplying biceps and triceps muscles in man. *Experimental brain research* 78:465–478. DOI: 10.1007/BF00230235.

Cavallari P, Katz R, Penicaud A. 1992. Pattern of projections of group I afferents from elbow muscles to motoneurones supplying wrist muscles in man. *Experimental brain research* 91:311–319. DOI: 10.1007/BF00231664.

Christ A, Kainz W, Hahn EG, Honegger K, Zefferer M, Neufeld E, Rascher W, Janka R, Bautz W, Chen J, Kiefer B, Schmitt P, Hollenbach H-P, Shen J, Oberle M, Szczerba D, Kam A, Guag JW, Kuster N. 2010. The Virtual Family—development of surface-based anatomical models of two adults and two children for dosimetric simulations. *Physics in Medicine and Biology* 55:N23–N38. DOI: 10.1088/0031-9155/55/2/N01.

Courtine G, van den Brand R, Roy RR, Edgerton VR. 2016. Multisystem Neurorehabilitation in Rodents with Spinal Cord Injury. In: *Neurorehabilitation Technology*. Cham: Springer International Publishing, 59–77. DOI: 10.1007/978-3-319-28603-7_4.

Courtine G, Harkema SJ, Dy CJ, Gerasimenko YP, Dyhre-Poulsen P. 2007. Modulation of multisegmental monosynaptic responses in a variety of leg muscles during walking and running in humans. *The Journal of Physiology* 582:1125–1139. DOI: 10.1113/jphysiol.2007.128447.

Courtine G, Sofroniew M V. 2019. Spinal cord repair: advances in biology and technology. *Nature Medicine* 25:898–908. DOI: 10.1038/s41591-019-0475-6.

REFERENCES

Cramer GD, Darby SA. 2014. *Clinical Anatomy of the Spine, Spinal Cord, and Ans*. St. Louis, Missouri: Elsevier. DOI: 10.1016/C2009-0-42801-0.

Crema A, Bassolino M, Guanziroli E, Colombo M, Blanke O, Serino A, Micera S, Molteni F. 2022. Neuromuscular electrical stimulation restores upper limb sensory-motor functions and body representations in chronic stroke survivors. *Med* 3:58–74. DOI: 10.1016/j.medj.2021.12.001.

Danner SM, Hofstoetter US, Ladenbauer J, Rattay F, Minassian K. 2011. Can the Human Lumbar Posterior Columns Be Stimulated by Transcutaneous Spinal Cord Stimulation? A Modeling Study. *Artificial Organs* 35:257–262. DOI: 10.1111/j.1525-1594.2011.01213.x.

Danner SM, Krenn M, Hofstoetter US, Toth A, Mayr W, Minassian K. 2016. Body Position Influences Which Neural Structures Are Recruited by Lumbar Transcutaneous Spinal Cord Stimulation. *PLOS ONE* 11:e0147479. DOI: 10.1371/journal.pone.0147479.

Dawson GD. 1956. The relative excitability and conduction velocity of sensory and motor nerve fibres in man. *The Journal of Physiology* 131:436–451. DOI: 10.1113/jphysiol.1956.sp005473.

Devanne H, Lavoie BA, Capaday C. 1997. Input-output properties and gain changes in the human corticospinal pathway. *Experimental Brain Research* 114:329–338. DOI: 10.1007/PL00005641.

Enoka RM. 2015. *Neuromechanics of Human Movement*. Champaign, IL: Human Kinetics.

Enoka RM, Fuglevand AJ. 2001. Motor unit physiology: Some unresolved issues. *Muscle & Nerve* 24:4–17. DOI: 10.1002/1097-4598(200101)24:1<4::AID-MUS13>3.0.CO;2-F.

Field-Fote EC, Anderson B, Robertson VJ, Spielholz NI. 2003. Monophasic and biphasic

stimulation evoke different responses. *Muscle & Nerve* 28:239–241. DOI: 10.1002/mus.10414.

Fiocchi S, Ravazzani P, Priori A, Parazzini M. 2016. Cerebellar and Spinal Direct Current Stimulation in Children: Computational Modeling of the Induced Electric Field. *Frontiers in Human Neuroscience* 10:1–13. DOI: 10.3389/fnhum.2016.00522.

Formento E, Minassian K, Wagner F, Mignardot JB, Le Goff-Mignardot CG, Rowald A, Bloch J, Micera S, Capogrosso M, Courtine G. 2018. Electrical spinal cord stimulation must preserve proprioception to enable locomotion in humans with spinal cord injury. *Nature Neuroscience* 21:1728–1741. DOI: 10.1038/s41593-018-0262-6.

Forst JC, Blok DC, Slopsema JP, Boss JM, Heyboer LA, Tobias CM, Polasek KH. 2015. Surface electrical stimulation to evoke referred sensation. *Journal of Rehabilitation Research and Development* 52:397–406. DOI: 10.1682/JRRD.2014.05.0128.

de Freitas RM, Capogrosso M, Nomura T, Milosevic M. 2022a. Preferential activation of proprioceptive and cutaneous sensory fibers compared to motor fibers during cervical transcutaneous spinal cord stimulation: a computational study. *Journal of Neural Engineering* 19:1–13. DOI: 10.1088/1741-2552/ac6a7c.

de Freitas RM, Capogrosso M, Nomura T, Milosevic M. 2022b. Optimizing sensory fiber activation during cervical transcutaneous spinal stimulation using different electrode configurations: A computational analysis. *Artificial Organs* 00:1–12. DOI: 10.1111/aor.14323.

de Freitas RM, Sasaki A, Sayenko DG, Masugi Y, Nomura T, Nakazawa K, Milosevic M. 2021. Selectivity and excitability of upper-limb muscle activation during cervical transcutaneous spinal cord stimulation in humans. *Journal of Applied Physiology* 131:746–759. DOI: 10.1152/japplphysiol.00132.2021.

REFERENCES

Freyvert Y, Yong NA, Morikawa E, Zdunowski S, Sarino ME, Gerasimenko Y, Edgerton VR, Lu DC. 2018. Engaging cervical spinal circuitry with non-invasive spinal stimulation and buspirone to restore hand function in chronic motor complete patients. *Scientific reports* 8:1–10. DOI: 10.1038/s41598-018-33123-5.

Gad P, Lee S, Terrafranca N, Zhong H, Turner A, Gerasimenko Y, Edgerton VR. 2018. Non-Invasive Activation of Cervical Spinal Networks after Severe Paralysis. *Journal of Neurotrauma* 35:2145–2158. DOI: 10.1089/neu.2017.5461.

Gaines JL, Finn KE, Slopsema JP, Heyboer LA, Polasek KH. 2018. A model of motor and sensory axon activation in the median nerve using surface electrical stimulation. *Journal of Computational Neuroscience* 45:29–43. DOI: 10.1007/s10827-018-0689-5.

Gerasimenko Y, Gorodnichev R, Moshonkina T, Sayenko D, Gad P, Reggie Edgerton V. 2015a. Transcutaneous electrical spinal-cord stimulation in humans. *Annals of Physical and Rehabilitation Medicine* 58:225–231. DOI: 10.1016/j.rehab.2015.05.003.

Gerasimenko YP, Lu DC, Modaber M, Zdunowski S, Gad P, Sayenko DG, Morikawa E, Haakana P, Ferguson AR, Roy RR, Edgerton VR. 2015b. Noninvasive Reactivation of Motor Descending Control after Paralysis. *Journal of Neurotrauma* 32:1968–1980. DOI: 10.1089/neu.2015.4008.

Gordon NM, Rudroff T, Enoka JA, Enoka RM. 2012. Handedness but not dominance influences variability in endurance time for sustained, submaximal contractions. *Journal of Neurophysiology* 108:1501–1510. DOI: 10.1152/jn.01144.2011.

Graham RD, Bruns TM, Duan B, Lempka SF. 2019. Dorsal root ganglion stimulation for chronic pain modulates Aβ-fiber activity but not C-fiber activity: A computational modeling study. *Clinical Neurophysiology* 130:941–951. DOI: 10.1016/j.clinph.2019.02.016.

REFERENCES

Greiner N, Barra B, Schiavone G, Lorach H, James N, Conti S, Kaeser M, Fallegger F, Borgognon S, Lacour S, Bloch J, Courtine G, Capogrosso M. 2021. Recruitment of upper-limb motoneurons with epidural electrical stimulation of the cervical spinal cord. *Nature Communications* 12:1–19. DOI: 10.1038/s41467-020-20703-1.

Grill WM. 1999. Modeling the effects of electric fields on nerve fibers: influence of tissue electrical properties. *IEEE Transactions on Biomedical Engineering* 46:918–928. DOI: 10.1109/10.775401.

Guidetti M, Ferrucci R, Vergari M, Aglieco G, Naci A, Versace S, Pacheco-Barrios K, Giannoni-Luza S, Barbieri S, Priori A, Bocci T. 2021. Effects of Transcutaneous Spinal Direct Current Stimulation (tsDCS) in Patients With Chronic Pain: A Clinical and Neurophysiological Study. *Frontiers in Neurology* 12:1–9. DOI: 10.3389/fneur.2021.695910.

Hawker GA, Mian S, Kendzerska T, French M. 2011. Measures of adult pain: Visual Analog Scale for Pain (VAS Pain), Numeric Rating Scale for Pain (NRS Pain), McGill Pain Questionnaire (MPQ), Short-Form McGill Pain Questionnaire (SF-MPQ), Chronic Pain Grade Scale (CPGS), Short Form-36 Bodily Pain Scale (SF. *Arthritis Care & Research* 63:S240–S252. DOI: 10.1002/acr.20543.

Hines ML, Carnevale NT. 1997. The NEURON Simulation Environment. *Neural Computation* 9:1179–1209. DOI: 10.1162/neco.1997.9.6.1179.

Hodgkin AL, Huxley AF. 1952. A quantitative description of membrane current and its application to conduction and excitation in nerve. *The Journal of Physiology* 117:500–544. DOI: 10.1113/jphysiol.1952.sp004764.

Hofstoetter US, Danner SM, Freundl B, Binder H, Mayr W, Rattay F, Minassian K. 2015a. Periodic modulation of repetitively elicited monosynaptic reflexes of the human

lumbosacral spinal cord. *Journal of Neurophysiology* 114:400–410. DOI: 10.1152/jn.00136.2015.

Hofstoetter US, Freundl B, Binder H, Minassian K. 2018. Common neural structures activated by epidural and transcutaneous lumbar spinal cord stimulation: Elicitation of posterior root-muscle reflexes. *PLOS ONE* 13:1–22. DOI: 10.1371/journal.pone.0192013.

Hofstoetter US, Krenn M, Danner SM, Hofer C, Kern H, McKay WB, Mayr W, Minassian K. 2015b. Augmentation of Voluntary Locomotor Activity by Transcutaneous Spinal Cord Stimulation in Motor-Incomplete Spinal Cord-Injured Individuals. *Artificial Organs* 39:E176–E186. DOI: 10.1111/aor.12615.

Hofstoetter US, McKay WB, Tansey KE, Mayr W, Kern H, Minassian K. 2014. Modification of spasticity by transcutaneous spinal cord stimulation in individuals with incomplete spinal cord injury. *The Journal of Spinal Cord Medicine* 37:202–211. DOI: 10.1179/2045772313Y.0000000149.

Howells J, Trevillion L, Bostock H, Burke D. 2012. The voltage dependence of I h in human myelinated axons. *The Journal of Physiology* 590:1625–1640. DOI: 10.1113/jphysiol.2011.225573.

Hultborn H, Illert M, Nielsen J, Paul A, Ballegaard M, Wiese H. 1996. On the mechanism of the post-activation depression of the H-reflex in human subjects. *Experimental Brain Research* 108:450–462. DOI: 10.1007/BF00227268.

Inanici F, Brighton LN, Samejima S, Hofstetter CP, Moritz CT. 2021. Transcutaneous Spinal Cord Stimulation Restores Hand and Arm Function After Spinal Cord Injury. *IEEE Transactions on Neural Systems and Rehabilitation Engineering* 29:310–319. DOI: 10.1109/TNSRE.2021.3049133.

REFERENCES

Inanici F, Samejima S, Gad P, Edgerton VR, Hofstetter CP, Moritz CT. 2018. Transcutaneous Electrical Spinal Stimulation Promotes Long-Term Recovery of Upper Extremity Function in Chronic Tetraplegia. *IEEE transactions on neural systems and rehabilitation engineering : a publication of the IEEE Engineering in Medicine and Biology Society* 26:1272–1278. DOI: 10.1109/TNSRE.2018.2834339.

Islam MA, Zaaya M, Comiskey E, Demetrio J, O'Keefe A, Palazzo N, Pulverenti TS, Knikou M. 2020. Modulation of soleus H-reflex excitability following cervical transspinal conditioning stimulation in humans. *Neuroscience Letters* 732:1–6. DOI: 10.1016/j.neulet.2020.135052.

Kandel ER, Schwartz JH, Jessell TM, Siegelbaum SA, Hudspeth AJ. 2013. Principles of Neural Science. In: McGraw-Hill ed. *New York, NY: McGraw-Hill*. New York,.

Katz R, Penicaud A, Rossi A. 1991. Reciprocal Ia inhibition between elbow flexors and extensors in the human. *The Journal of Physiology* 437:269–286. DOI: 10.1113/jphysiol.1991.sp018595.

Kendall FP, Kendall EM, Provance PG, Rodgers MM, Romani WA. 2005. *Muscles: Testing and Function with Posture and Pain*. Philadelphia, PA: Lippincott, Williams, & Wilkins.

Khadka N, Liu X, Zander H, Swami J, Rogers E, Lempka SF, Bikson M. 2020. Realistic anatomically detailed open-source spinal cord stimulation (RADO-SCS) model. *Journal of Neural Engineering* 17:1–12. DOI: 10.1088/1741-2552/ab8344.

Kiernan MC, Mogyoros I, Burke D. 1996. Differences in the recovery of excitability in sensory and motor axons of human median nerve. *Brain* 119:1099–1105. DOI: 10.1093/brain/119.4.1099.

REFERENCES

Kitano K, Koceja DM. 2009. Spinal reflex in human lower leg muscles evoked by transcutaneous spinal cord stimulation. *Journal of Neuroscience Methods* 180:111–115. DOI: 10.1016/j.jneumeth.2009.03.006.

Krenn M, Toth A, Danner SM, Hofstoetter US, Minassian K, Mayr W. 2013. Selectivity of transcutaneous stimulation of lumbar posterior roots at different spinal levels in humans. *Biomedical Engineering / Biomedizinische Technik* 58. DOI: 10.1515/bmt-2013-4010.

Kuhn A, Keller T, Lawrence M, Morari M. 2009. A model for transcutaneous current stimulation: simulations and experiments. *Medical & Biological Engineering & Computing* 47:279–289. DOI: 10.1007/s11517-008-0422-z.

Kumru H, Rodríguez-Cañón M, Edgerton VR, García L, Flores Á, Soriano I, Opisso E, Gerasimenko Y, Navarro X, García-Alías G, Vidal J. 2021. Transcutaneous Electrical Neuromodulation of the Cervical Spinal Cord Depends Both on the Stimulation Intensity and the Degree of Voluntary Activity for Training. A Pilot Study. *Journal of Clinical Medicine* 10:1–16. DOI: 10.3390/jcm10153278.

Ladenbauer J, Minassian K, Hofstoetter US, Dimitrijevic MR, Rattay F. 2010. Stimulation of the Human Lumbar Spinal Cord With Implanted and Surface Electrodes: A Computer Simulation Study. *IEEE Transactions on Neural Systems and Rehabilitation Engineering* 18:637–645. DOI: 10.1109/TNSRE.2010.2054112.

Lee Y, Hwang K. 2002. Skin thickness of Korean adults. *Surgical and Radiologic Anatomy* 24:183–189. DOI: 10.1007/s00276-002-0034-5.

Lu DC, Edgerton VR, Modaber M, AuYong N, Morikawa E, Zdunowski S, Sarino ME, Sarrafzadeh M, Nuwer MR, Roy RR, Gerasimenko Y. 2016. Engaging Cervical Spinal Cord Networks to Reenable Volitional Control of Hand Function in Tetraplegic Patients. *Neurorehabilitation and Neural Repair* 30:951–962. DOI: 10.1177/1545968316644344.

REFERENCES

Manson GA, Atkinson DA, Shi Z, Sheynin J, Karmonik C, Markley RL, Sayenko DG. 2022. Transcutaneous spinal stimulation alters cortical and subcortical activation patterns during mimicked-standing: A proof-of-concept fMRI study. *Neuroimage: Reports* 2:1–11. DOI: 10.1016/j.ynirp.2022.100090.

Marchand-Pauvert V, Nicolas G, Pierrot-Deseilligny E. 2000. Monosynaptic Ia projections from intrinsic hand muscles to forearm motoneurones in humans. *The Journal of Physiology* 525:241–252. DOI: 10.1111/j.1469-7793.2000.t01-1-00241.x.

Massey SJ, Al'joboori YD, Vanhoestenberghe A, Duffell LD. 2018. The Effects of Neuromodulation on Central Excitability of the Upper Limb in Healthy, Able-bodied Adults. In: *International Functional Electrical Stimulation Society Proceedings 2018*. 68–70.

McIntosh JR, Joiner EF, Goldberg JL, Murray LM, Yasin B, Mendiratta A, Karceski SC, Thuet E, Modik O, Shelkov E, Mandigo C, Daniel Riew K, Harel NY, Virk MS, Carmel JB, Peters VA Med Ctr JJ. 2022. An actionable map of arm and hand muscle responses to electrical stimulation of the dorsal cervical spinal cord in humans. *bioRxiv*. DOI: 10.1101/2022.01.29.478182.

McIntyre CC, Richardson AG, Grill WM. 2002. Modeling the Excitability of Mammalian Nerve Fibers: Influence of Afterpotentials on the Recovery Cycle. *Journal of Neurophysiology* 87:995–1006. DOI: 10.1152/jn.00353.2001.

McNulty PA, Türker KS, Macefield VG. 1999. Evidence for strong synaptic coupling between single tactile afferents and motoneurones supplying the human hand. *The Journal of Physiology* 518:883–893. DOI: 10.1111/j.1469-7793.1999.0883p.x.

Melzack R, Wall PD. 1965. Pain mechanisms: a new theory. *Science (New York, N.Y.)* 150:971–9. DOI: 10.1126/science.150.3699.971.

REFERENCES

Mendez A, Islam R, Latypov T, Basa P, Joseph OJ, Knudsen B, Siddiqui AM, Summer P, Staehnke LJ, Grahn PJ, Lachman N, Windebank AJ, Lavrov IA. 2021. Segment-Specific Orientation of the Dorsal and Ventral Roots for Precise Therapeutic Targeting of Human Spinal Cord. *Mayo Clinic Proceedings* 96:1426–1437. DOI: 10.1016/j.mayocp.2020.07.039.

Milosevic M, Masugi Y, Obata H, Sasaki A, Popovic MR, Nakazawa K. 2019a. Short-term inhibition of spinal reflexes in multiple lower limb muscles after neuromuscular electrical stimulation of ankle plantar flexors. *Experimental Brain Research* 237:467–476. DOI: 10.1007/s00221-018-5437-6.

Milosevic M, Masugi Y, Sasaki A, Sayenko DG, Nakazawa K. 2019b. On the reflex mechanisms of cervical transcutaneous spinal cord stimulation in human subjects. *Journal of Neurophysiology* 121:1672–1679. DOI: 10.1152/jn.00802.2018.

Minassian K, McKay WB, Binder H, Hofstoetter US. 2016. Targeting Lumbar Spinal Neural Circuitry by Epidural Stimulation to Restore Motor Function After Spinal Cord Injury. *Neurotherapeutics* 13:284–294. DOI: 10.1007/s13311-016-0421-y.

Minassian K, Persy I, Rattay F, Dimitrijevic MR, Hofer C, Kern H. 2007. Posterior root–muscle reflexes elicited by transcutaneous stimulation of the human lumbosacral cord. *Muscle & Nerve* 35:327–336. DOI: 10.1002/mus.20700.

Moraud EM, Capogrosso M, Formento E, Wenger N, DiGiovanna J, Courtine G, Micera S. 2016. Mechanisms Underlying the Neuromodulation of Spinal Circuits for Correcting Gait and Balance Deficits after Spinal Cord Injury. *Neuron* 89:814–828. DOI: 10.1016/j.neuron.2016.01.009.

Murray LM, Knikou M. 2017. Remodeling Brain Activity by Repetitive Cervicothoracic Transspinal Stimulation after Human Spinal Cord Injury. *Frontiers in Neurology* 8:1–8.

REFERENCES

DOI: 10.3389/fneur.2017.00050.

Murray LM, Knikou M. 2019. Transspinal stimulation increases motoneuron output of multiple segments in human spinal cord injury. *PLOS ONE* 14:1–21. DOI: 10.1371/journal.pone.0213696.

Oakley JC, Prager JP. 2002. Spinal Cord Stimulation. *Spine* 27:2574–2583. DOI: 10.1097/00007632-200211150-00034.

Oldfield RC. 1971. The assessment and analysis of handedness: The Edinburgh inventory. *Neuropsychologia* 9:97–113. DOI: 10.1016/0028-3932(71)90067-4.

Park S-W, Wolf SL, Blanton S, Winstein C, Nichols-Larsen DS. 2008. The EXCITE Trial: Predicting a clinically meaningful motor activity log outcome. *Neurorehabilitation and neural repair* 22:486–93. DOI: 10.1177/1545968308316906.

Pereira R, Freire IV, Cavalcanti CVG, Luz CPN, Neto OP. 2012. Hand dominance during constant force isometric contractions: evidence of different cortical drive commands. *European Journal of Applied Physiology* 112:2999–3006. DOI: 10.1007/s00421-011-2278-4.

Peurala SH, Pitkänen K, Sivenius J, Tarkka IM. 2002. Cutaneous electrical stimulation may enhance sensorimotor recovery in chronic stroke. *Clinical Rehabilitation* 16:709–716. DOI: 10.1191/0269215502cr543oa.

Pierrot-Deseilligny E, Burke D. 2005. *The Circuitry of the Human Spinal Cord*. Cambridge, UK: Cambridge University Press. DOI: 10.1017/CBO9780511545047.

Plonsey R, Heppner DB. 1967. Considerations of quasi-stationarity in electrophysiological systems. *The Bulletin of Mathematical Biophysics* 29:657–664. DOI: 10.1007/BF02476917.

REFERENCES

Rattay F. 1999. The basic mechanism for the electrical stimulation of the nervous system. *Neuroscience* 89:335–346. DOI: 10.1016/S0306-4522(98)00330-3.

Rattay F, Danner SM, Hofstoetter US, Minassian K. 2014. Finite Element Modeling for Extracellular Stimulation. In: *Encyclopedia of Computational Neuroscience*. New York, NY: Springer New York, 1–12. DOI: 10.1007/978-1-4614-7320-6_593-5.

Rejc E, Smith AC, Weber KA, Ugiliweneza B, Bert RJ, Negahdar M, Boakye M, Harkema SJ, Angeli CA. 2020. Spinal Cord Imaging Markers and Recovery of Volitional Leg Movement With Spinal Cord Epidural Stimulation in Individuals With Clinically Motor Complete Spinal Cord Injury. *Frontiers in Systems Neuroscience* 14:1–15. DOI: 10.3389/fnsys.2020.559313.

Richardson AG, McIntyre CC, Grill WM. 2000. Modelling the effects of electric fields on nerve fibres: Influence of the myelin sheath. *Medical and Biological Engineering and Computing* 38:438–446. DOI: 10.1007/BF02345014.

Rossi-Durand C, Jones KE, Adams S, Bawa P. 1999. Comparison of the depression of H-reflexes following previous activation in upper and lower limb muscles in human subjects. *Experimental Brain Research* 126:117–127. DOI: 10.1007/s002210050721.

Rowald A, Komi S, Demesmaeker R, Baaklini E, Hernandez-Charpak SD, Paoles E, Montanaro H, Cassara A, Becce F, Lloyd B, Newton T, Ravier J, Kinany N, D'Ercole M, Paley A, Hankov N, Varescon C, McCracken L, Vat M, Caban M, Watrin A, Jacquet C, Bole-Feysot L, Harte C, Lorach H, Galvez A, Tschopp M, Herrmann N, Wacker M, Geernaert L, Fodor I, Radevich V, Van Den Keybus K, Eberle G, Pralong E, Roulet M, Ledoux J-B, Fornari E, Mandija S, Mattera L, Martuzzi R, Nazarian B, Benkler S, Callegari S, Greiner N, Fuhrer B, Froeling M, Buse N, Denison T, Buschman R, Wende C, Ganty D, Bakker J, Delattre V, Lambert H, Minassian K, van den Berg CAT,

REFERENCES

Kavounoudias A, Micera S, Van De Ville D, Barraud Q, Kurt E, Kuster N, Neufeld E, Capogrosso M, Asboth L, Wagner FB, Bloch J, Courtine G. 2022. Activity-dependent spinal cord neuromodulation rapidly restores trunk and leg motor functions after complete paralysis. *Nature Medicine* 28:260–271. DOI: 10.1038/s41591-021-01663-5.

Roy FD, Bosgra D, Stein RB. 2014. Interaction of transcutaneous spinal stimulation and transcranial magnetic stimulation in human leg muscles. *Experimental Brain Research* 232:1717–1728. DOI: 10.1007/s00221-014-3864-6.

Roy FD, Gibson G, Stein RB. 2012. Effect of percutaneous stimulation at different spinal levels on the activation of sensory and motor roots. *Experimental Brain Research* 223:281–289. DOI: 10.1007/s00221-012-3258-6.

Sabbahi MA, Sengul YS. 2012. Cervical multisegmental motor responses in healthy subjects. *Spinal Cord* 50:432–439. DOI: 10.1038/sc.2011.166.

Sasaki A, de Freitas RM, Sayenko DG, Masugi Y, Nomura T, Nakazawa K, Milosevic M. 2021. Low-Intensity and Short-Duration Continuous Cervical Transcutaneous Spinal Cord Stimulation Intervention Does Not Prime the Corticospinal and Spinal Reflex Pathways in Able-Bodied Subjects. *Journal of Clinical Medicine* 10:1–13. DOI: 10.3390/jcm10163633.

Sass LR, Khani M, Natividad GC, Tubbs RS, Baledent O, Martin BA. 2017. A 3D subject-specific model of the spinal subarachnoid space with anatomically realistic ventral and dorsal spinal cord nerve rootlets. *Fluids and Barriers of the CNS* 14:1–16. DOI: 10.1186/s12987-017-0085-y.

Sass LR, Khani M, Romm J, Schmid Daners M, McCain K, Freeman T, Carter GT, Weeks DL, Petersen B, Aldred J, Wingett D, Martin BA. 2020. Non-invasive MRI quantification of cerebrospinal fluid dynamics in amyotrophic lateral sclerosis patients.

REFERENCES

Fluids and Barriers of the CNS 17:1–14. DOI: 10.1186/s12987-019-0164-3.

Sathiamoorthy A, Sathiamoorthy SS. 1990. Limb dominance and motor conduction velocity of median and ulnar nerves. *Indian journal of physiology and pharmacology* 34:51–53.

Sayenko DG, Atkinson DA, Dy CJ, Gurley KM, Smith VL, Angeli C, Harkema SJ, Edgerton VR, Gerasimenko YP. 2015a. Spinal segment-specific transcutaneous stimulation differentially shapes activation pattern among motor pools in humans. *Journal of Applied Physiology* 118:1364–1374. DOI: 10.1152/japplphysiol.01128.2014.

Sayenko DG, Atkinson DA, Floyd TC, Gorodnichev RM, Moshonkina TR, Harkema SJ, Edgerton VR, Gerasimenko YP. 2015b. Effects of paired transcutaneous electrical stimulation delivered at single and dual sites over lumbosacral spinal cord. *Neuroscience letters* 609:229–34. DOI: 10.1016/j.neulet.2015.10.005.

Seáñez I, Capogrosso M. 2021. Motor improvements enabled by spinal cord stimulation combined with physical training after spinal cord injury: review of experimental evidence in animals and humans. *Bioelectronic Medicine* 7:1–13. DOI: 10.1186/s42234-021-00077-5.

Sekiguchi H, Nakazawa K, Suzuki S. 2003. Differences in recruitment properties of the corticospinal pathway between lengthening and shortening contractions in human soleus muscle. *Brain Research* 977:169–179. DOI: 10.1016/S0006-8993(03)02621-0.

Smith AC, Rymer WZ, Knikou M. 2015. Locomotor training modifies soleus monosynaptic motoneuron responses in human spinal cord injury. *Experimental Brain Research* 233:89–103. DOI: 10.1007/s00221-014-4094-7.

Taccola G, Sayenko D, Gad P, Gerasimenko Y, Edgerton VR. 2018. And yet it moves : Recovery of volitional control after spinal cord injury. *Progress in Neurobiology*

160:64–81. DOI: 10.1016/j.pneurobio.2017.10.004.

Taylor C, McHugh C, Mockler D, Minogue C, Reilly RB, Fleming N. 2021. Transcutaneous spinal cord stimulation and motor responses in individuals with spinal cord injury: A methodological review. *PLOS ONE* 16:1–33. DOI: 10.1371/journal.pone.0260166.

Torriani M, Gill CM, Daley S, Oliveira AL, Azevedo DC, Bredella MA. 2014. Compartmental neck fat accumulation and its relation to cardiovascular risk and metabolic syndrome. *The American Journal of Clinical Nutrition* 100:1244–1251. DOI: 10.3945/ajcn.114.088450.

Verhoeven K, VANDIJK J. 2006. Decreasing pain in electrical nerve stimulation. *Clinical Neurophysiology* 117:972–978. DOI: 10.1016/j.clinph.2006.01.006.

Villar Ortega E, Ansó J, Bütler KA, Marchal-Crespo L. 2019. High-frequency transcutaneous cervical electrical stimulation: A pilot study. In: 115–118.

Wade RG, Bligh ER, Nar K, Stone RS, Roberts DJ, Teh I, Bourke G. 2020. The Geometry of the roots of the Brachial Plexus. *Journal of Anatomy* 237:999–1005. DOI: 10.1111/joa.13270.

Wagner FB, Mignardot J-B, Le Goff-Mignardot CG, Demesmaeker R, Komi S, Capogrosso M, Rowald A, Seáñez I, Caban M, Pirondini E, Vat M, McCracken LA, Heimgartner R, Fodor I, Watrin A, Seguin P, Paoles E, Van Den Keybus K, Eberle G, Schurch B, Pralong E, Becce F, Prior J, Buse N, Buschman R, Neufeld E, Kuster N, Carda S, von Zitzewitz J, Delattre V, Denison T, Lambert H, Minassian K, Bloch J, Courtine G. 2018. Targeted neurotechnology restores walking in humans with spinal cord injury. *Nature* 563:65–71. DOI: 10.1038/s41586-018-0649-2.

Wenger N, Moraud EM, Gandar J, Musienko P, Capogrosso M, Baud L, Le Goff CG,

REFERENCES

Barraud Q, Pavlova N, Dominici N, Minev IR, Asboth L, Hirsch A, Duis S, Kreider J, Mortera A, Haverbeck O, Kraus S, Schmitz F, DiGiovanna J, van den Brand R, Bloch J, Detemple P, Lacour SP, Bézard E, Micera S, Courtine G. 2016. Spatiotemporal neuromodulation therapies engaging muscle synergies improve motor control after spinal cord injury. *Nature Medicine* 22:138–145. DOI: 10.1038/nm.4025.

West CA, McKay Hart A, Terenghi G, Wiberg M. 2012. Sensory Neurons of the Human Brachial Plexus. *Neurosurgery* 70:1183–1194. DOI: 10.1227/NEU.0b013e318241ace1.

Wu YK, Levine JM, Wecht JR, Maher MT, LiMonta JM, Saeed S, Santiago TM, Bailey E, Kastuar S, Guber KS, Yung L, Weir JP, Carmel JB, Harel NY. 2020. Posteroanterior cervical transcutaneous spinal stimulation targets ventral and dorsal nerve roots. *Clinical Neurophysiology* 131:451–460. DOI: 10.1016/j.clinph.2019.11.056.

Zheng Y, Hu X. 2020a. Muscle activation pattern elicited through transcutaneous stimulation near the cervical spinal cord. *Journal of Neural Engineering* 17:1–13. DOI: 10.1088/1741-2552/ab5e09.

Zheng Y, Hu X. 2020b. Elicited upper limb motions through transcutaneous cervical spinal cord stimulation. *Journal of Neural Engineering* 17:1–10. DOI: 10.1088/1741-2552/ab8f6f.

Acknowledgements

The three years of my PhD have been the most challenging and transformative years of my life, and I am really grateful for the everyone who joined me on this journey.

First, I would like to express my gratitude to Prof. Taishin Nomura for opening the doors of his laboratory to me. I thank him for providing financial and technical support, which were crucial for my academic achievements and success. Especially, I also would like to thank Dr. Matija Milosevic for his tremendous efforts and dedication in my supervision. Among the many and various skills that I learned from him, I would like to express my appreciation for teaching to focus in my objectives. It has been an enormous pleasure working with you.

I wish to thank Dr. Takuyuki Endo for giving me the opportunity to work at Toneyama Hospital. It has been a very fruitful experience for me. Importantly, I am grateful for Prof. Kimitaka Nakazawa and Dr. Atsushi Sasaki for making experiments with transcutaneous spinal cord stimulation possible at University of Tokyo. I also thank Dr. Marco Capogrosso from University of Pittsburgh for helping me with my computational simulations.

I thank my friends Naomi and Vitor for all the good times in Osaka, and for their emotional support (a.k.a. coffee sessions in the advising room). I thank Shou for being supportive, and for teaching me (the good and bad) Japanese language and culture. Despite being on the other side of the globe, I also thank my family for always being understanding and encouraging of my endeavours (I love you all).

Last but not least, I thank the Engineering Science 21st Century scholarship from the Ministry of Education, Culture, Sports, Science and Technology in Japan (MEXT) for the financial support and for providing me an opportunity to conduct my doctoral course studies in Japan.

Publications

Journal Papers (first author)

de Freitas, R. M., Capogrosso, M., Nomura, T., & Milosevic, M. 2022. Optimizing sensory fiber activation during cervical transcutaneous spinal cord stimulation using different electrode configurations: A computational analysis. *Artificial Organs* 00:1-12. DOI: 10.1111/aor.14323

de Freitas RM, Capogrosso M, Nomura T, Milosevic M. 2022. Preferential activation of proprioceptive and cutaneous sensory fibers compared to motor fibers during cervical transcutaneous spinal cord stimulation: a computational study. Journal of Neural Engineering 19:1-13. DOI: 10.1088/1741-2552/ac6a7c.

de Freitas RM, Sasaki A, Sayenko DG, Masugi Y, Nomura T, Nakazawa K, Milosevic M. 2021. Selectivity and excitability of upper-limb muscle activation during cervical transcutaneous spinal cord stimulation in humans. Journal of Applied Physiology 131:746–759. DOI: 10.1152/japplphysiol.00132.2021.

Journal Paper (others)

Sasaki A, de Freitas RM, Sayenko DG, Masugi Y, Nomura T, Nakazawa K, Milosevic M. 2021. Low-Intensity and Short-Duration Continuous Cervical Transcutaneous Spinal Cord Stimulation Intervention Does Not Prime the Corticospinal and Spinal Reflex Pathways in Able-Bodied Subjects. Journal of Clinical Medicine 10:1-13. DOI: 10.3390/jcm10163633.

PUBLICATIONS

International Conference Papers (first author)

de Freitas, R. M., Nomura, T., & Milosevic, M. 2021. Development of an anatomically realistic cervical transcutaneous spinal cord stimulation model. *2021 IFESS conferences, Artificial Organs* E99–E103. DOI: 10.1111/aor.14132

Freitas, R. M., & Kohn, A. F. 2020. Quantitative and Qualitative Parameters of Myoelectric Signals for Computational Simulations of Human Surface Electromyograms. *ACM International Conference Proceeding Series* 256–262. DOI: 10.1145/3397391.3397446

International Conference Paper (other)

Mengyi, W., Li, L., de Freitas, R. M., Endo, T., Nomura, T., & Nakamura, T. 2022. Assessment of spatio-temporal gait parameters using a novel wearable motion capture system. *2022 IEEE 4th Global Conference on Life Sciences and Technologies (LifeTech)* 527–528. DOI: 10.1109/LifeTech53646.2022.9754827